UNIVERSITY OF CALIFORNIA, SAN DIEGO

Diurnal to Annual Variations in the Atmospheric Water Cycle

A dissertation submitted in partial satisfaction of the

requirements for the degree Doctor of Philosophy

in

Earth Sciences

by

Alexander C. Ruane

Committee in charge:

John Roads, Chair
Masao Kanamitsu
Arthur Miller
Joel Norris
Richard Salmon
Jeffrey Vincent

2007

The dissertation of Alexander C. Ruane is approved, and it is acceptable in quality and form for publication on microfilm:

_____

_____

_____

_____

_____

_____

Chair

University of California, San Diego

2007

TABLE OF CONTENTS

LIST OF FIGURES AND TABLES

ACKNOWLEDGMENTS

My relationship with John Roads has been essential to my enjoyment of these last five years at Scripps. John pulled off the difficult combination of support, motivation, and enthusiasm based on a foundation of honesty and respect. I have been fortunate enough to gain some global exposure through John's many connections and had the independence to pursue some of my own research and academic initiatives, but John made sure I balanced my travel to international meetings and my SIO environmental science extra-curriculars with a rigorous research schedule. I especially appreciate John's constant open-door policy and his rapid responses to my emails no matter which corner of the globe he was in or what ordeal he was going through. I am also thankful for the time and effort he took to provide feedback on my many manuscript drafts.

Many thanks are also due to the members of my thesis committee, Masao Kanamitsu, Art Miller, Joel Norris, Rick Salmon, and Jeff Vincent, for finding time for me in their busy schedules and for providing many helpful comments and research ideas. Kana, in particular, has always kept his door open to help me understand the NCEP Global Spectral Model.

I was spared many hours of frustration due to the excellent computer support of Jack Ritchie, Patrick Tripp, and Martin Olivera. I would also like to recognize the administrative work of Diane Boomer, Mishauno Woggon, Shivani Singh, Nirvana Singh, Caroline Baxter, and Dawn Huffman, which allowed me to concentrate on my research and conference plans without worrying about bureaucratic distractions. I had many stimulating conversations with Ana Nunes, Hideki Kanamaru, and other researchers throughout the SIO Climate Research Division, and thank Emelia Bainto for

her programming work on CEOP variables. Wesley Ebisuzaki and Jack Woollen at the National Centers for Environmental Prediction were also very helpful in providing reformatted observation files for my reanalysis, and my interactions with researchers in the Coordinated Enhanced Observing Period were very influential in my research directions. I am also grateful to Bruce Anderson, David Mocko, and Mike Bosilovich for helping me identify bugs in the CEOP output.

Liz Douglass was an absolutely wonderful officemate, always willing to let me vent about my research (or whatever else was bothering me) and helping me to get through the stressful portions of graduate life at Scripps. I would also like to thank the other members of our tight group of climate students who arrived in 2002 (Hyodae Seo, Odelle Hadley, Guillaume Mauger, Hey-Jin Kim, and John Holecek), the students from the Scripps Environmental Science and Policy (ESP) group, everybody who made lunchtime in the Nierenberg rose garden something to look forward to, and Lisa Shaffer for her frequent advice and guidance.

My wife, Abbi, has been an absolute blessing throughout this entire process, keeping me on an even keel despite many hours of her early commutes and (recently) morning sickness. I'd also like to thank my parents and extended family for their constant support and their interest in my work. In addition to completing this thesis, during my time at Scripps I have moved across the country, become engaged, married, a father-to-be, and a world traveler, none of which would have been possible without so many supportive family members and friends.

Chapter 2, in full, is a reproduction of the work by Ruane, A.C., and J.O Roads in the *Journal of the Meteorological Society of Japan*, 2007, **85A**, 117-143, which is part of

the "Coordinated Enhanced Observing Period" special issue. Chapter 3 is a reproduction of the work by Ruane, A.C., and J.O. Roads, 2007, which is in press at *Earth Interactions*. Chapter 4 is a reproduction of a Ruane, A.C., and J.O. Roads manuscript that has been accepted as part of the "Understanding Diurnal Variability of Precipitation through Observations and Models" special issue of the *Journal of Climate*.

I, Alexander C. Ruane, was the primary investigator and author of these papers. I conducted the analysis presented therein and prepared each manuscript for publication. John Roads helped guide the research direction and contributed greatly to the successive drafts of these works through many useful discussions and helpful criticisms.

My dissertation research was supported through grants from the National Oceanic and Atmospheric Administration (NOAA NA17RJ1231) and the National Aeronautics and Space Administration (NASA NNG05GR50G and NNG06GC85G). We also acknowledge partial support from the California Space Institute (CSI) and California Space Grant Consortium (CSGC), as well as the Admiral Nimitz Fellowship program at the Scripps Institution of Oceanography. The views expressed herein are those of the authors and do not necessarily reflect the views of NOAA, NASA, CSI, or CSGC.

VITA

2000-2002	Undergraduate Research Assistant, Cornell University, Ithaca, NY
2000	Undergraduate Research Assistant, Massachusetts Institute of Technology, Cambridge, MA
2002	Bachelor of Science, Cornell University, Ithaca, NY
2002-2007	Research Assistant, University of California, San Diego, CA
2007	Teacher's Assistant, University of California, San Diego, CA
2007	Doctor of Philosophy, University of California, San Diego, CA

PUBLICATIONS

Anderson, B.T., A. Ruane, J.O. Roads, M. Kanamitsu, and G. Salvucci, 2007: A new metric for estimating local moisture cycling and its influence upon seasonal precipitation rates. *J. Hydrometeor.,* in review.

Bosilovich, M., D. Mocko, W.K.-M. Lau, A. Ruane, and J. Roads, 2006: Initial comparisons of model analyses during the North American Monsoon Experiment (NAME). *CEOP Newsletter*, **10**, 2-3

Ruane, A.C., and J.O. Roads, 2007a: The diurnal cycle of water and energy over the continental United States from three reanalyses. *J. Meteor. Soc. Jpn*., **85A**, 117-143.

Ruane, A.C., and J.O. Roads, 2007b: 6-hour to 1-year variance of five global precipitation sets. *Earth Interactions*, in press.

Ruane, A.C., and J.O. Roads, 2007c: Dominant balances and exchanges of the atmospheric water cycle at diurnal, annual, and intraseasonal time scales. *J. Climate,* accepted.

ABSTRACT OF THE DISSERTATION

Diurnal to Annual Variations in the Atmospheric Water Cycle

by

Alexander C. Ruane
Doctor of Philosophy in Earth Sciences
University of California, San Diego, 2007
John Roads, Chair

This dissertation examines aspects of diurnal to annual variability in the atmospheric water cycle in observations and global numerical weather prediction models. Investigations begin with an in-depth evaluation of variance at a single time scale, followed by a comprehensive analysis of a particular water cycle component, and finally a complete description of the balances and exchanges of water cycle components across time scales.

Comparisons of global and regional reanalyses reveal significant differences in the amplitude and phase of water and energy components' diurnal cycles, with parameterization and land-surface errors propagating throughout the system. Evaluations of the 6-hour to 1-year spectra of global precipitation data from reanalyses and high-resolution precipitation products also indicate significant model biases in capturing the sub-seasonal variability of precipitation as well as disagreement among observation-based products. Component interactions in the atmospheric water cycle

reveal distinct characteristics that are unique to particular locations and time scales, including a clear separation between thermodynamic and dynamic controls of variability.

Together, these experiments reveal considerable differences in the physical mechanisms that govern the atmospheric water cycle at different temporal and spatial scales. Parameterization sets that have been tuned for performance on a given frequency are often inadequate for simulations that require more complete statistical representations of hydrometeorological processes, and simulated water cycle components are still far from observations. Methodologies introduced in this study help isolate key obstacles that prevent the accurate simulation of global hydroclimate, and identify unique processes that are vital to understanding regional anomalies.

CHAPTER I

Introduction

The atmospheric water cycle is an important test bed for our understanding of the atmosphere. In addition to the clear societal interest in understanding precipitation for water resources and disaster preparation, evaluation of each water cycle component offers insight into our different modeling capabilities. Evaporation is driven initially by radiative input which comes primarily at the strong diurnal and annual frequencies. Water vapor flux convergence is an indicator of the dynamical physics that govern atmospheric motion. Precipitation is the result of processes that span many temporal and spatial scales, but is heavily parameterized in most atmospheric models. The models' atmospheric moisture content varies in reaction to these other components, but is also constrained by assimilated observations in reanalysis systems.

It has long been known that the water cycle varies between regions, but the extent and origin of these unique characteristics is not clear. Albedo, heat capacity, and angle of incidence differences at the surface affect evaporation and boundary layer stability, which in turn influence the rest of the water cycle, but aside from a general land/sea contrast these impacts are not captured well. Rather than examining each water cycle component in isolation, it is possible to take advantage of this balanced system to solve complex problems through a deduction based on processes that are more widely understood. Balances and exchanges between water cycle components also depend upon the time scale of their interactions. In general, transport limitations restrict the influence of processes on short time scales to small regions, but cross-scale interactions

are also common. For example, the low-frequency Hadley circulation is driven by high-frequency equatorial convection and creates large-scale environments that may inhibit or encourage convection.

Atmospheric modeling systems have made huge strides in recent decades, but large biases persist in many aspects of the water cycle. An emphasis on seasonal and interannual prediction has resulted in parameterizations that may be tuned to produce higher skill on these time scales at the expense of others. New evaluations and assessments of the model's hydrometeorology must accompany advancements in data assimilation techniques, increases in domain resolution, and parameterization upgrades to monitor highly sensitive parameters or unforeseen side effects. For example, current models tend to have overly-active triggering mechanisms in their convective parameterizations (Trenberth et al., 2003), leading to precipitation that is too frequent and too light but still resulting in fairly accurate seasonal totals. Because the hydrologic impact of brief, heavy rainfall events is very different than that of prolonged sprinklings, even seasonal studies must properly account for sub-seasonal processes.

Two recent research initiatives motivate this dissertation's analysis of the water cycle across relatively high-frequency time scales. First, the Coordinated Energy and Water Cycle Observation Program (CEOP; Koike, 2004) was created to explore issues in the water cycle at resolutions that enable these evaluations. An element of the World Climate Research Program initiated by the Global Energy and Water Cycle Experiment (GEWEX) and originally called the Coordinated Enhanced Observing Period, CEOP joins together international observational, modeling, and remote-sensing products for a broad inter-comparison. The Experimental Climate Prediction Center (ECPC) at

Scripps provided four sets of model output during the 2001-2004 CEOP period. Output included two reanalysis experiments that assimilated global observations and two sets of short-range forecasts initialized by these reanalyses (see Appendix 1).

Second, new satellite-derived precipitation schemes allow for the evaluation of atmospheric models over vast regions of the globe that were previously unavailable due to inadequate observations for comparison. A suite of High-resolution Precipitation Products (HRPPs) are currently being developed that allow never-before-seen continuous estimation of precipitation away from the polar regions at high temporal and spatial scales. Comparisons between models and HRPPs during the CEOP period provide useful insight into the performance of global models as well as important intercomparisons that aid the development of HRPP algorithms.

This dissertation analyzes the observed and modeled global water cycle during the CEOP period in order to demonstrate evaluation techniques and to allow direct comparisons with other models and observations. Chapter 2 examines all aspects of the water cycle on a single time scale (diurnal) over North America, examining the role of the analysis system, the effect of resolution changes, and the interactions of the atmospheric water cycle with the energy cycle and the land surface. Chapter 3 explores the comprehensive variability of a specific water cycle component (precipitation) across diurnal to annual frequencies, comparing HRPPs to reanalysis models across the globe. Chapter 4 evaluates the exhaustive component interactions of the atmospheric water cycle in a reanalysis system at distinct diurnal, annual, and intraseasonal frequencies that are not externally forced. Together, these studies reveal unique water cycle characteristics between time scales and in various regions of the world.

CHAPTER II

The Diurnal Cycle of Water and Energy over the Continental United States from Three Reanalyses

Abstract

The Continental United States summertime diurnal surface and column-integrated atmospheric water and energy components are compared among three reanalyses. The strength of the diurnal solar forcing leads to consistent phases among surface energy components across the continent and all reanalyses, but the amplitudes vary widely. This forcing has a particularly strong and direct impact on the surface energy cycle, but interacts with many aspects of the surface and column-integrated water and energy cycles through dynamical convergence, leading to large diurnal fluctuations in the atmospheric reservoir of water vapor and total dry energy. Although they are negligible on timescales greater than a year, the tendency terms of the water and energy budgets at the surface and in the atmosphere are important on the diurnal scale. The North American Regional Reanalysis (NARR) displays a diurnal circulation pattern centered over Northern Texas that links together regional patterns in the diurnal cycles of assimilated precipitation. Constructed vapor flux convergences from the National Centers for Environmental Prediction / Department of Energy (NCEP/DOE) Reanalysis-2 Global Spectral Model and the Experimental Climate Prediction Center's reanalysis using an updated Seasonal Forecast Model reproduce many of the observed regional circulation and convergence patterns, but fail to generate the appropriate diurnal precipitation, presumably due to inadequate convective parameterizations. Diurnal variations in

atmospheric energy respond not only to the direct solar forcing, but also to the resulting dynamically-forced semidiurnal thermal tide.

2.1. Introduction

The diurnal cycle is one of the Earth's fundamental cycles. Coastal sailors have long relied on diurnal circulations to push their boats out to sea in the morning and then back to harbor in the afternoon. Valley communities are aware of a diurnal shift in winds that flow up the mountains during the day and down from the mountains at night. The diurnal cycle also has a noticeable influence on precipitation. Early sailors suggested that precipitation peaked during the night over the ocean, in contrast to an afternoon peak over land, and Kraus (1963) presented evidence for this nocturnal maximum. Gray and Jacobson (1977) provided additional observational evidence of the diurnal cycle of deep convection over the oceans, linking the rainfall with the radiative effects of clouds and regional circulations. Dai et al. (1999a, 1999b) showed the sensitivity of diurnal temperature and precipitation to other components of the hydrometeorological cycle.

Wallace (1975) uncovered strong regional coherence in the diurnal behavior of United States precipitation, including an intriguing nocturnal maximum over the Midwest that stands in contrast to a general afternoon peak over most other continental regions. The most common mechanism for precipitation over continents is land-surface heating, which drives an afternoon maximum in convective instability (Yang and Smith, 2006). Exceptions to the afternoon peak in precipitation are difficult to simulate using large-scale boundary-layer and convective parameterization schemes. The reproduction of regional behaviors (especially the Midwest nocturnal maximum) remains a challenge to the modeling community; Lee et al. (2006) showed that these features cannot be

expected to disappear with higher assimilation resolution, as limitations in parameterizations can negate the benefits of higher resolution assimilations.

Diurnal variations in other components of the hydroclimate are also evident. Dai and Deser (1999) examined the diurnally varying surface wind and divergence fields and found large-scale tendencies toward onshore and upslope winds during the day, with the reverse at night. Their study also found interactions between the wind field and variations in temperature and cloud cover. Dai et al. (1999b) further found diurnal variations in static instability, as well as a tendency toward surface convergence over the Midwest corresponding to the onset of that region's nocturnal precipitation maximum. Lindzen (1967) linked the diurnal cycle of upper-level winds, divergence, and temperatures to an atmospheric tide driven by the absorption of shortwave radiation by water vapor and ozone.

Global understanding of the diurnal cycle is complicated by data-sparse regions over the oceans and in the Southern Hemisphere, and a general deficiency of upper-air data, although satellite observations are improving our knowledge. Satellite observations also confirm a global land/sea contrast in the time of peak precipitation, with a nocturnal maximum over the ocean and an afternoon peak over most land regions (e.g. Yang and Smith, 2006). Exceptions, however, are common and merit further study, including variations in peak time near mountains and coastlines.

The ability to accurately represent the diurnal cycle of precipitation is a good test of a model's hydrometeorologic parameterizations, as precipitation is highly sensitive to errors in other components of the water and energy cycles. Randall et al. (1991) demonstrated that a GCM can reproduce many of the dominant diurnal features for

precipitation. Their simulation produced a broad afternoon maximum over land during rainy seasons, as well as an early morning maximum over the oceans. Data assimilation models (e.g. Lim and Suh, 2000) have also shown similar patterns over a global domain. In addition, the monsoonal precipitation amounts in Randall et al. (1991) were reduced when the diurnal cycle was omitted. Wilson and Mitchell (1986) had previously shown that increasing the temporal resolution of a model had a significant impact on its performance mainly due to better representation of the diurnal cycle.

The simulation of the diurnal cycle challenges the representation of cloud cover affecting the radiative balance, turbulent fluxes near the surface, dynamical reaction to the diurnal signal, and convective parameterizations driving precipitation. The diurnal cycle significantly impacts the model's water and energy balances, and therefore offers a temporal scale to examine major atmospheric balances and assess model deficiencies. As rainfall is highly sensitive to many of the reservoir and flux terms of the water and energy budget, successful depiction of the precipitation diurnal cycle requires a hydrometeorologically robust model.

The evolution of three-dimensional diurnal structures also has a significant role in diurnal anomalies. Zhang (2003) showed that the diurnal cycle of a particular location may be out of phase with the boundary layer forcings if strong large-scale dynamical forcings are present. Dai et al. (1999b) found observational evidence that variations in convective available potential energy (CAPE) affected diurnal precipitation. Simulated CAPE variations were underestimated by their regional model, which could not reproduce regional circulations favorable for CAPE enhancement. In addition, the

buildup of CAPE was prematurely interrupted by parameterizations that set off convection too early in the day (see also Dai and Trenberth, 2004).

Boundary-layer and convective parameterizations have been most extensively tested in experiments with seasonal (or longer) timescales. Tunings that improve the results on monthly timescales sometimes have a negative effect on the simulation of the diurnal cycle (e.g. Lin et al., 2000). This is particularly true of diurnal precipitation, which is often too frequent but at low intensity (Trenberth et al., 2003). The statistics of extreme precipitation events, as well as wet and dry periods, are also affected (Chen et al., 1996).

The goal of this study is to assess the diurnal cycles of surface and atmospheric water and energy components over the summertime Continental United States as simulated by three reanalyses. While the exact magnitude of diurnal variation also merits study, the phase is stressed here in order to assess whether the diurnal interactions between various components are evolving in a proper manner. Particular emphasis is placed on the progression of different variables' peak times, the performance of parameterizations, and large discrepancies between simulated and observed cycles.

Section 2.2 lays out the data and methodology used to examine the diurnal cycle. A preliminary comparison between the reanalyses and observations is conducted in Section 2.3, followed by examinations of the diurnal behavior of surface energy and water components in Sections 2.4 and 2.5. The diurnal behavior of atmospheric water and energy are shown in Sections 2.6 and 2.7, respectively. Section 2.8 summarizes our results and presents conclusions.

2.2. Methodology

2.2.1. The Coordinated Enhanced Observing Period

The Coordinated Enhanced Observing Period (CEOP, Koike, 2004) provides the pragmatic framework for this study. An element of the World Climate Research Program (WCRP) initiated by the Global Energy and Water Cycle Experiment (GEWEX), CEOP joins together international observational, modeling, and remote-sensing participants for a broad inter-comparison of hydroclimate products. Participants will eventually be able to utilize extensive *in situ* observations, customized model variables, and satellite products to characterize, simulate, and predict the Earth's hydroclimate. In particular, the diverse network of *in situ* stations will provide observations at high temporal resolution for comparison to corresponding model output location time series (MOLTS) data, allowing for a broad survey of different diurnal regimes over CEOP's comparative period from July 1st, 2001, through December 31st, 2004. Also, gridded model and satellite observations will complement the station data at each reference site.

CEOP coordinates observations from 35 reference sites, located mainly within the Continental Scale Experiments of GEWEX, ranging in latitude from 71ºN to 35ºS. Many of the stations contain meteorological towers as well as full radiation and turbulent flux instrumentation. Soil temperature and moisture are monitored at many (but not all) sites. The reference sites archive the observational data at the University Cooperation for Atmospheric Research (UCAR), where quality-control procedures are run to further synthesize the observations. The CEOP comparative period was split into several Enhanced Observing Periods (EOPs), with EOP3 (representing October 1st, 2002,

through September 30th, 2003) being the most complete. While observations continue to be processed by UCAR and submitted from the reference sites, at the time of this writing one of the most substantial observation sets exists for the Atmospheric Radiation Measurement Program's Southern Great Plains (ARM SGP) site in Oklahoma, which provides an initial focus for this work.

2.2.2. Model Background

Table 1 shows the major design and parameterization differences between the three reanalyses used in this study, which are introduced in this section.

2.2.2.a ECPC Contributions to CEOP

As a contribution to the CEOP model analysis archive, the Experimental Climate Prediction Center (ECPC) provided extensive gridded and MOLTS output from the National Centers for Environmental Prediction / Department of Energy (NCEP/DOE) Reanalysis-2 (RII, Kanamitsu et al., 2002a) using the NCEP Global Spectral Model (GSM) as well as an updated reanalysis using the Seasonal Forecast Model (SFM, Kanamitsu et al., 2002b). The GSM and SFM for these analyses use a primitive equations system of virtual temperature, humidity, surface pressure, and momentum prognostic equations, resolved in the horizontal with spherical harmonics at a triangular truncation of 62 and in the vertical with 28 σ-levels (T62L28). RII utilizes the simplified Arakawa-Schubert (SAS, Pan and Wu, 1995) convection scheme, while SFM uses the relaxed Arakawa-Schubert (RAS, Moorthi and Suarez, 1992). RII's land surface is driven by the Oregon State University Land Surface Model (OSU2, Pan and Mahrt,

1987), consisting of two vertical layers in the top 2 meters of soil, while the SFM utilizes the Noah land surface model (Ek et al., 2003) with four layers in the top 2 meters. In addition, both the RII and the SFM adjust the soil moisture as dictated by the biases computed when the model precipitation is compared to observed precipitation over 5-day pentads. Updates in the interaction between the atmosphere and the land surface have since been implemented at ECPC to maintain a surface hydrologic balance between successive forecasts.

The assimilation system enables the experiments to be initialized with observed atmospheric conditions. As the model atmosphere subsequently evolves over the 6-hr analysis cycle, interactions between variables and dominant features reveal potential errors in the diurnal cycle simulations. The sea-surface temperatures are set to daily mean values in the RII, and subsequently there is no diurnal variation in skin temperature over the ocean. ECPC's model output contribution to CEOP consists of augmented 0-6hr analyses (herein referred to as RII6 and SFM6), as well as 36-hour forecasts initialized daily from the 12UTC analysis (herein referred to as RII36 and SFM36), all with 3-hour output intervals. CEOP archives these output data (and the accompanying MOLTS data, totaling ~1 terabyte for each experiment) in a centralized database in Germany at the World Data Center for Climate, Max-Planck Institute for Meteorology.

The variables provided for the CEOP experiments were selected to meet CEOP's emphasis on flux and reservoir terms for the water and energy cycles. While many of the variables correspond to the exact forecast time, many of the flux terms are the average of the previous output period. When performing harmonic analyses (see section 2.3), the instantaneous value for a forecast put out at 03UTC is placed at

03:00UTC, but the accumulated values for a forecast put out at 03UTC are placed at 01:30UTC to represent the center of the accumulated period, and likewise for the other output times. Tendency terms are calculated over a continuous 3-hr period (e.g. the tendency term for 03UTC comes from the 00UTC – 03UTC period). This model tendency then also includes the model analysis increment.

When comparing the *in situ* observations with the MOLTS data, several factors must be considered. First, a model grid point is about 1.9ºx1.9º, which typically covers a region much larger than the instrumental coverage, although sites such as the ARM SGP have multiple observations over large heterogeneous regions. While the nearest grid point location is selected for the MOLTS data, the location of the actual reference site inside this grid point varies, depending on the reference site. Second, the model surface conditions can differ drastically from the conditions at the reference site, potentially leading to different behaviors. Third, certain variables display larger regional variation, particularly in areas with large variations in elevation and ground cover.

2.2.2.b NARR

The North American Regional Reanalysis (NARR, Mesinger et al., 2006) uses the Eta model, including the Noah land surface scheme, as part of a 3-hr assimilation at 32-km resolution with 45 vertical η-levels. Mitchell et al. (2004) demonstrated significant regional improvements in a number of variables when using precipitation assimilation over the United States continent. NARR therefore uses observed precipitation in the assimilation system, nudging the latent heating toward conditions that mimicked the

precipitation observations. The three-dimensional NARR atmospheric and surface features may therefore be an improvement over the RII and SFM which only use observed precipitation to correct soil moisture. Comparisons with the NARR results also help to identify diurnal structures missed by the comparatively coarse temporal and spatial assimilation resolution of the RII and SFM-based global analyses. To facilitate comparisons in this study, the NARR output was interpolated onto the coarser horizontal resolution of the global reanalyses. The difference between instantaneous and accumulated NARR variables was also taken into account when performing the harmonic analyses.

2.2.3. Harmonic Analysis

Harmonic analysis is used in this study to emphasize general and unique behaviors of the hydrometeorological diurnal cycle. In order to generate a smooth representation of the diurnal cycle, the 3-hr and 6-hr forecasts from each analysis initialization (SFM6 and RII6, at 00UTC, 06UTC, 12UTC, and 18UTC) are combined to generate a mean day, with each value reported at the end of a 3-hr accumulation period. Because these reanalyses are initialized 4 times daily, the simulated diurnal cycle is a combination of the diurnal cycle of assimilated observations and the models' intrinsic diurnal cycle. The 36-hr forecast experiments (SFM36 and RII36, initialized once per day) remove the component of the diurnal cycle forced by assimilated observations, leaving only the models' diurnal cycle. A comparison between the diurnal cycles of the analysis and forecast experiments has therefore begun and will be reported on in a future study.

Harmonic analysis separates the relative phases and amplitudes of the cycles, which can then be reconstructed according to:

$$Q(t) \approx \overline{Q} + \sum_{h=1}^{H} A_h \cos\left(\frac{2\pi(t-\phi_h)}{P_h}\right), \qquad (2.1)$$

where $Q(t)$ is the time series for the variable of interest, $\overline{Q}$ is that variable's mean over the record, H is the number of harmonics, A_h is the amplitude of the h^{th} harmonic, t is time (in hours), ϕ_h is the phase of the h^{th} harmonic (in hours), and P_h is the period of the h^{th} harmonic (in hours). Of course, as H approaches infinity the reconstruction will exactly reproduce the variable's record, but the selection of fundamental harmonics allows focus on the diurnal and semidiurnal cycles. The semidiurnal harmonic is the highest frequency whose phase may be fit, given the 3-hourly output.

The discrepancies between a variable's harmonic reconstruction and its true record depend on the strengths of the cycles selected. Dai (2001) found that, aside from the winter season, the diurnal harmonic explains between 40-80% of the observed mean daily variance in precipitation over the continents and about 40% of the mean daily variance over the oceans. The semidiurnal harmonic is more pronounced over the oceans, accounting for 20-40% of the daily variance as opposed to 15-25% over the land.

Harmonic analysis is common among studies of the diurnal cycle, but the procedures vary. Many of the observational studies that do not utilize harmonic analysis assess diurnal character by simply referring to the time of day when a variable's mean value is at its peak (e.g. Wallace, 1975, and Nakamura, 2004), but this approach does not distinguish between cycles of diurnal, semidiurnal, and other frequencies. This

approach also is restricted by the frequency of output times, although it is beneficial because it does not restrict variability to harmonic waves.

Harmonic fitting for the model output in this study is performed by a least-squares fit of the diurnal and semidiurnal harmonic to the mean Boreal Summertime day from 2001-2003, similar to the method of Dai (2001, 2006). This summertime grouping differs slightly from convention due to the initialization of CEOP on July 1st and its ending on December 31st. This study is therefore focused on Boreal Summer defined here as July, August, and September (JAS).

The phases are shifted to local solar time (LST); defined by:

$$L = U + \lambda / 15^\circ , \qquad (2.2)$$

where L is the time in LST, U is the time in UTC, and λ is the longitude in degrees. Some variables with zero values throughout the night are best represented by a diurnal harmonic multiplied by a time-dependent step function, but these variables' harmonics feature a strong semidiurnal cycle whose phase corresponds with the diurnal peak. The second peak of the semidiurnal harmonic falls exactly at the diurnal minimum, which leaves a diurnal profile sharpened during the afternoon but with a broad, shallow, minimum at night. Thus a direct comparison of diurnal and semidiurnal amplitudes does not always reveal the relative behaviors of these natural cycles.

Although certain points' time series may be significantly fit with a single harmonic, the most appropriate diurnal cycle comes out of the sum of diurnal and semidiurnal harmonics, as many points experience a strong semidiurnal cycle which would alter the diurnal harmonic's fit if omitted. To test the goodness-of-fit for the least-squares harmonics, the variance of the mean day described by the diurnal and

semidiurnal harmonics is calculated at all points. Values below 75% are flagged and omitted from plots. This test ensures that only areas whose mean diurnal variation may be described by a strong combination of the diurnal and semidiurnal harmonics are shown, while areas with large signals at higher frequencies are removed. The 75% criterion is exceeded by many variables with strong diurnal cycles, but was chosen as a robust test to include the full scope of variables included in this study. It must be emphasized that although this study analyzes a mean day's diurnal variation, there is no guarantee that this behavior is repeated on a consistent basis.

2.3. Comparison with ARM SGP Observations

The Southern Great Plains site of the Atmospheric Radiation Measurement Program is located in portions of Oklahoma and Kansas, centered near Lamont, Oklahoma. The region is characterized by flat terrain, agricultural land cover, and wide seasonal variation in temperature and specific humidity. It is also one of the best observed areas in the world, featuring an array of instrumented stations throughout the site.

The harmonic-fit diurnal cycle of net radiation at the location corresponding to the ARM SGP site from NARR, SFM6, RII6, and the mean of the available observations are shown in **Fig. 2.1a**. As expected, all of the cycles are dominated by the solar signal and peak at local noon, although most of the model analyses overestimate the diurnal amplitude. There is disagreement among the models as to the amplitudes of the diurnal cycle of the net radiation's short- and longwave components (not shown), likely due to discrepancies between the cloud and albedo parameterizations used.

Figures 2.1b,c,d also demonstrate large differences in the treatment of turbulent fluxes between the models and the SGP observations. The models all contain the same ~1 hour phase lag from the observed noontime peak in latent heat flux, but with very different diurnal amplitudes and means. The same amplitude variation is true for the sensible heat flux, but the models all seem to do a decent job in reproducing the noontime peak observed in sensible heat flux. NARR and the SFM-based analysis underestimate the latent heat flux variation while overestimating the sensible heat flux. RII has the opposite bias, and the sign of these biases are generally consistent across the Continental United States. The peak downward ground heat flux precedes the ~13LST ARM SGP observations in all models. The SFM analysis best reproduces the observed phase, but overestimates its amplitude. The RII analysis has similar amplitude to the SFM analysis but the largest lead time. NARR has the largest amplitude in downward flux peaking just before noon. The phases of these heat fluxes correspond to within a few hours of the strong diurnal peak in net radiation. Although the turbulent fluxes are biased by a factor of ~2 from observations, the sensible and latent heat fluxes' biases of opposite signs approximately compensate each other, allowing the models to do a reasonable overall job of representing the radiant energy and surface energy budget at this location. The average of the diurnal variations of SFM6 and RII6 sensible and latent heat fluxes actually outperforms the NARR values at the ARM SGP site.

Figure 2.2 reveals that significant errors persist in the handling of the water cycle and near-surface dynamics by the global analyses. RII6 produces a mid-afternoon peak in precipitation, while the NARR successfully captures the observed nocturnal peak in the early morning hours. SFM6 lacks any significant diurnal cycle at this point, instead

precipitating at a low mean rate all day. A similar phase shift is also evident in the diurnal anomalies of the RII6 2-meter specific humidity, where the NARR data capture the strong semidiurnal component as well. The SFM6 specific humidity is too low, but the phase and amplitude of its diurnal cycle is an improvement on RII6. The near-surface winds also prove difficult to capture, with the global models shifting peak zonal winds to earlier in the morning and the RII6 creating a spurious nocturnal peak in meridional wind. The global reanalyses overestimate the mean surface winds, but the observed amplitude of diurnal variation is nearly reproduced. NARR zonal winds improve on the global models, but NARR shifts its near-surface wind peaks by almost 3 hours.

Although errors still persist in NARR's representation of the ARM SGP site, its improvement over the RII6 and SFM6 experiments suggests an improvement in overall atmospheric structures produced by increased resolution and precipitation assimilation. NARR can therefore be used as a basis for other comparisons with the RII and SFM reanalyses. The examination of individual features resolved by NARR, that the global analyses and forecasts handle poorly, are ongoing and will be the focus of a future study.

Not all of the components' diurnal variations follow a strong diurnal harmonic. **Figure 2.3** shows the diurnal variations of column-integrated energy components (see discussion in section 2.7 below about the influence of thermal tides) at the location corresponding to ARM SGP in SFM6 and RII6. The short- and longwave heating are dominated by the diurnal harmonic, but the tendency and divergence terms are strongly semidiurnal with the diurnal harmonic acting to enhance one of the two semidiurnal maxima.

2.4. Surface Energy

The surface energy budget is given by:

$$0 = Q_r - Q_H - L_E + Q_G \,, \qquad (2.3)$$

where Q_r is net radiation influx, Q_H is sensible heat flux, L_E is the latent heat flux, and Q_G is ground heat flux (out of the 2-meter subsurface layer being positive). There is no separate tendency term in this budget, as the longwave radiation implicitly contains the variation of skin temperature. The surface energy is therefore potentially dependent on (among others): mean cloud cover, surface albedo, mean surface temperature, mean surface specific humidity, mean surface winds, elevation, soil moisture, and soil type. The mean NARR values of sensible and latent heat fluxes are shown in **Fig. 2.4**, along with the 2-meter temperature and planetary boundary layer (PBL) height, which are strongly affected by the surface energy budget. As these all vary significantly over the contiguous United States, their diurnal phases could potentially also vary significantly, but in these simulations they show remarkable horizontal agreement.

The diurnal variations in the remaining sections are plotted utilizing a vector representation, with the vector's length corresponding to the amplitude of the diurnal variation, and the direction of the vector indicating the local time of the peak diurnal value (a vector pointing North corresponds to local midnight, a vector pointing East corresponds to local 6AM, etc.). The vectors were also scaled to show the relevant information in a clear manner. The unit vector (denoted by a bold line in the Southwest corner of each panel) represents the same reference magnitude in each panel for a particular variable, but the length varies depending on the relative magnitudes in each panel. A panel displaying larger diurnal amplitudes than the others will have a shorter

unit length, shortening the vectors displayed to prevent overlap. A panel displaying smaller diurnal amplitudes than the others will have a longer unit length, lengthening the vectors to make them more legible. Each plot should be examined with reference to the unit vector in order to make visual comparisons between reanalyses.

The solar insolation that drives the diurnal cycle has a particularly strong effect on the land surface. As most of the shortwave energy passes through the atmosphere with little absorption, the strongest diurnal forcing occurs via a regular radiative imbalance at the Earth's surface, and is reflected in all the terms of the surface energy budget. The phase and diurnal magnitude anomaly of each of the reanalyses' diurnal cycle of sensible heat flux across the continental United States is shown in **Figs. 2.5a,b,c**, featuring a peak almost exactly at noon LST over the entire land surface. A similar uniformity is also seen in the phases of latent heat flux (**Figs. 2.5d,e,f**) across the land surface, although each simulation has a slightly different lag from local noon (RII6 being the largest at ~1 hour). As expected, the amplitude of sensible heating is correlated with warmer and drier regions in all reanalyses, while the latent heating is anti-correlated to these conditions (although very subtly in the SFM reanalysis). In addition, there appears to be a slight lag in peak time over dry regions for both sensible and latent heat flux in all simulations, although it is not significant at this temporal resolution. To disperse the midday excess in surface energy, the turbulent flux terms in each reanalysis follow a nearly universal phase locked to the surface insolation which dominates over secondary influences like geographical variations in temperature, humidity, elevation, or soil types. The distinctive diurnal features are therefore direct responses to the regular solar signal, and show little variation due to anything else.

The oceans in these simulations do not contain diurnally-varying sea surface temperatures (an effect mimicking the larger heat capacity of the water), which removes the diurnal role of radiative energy in determining the evolution of the turbulent fluxes. The lack of a dominant shortwave signal allows the geographical anomalies in diurnally varying air temperature and humidity to play a larger role, although the amplitudes over water are markedly decreased. In most locations, the phases appear to follow the temperature gradient between the (diurnally constant) sea surface and the lower atmosphere, which reaches a maximum when the lower atmospheric temperature is at its minimum in the hours before sunrise. The large values of RII6 latent heating in the Gulf of Mexico are due to an error in SST interpolation (corrected for SFM6) of a coarse grid in such a region of high-resolution terrain, leading to much warmer skin temperatures in that area. The diurnal variation of the ground heat flux (not shown) is small in comparison to the other components.

Figure 2.6 demonstrates that the solar signal drives a uniform reaction over land in the 2-meter air temperature, which peaks around 15LST in the NARR and SFM6 and at ~16 LST in the RII6. The peak lags noon LST because the temperature continues to rise as long as the sum of the turbulent fluxes carrying energy away from the surface is less than the net radiative input, even as the sun lowers in the sky. In a similar manner, the minimum occurs just before sunrise. Again, geographic variations in phase due to vegetation, elevation, and moisture are dominated by the phase of the radiative flux.

The consistency in phase for the height of the PBL over land in **Figs. 2.6d,e,f** suggest that the solar forcing extends its diurnal impact into the lower atmosphere. The discrepancies between the simulations demonstrate alternate effects of the raised

elevation, which delays the peak in the NARR simulations but is generally indistinguishable in phase from the rest of the land points in SFM6 and RII6. Both of the global reanalyses use the Hong and Pan (1996) nonlocal-K PBL parameterization, but different land surface models lead to different diurnal behaviors in PBL height, depending on the Richardson number as well as the near-surface temperature and humidity profiles. Both lead the NARR PBL peak by several hours (due possibly to higher mean PBL heights using NARR's modified Mellor-Yamada level-2.5 scheme, Janjić, 1996), with SFM6 peaking ahead of RII6. The overall phase differences between models suggest a premature decline in the boundary layer in the global simulations, which mimics an inability to produce significant static instability due to overly sensitive convective parameterizations as noted by Dai and Trenberth (2004). Although it is beyond the scope of this investigation, it would be of interest to compare these experiments with other analyses and radiosonde observations.

The amplitudes of the diurnal cycles of 2-meter temperature and planetary boundary layer height are more indicative of how regional influences affect the reanalyses' diurnal cycle. NARR's 2-meter temperatures have their highest amplitudes over the Great Plains east of the Rockies, while the planetary boundary layer has its highest diurnal variation over the elevated regions where its mean height is the largest. SFM6 2-meter temperatures have a high bias in diurnal amplitude compared to NARR and RII6, while RII6 underestimates the planetary boundary layer height amplitudes seen in the other reanalyses. Despite these different general biases, the global simulations feature higher diurnal amplitudes over the dry, elevated regions for both variables, as the

radiative components are amplified where diminished latent heating leads to reduced specific humidities.

2.5. Surface Water

The surface water balance is governed by:

$$\frac{\partial s}{\partial t} = P - E - N \,, \qquad (2.4)$$

where $\frac{\partial s}{\partial t}$ is the tendency of total surface water (in the soils and snow pack), P is precipitation, E is evaporation, and N is total runoff (on surface and base flow in the soil). As shown in the previous section, the phase of the evaporation is determined by the solar insolation, which dominates over other regional influences. Runoff in all three reanalyses does not have a significant diurnal cycle.

NARR's mean surface water amount (soil water plus snow pack) and precipitation (**Fig. 2.7**) show significant regional variations. The SFM reanalysis slightly underestimates rainfall in comparison to NARR, particularly in the Upper Great Plains region west-southwest of the Great Lakes. The southeastern United States and Mexico are very rainy in the RII reanalysis, and the positive bias extends over most of the domain. The competing biases in mean precipitation between the global reanalyses are most likely due to their convection schemes.

Surface water tendency has a negligible magnitude over long (>seasonal) timescales in comparison to the other components of the surface water budget, but this is not true on diurnal timescales. The diurnal variation in total surface water tendency (**Figs. 2.8a,b,c**) responds to sporadic precipitation events as well as a daily evaporation

cycle driven by the radiative forcing. Although the precipitation events cause the largest jumps in surface water, the fitted harmonics reflect the most common diurnal variation and show a negative tendency throughout the daytime with a peak near local noon when evaporation is almost a maximum. The OSU2 scheme in RII6 shows very little regional differences in diurnal amplitude, but the Noah land-surface scheme (NARR and SFM6) shows higher amplitudes in the wetter regions.

Figures 4.8d,e,f display the diurnal cycle of precipitation rate as simulated by the three reanalyses. It is immediately evident that precipitation is not solely dependent on the diurnal solar forcing, as significant regional differences in phase and amplitude are clear in all simulations. NARR's assimilated precipitation features a late-afternoon peak over most land areas, but also matches Wallace's (1975) nocturnal maximum in the Upper Midwest. Peak precipitation rates in the late-afternoon over the Rocky Mountains have increasingly lagged phases traveling eastward across the Great Plains, indicative of propagating thunderstorm activity culminating in a peak near sunrise over the Great Lakes region (see Carbone et al., 2002). Lee mountain waves, moisture transport through a nocturnal low-level jet, and the influence of Rocky Mountain circulations can all impact the phase of precipitation in this area, but each are complex diurnal features that are difficult to simulate.

The propagation of mesoscale storms across the Great Plains fits nicely into a circulation of diurnal precipitation centered over Northern Texas and Oklahoma. The vectors of diurnal precipitation spiral around (and always away from) this point (with the exception of the southeastern states), indicating the influence of an anomalous anticyclonic circulation that drives the arrival of precipitation. Beginning with peak

precipitation before noon over the Northwest Gulf of Mexico, the time of peak precipitation arrives progressively later in the day around this circulation all the way to the Great Lakes region. The most likely source of this circulation is the influence of a diurnally-driven low-level jet which supplies moisture to the Great Plains region from the Gulf of Mexico (Higgins et al., 1997a, 1997b) and is part of an anomalous anticyclonic diurnal circulation centered slightly to the east of the Great Plains LLJ (similar to the simulations of Schubert et al.,1998).

In contrast to NARR's assimilated precipitation, the SFM6 and RII6 do not produce the regional diurnal precipitation features over the land. Instead, a consistent early-afternoon peak over the continent occurs in both simulations. Both the simplified and relaxed Arakawa-Schubert schemes initiate convection prematurely, resulting in a release of convective available potential energy (CAPE) despite the influence of inhibiting afternoon divergence in some regions. This is a typical problem with convective parameterizations (see e.g. Dai et al., 1999b). The simulated diurnal cycle therefore follows a consistent diurnal pattern in producing the seasonal means, altering the diurnal amplitude for regions with different means and reanalyses with wet biases. The resulting precipitation statistics are too frequent and too light in intensity on near-diurnal timescales (as noted by Trenberth et al., 2003). In the SFM analysis, much of the central and western regions appear to act in a similar fashion as the ARM SGP grid point (recall Fig. 2.2a), with an overactive convective trigger leading to very little diurnal variation.

The surface water balance is an interesting test for hydrometeorological models, as accurate simulation requires proper land-surface, radiation, boundary-layer, and

convective schemes. Surface water and evaporation are mostly isolated from the atmosphere above the boundary layer, but precipitation is dependent on diurnal dynamics and parameterizations that affect the column water budget. Convective parameterizations need to balance between large-scale and boundary-layer forcings (Zhang, 2003). In the RII6 and SFM6, the surface properties tend to overpower the subtle changes in column dynamics and vapor convergence in the Arakawa-Schubert based schemes. The implementation of these schemes was designed to produce the desired long-term means over the Continental United States, but they do so at the expense of good statistics of higher frequency physical processes which may be important in predicting the impacts of various climate scenarios.

2.6. Atmospheric Water

The water vapor in the atmospheric column follows:

$$\frac{\partial\{q\}}{\partial t} = -\nabla \bullet \{vq\} + E - P, \qquad (2.5)$$

where $\frac{\partial\{q\}}{\partial t}$ is the tendency of precipitable water and $-\nabla \bullet \{vq\}$ is the water vapor flux convergence (curly braces indicate the column integral). As was shown in section 2.4 above, the atmosphere receives a regular influx of moisture from the surface which peaks ~1 hour past local noon regardless of continental location. The remaining terms of the atmospheric water budget are also influenced by diurnally varying structures affecting transport and vertical structure, as well as simulation errors introduced through the influences of cloud and convection parameterizations.

Figure 2.9 shows the mean values of precipitable water, vapor flux convergence, and 10-meter wind components from NARR. Despite differences in mean precipitation biases, both global reanalyses feature dry biases in the atmospheric column's precipitable water. NARR's 10-meter meridional winds show patterns similar to low-level jets (LLJs) over the Great Plains and off of the Gulf of California, although Mo et al. (2005) show that the Gulf of California LLJ is systematically overestimated by NARR. The traces of these LLJs are also seen in SFM6 and RII6, although the Great Plains LLJ region is strengthened (particularly in RII6) and the Gulf of California LLJ is diminished. Anomalies between the mean wind fields are more common over regions with complex terrain (e.g. the Rocky Mountains), where the coarse spatial resolution in the global analyses is not able to resolve topography features as well as the much higher resolution in NARR.

Over long (>seasonal) periods, the precipitable water tendency term becomes negligible compared to large accumulated values balancing evaporation, precipitation, and moisture convergence, but this is not true on diurnal time scales (similar to surface water tendency). **Figure 2.10** reveals that precipitable water tendency is the same order of magnitude as precipitation and evaporation, exceeding both in many locations. This variation is larger than that observed by Dai et al. (2002) using GPS methods over North America. Over most of the continent the precipitable water tendency peaks between 12LST and 18LST. RII6 precipitable water acts very similarly to the latent heat flux (Fig. 2.5d,e,f) on the diurnal scale, peaking ~13LST over wet regions with consistent evaporation and later in arid regions where strong evaporation is more sporadic and other components of the water cycle play a larger role. NARR and SFM6 feature a similar

pattern, although the diurnal cycles are not significant over most of the areas with low diurnal evaporation variation in NARR. The largest diurnal amplitudes in SFM6 occur over the North American Monsoon region (Gutzler et al., 2005).

The diurnal cycles of water vapor flux convergence are shown in **Figs. 2.10d,e,f**. NARR computes vapor flux convergence every time step and records accumulated values in its 3-hourly output. The global reanalyses compute moisture convergence from instantaneous values of vapor and winds every three hours (see e.g. Roads et al., 2002), but linear interpolations of this infrequently derived quantity yielded relatively large errors in the diurnal balance of atmospheric water (*Eqn. 2.5*). For this study, a more exact residual vapor flux convergence was therefore calculated at each 3-hourly output time as the remainder term that would balance the accumulated precipitation, evaporation, and the tendency (forecast) term. The resulting diurnal patterns are quite similar to the accumulated NARR vapor flux convergence. As expected, the vapor flux convergence over the arid southwest appears to be the primary driver of the precipitable water tendency in that region.

The regional pattern of diurnal vapor flux convergence in NARR shows the same circulation seen in the assimilated precipitation (Figs. 2.7d,e,f). A similar circulation was first suggested by Rasmusson (1967). This suggests that the timing of diurnal precipitation is most strongly determined by anomalous dynamical convergence in the moist lower atmosphere. The nocturnal precipitation maximum in the Upper Midwest corresponds to nocturnal moisture convergence likely supplied by the Great Plains low-level jet, which bisects the precipitation circulation affecting a large portion of the Continental United States.

Surprisingly, the residual vapor flux convergences produce nearly identical regional patterns in the global reanalyses, although they cannot reproduce the patterns in diurnal precipitation. Examined as a whole, the global reanalyses reproduce the basic patterns of NARR evaporation, precipitable water tendency, and vapor flux convergence, but fail to generate the pattern in the remaining component (precipitation). Again, the convective parameterizations are most likely to blame, placing too much emphasis on diurnal variations in energy (e.g. CAPE) at the expense of what appears to be the true dynamical forcing.

The low-level jet is only one of many diurnally forced dynamical anomalies. **Figure 2.11** shows large regional patterns in the diurnal variation of 10-meter winds. The most prominent patterns show the well-documented mountain/valley and land/sea circulations, with air flowing upslope and onshore during the afternoon and downslope and offshore in the morning. The patterns are similar among all of the reanalyses, although the global reanalyses feature larger diurnal amplitudes. Preliminary examinations of diurnal dynamical anomalies throughout the atmospheric column (not shown) reveal complex three-dimensional features on many spatial scales. While the Arakawa-Schubert based parameterizations overwhelm the influence of these dynamical features, they likely have significant impacts on diurnal precipitation patterns.

2.7. Atmospheric Energy

Atmospheric energy is balanced through

$$\frac{\partial\{C_pT + KE\}}{\partial t} + \frac{\partial \pi}{\partial t}\phi_s = -\nabla \bullet \{v(C_pT + \phi + KE)\} + Q_H + LP + \{Q_r\}, \qquad (2.6)$$

where C_p is the specific heat of air with respect to pressure, T is temperature, KE is kinetic energy, π is total atmospheric mass, ϕ_s is the surface geopotential, and LP is the latent heat released throughout the column by precipitation. The left-hand side of *Eqn. 2.6* represents the tendency of thermal, kinetic, and potential energy (herein referred to as the total dry energy), and the first term on the right-hand side represents the convergence of total dry energy. As discussed in previous sections, sensible heat input to the atmosphere regularly follows a noontime peak, and the latent heat released by precipitation is large but sporadic.

The SFM6 and RII6 experiments have been extensively post-processed to produce the column-integrated atmospheric energy variables that allow an examination of the atmospheric energy budget, which cannot be easily performed on the available NARR output. This section is therefore restricted to the global reanalyses. **Figure 2.12** shows SFM6's mean values of column-integrated longwave cooling and shortwave heating, as well as the total dry energy and its divergence. Due, in part, to the reduced size of the atmospheric column, the radiation and total dry energy values are lower over elevated terrain. Dry energy divergence seems to be amplified over warmer regions.

As mentioned in section 2.4, the bulk of diurnal forcing occurs at the surface as the atmosphere is mostly transparent to solar radiation. Although the atmosphere experiences a negative mean net radiative heating due to longwave emission (not shown), **Fig. 2.13** shows a peak in the diurnal cycle of total radiative heating (i.e. a minimum in atmospheric radiative cooling) shortly after noontime in the global reanalyses. The individual components of atmospheric radiative heating, however, display different diurnal behaviors. The shortwave heating generates a positive noontime peak

coincident with maximum solar angle, and is zero during the nighttime. The longwave heating corresponds to the mid-afternoon peak in surface temperature (recall Fig. 2.6a,b,c), but is much smaller in diurnal amplitude and never is large enough to cause positive longwave heating. Although the mean atmospheric longwave cooling dominates the mean radiative heating, the diurnal variation of shortwave heating dominates the diurnal variation. The diurnal behavior of net radiative heating therefore has the same amplitude as the shortwave heating and a very similar phase, but the phase is lagged slightly by the longwave variation. In both reanalyses, the low diurnal temperature range over the oceans diminishes the diurnal cycle of the longwave emission, resulting in noontime peaks in the net radiative heating.

The diurnal cycle of total dry energy is driven not by the radiative input, but by the dynamical response to uneven heating across the globe. As the diurnal solar forcing heats up water vapor and ozone over the daytime face, thermal expansion forces pressure anomalies which lead to a semidiurnal thermal tide (as described by Lindzen, 1967). The resulting semidiurnal geopotential variations are the strongest element of the diurnal cycle of total dry energy in the global reanalyses. The thermal tide leads to a minimum in pressure during the warmest portion of the day (Dai and Wang, 1999), as the mean stability of the atmosphere causes thermally expanding air to horizontally diverge. The reanalyses reflect this behavior in **Fig. 2.14a,b**, as the total dry energy divergence (constructed in the same manner as the constructed vapor convergence in section 2.6) peaks in the late afternoon. By including the full atmospheric column, the results presented in this study reflect the semidiurnal influence of the upper atmosphere, which dominates over the diurnal surface convergence (see Fig. 2.11). Interaction with the

land surface enhances the diurnal nature of total dry energy in the lower atmosphere over the land, but over the ocean (with diurnally constant sea surface temperatures) either semidiurnal peak may be larger. Over portions of the Gulf of Mexico and Atlantic Ocean where the diurnal influence is weak, adjacent vectors point in opposite directions (indicating 12 hour differences in peak time), reflecting the similarity in amplitude between morning and afternoon semidiurnal maxima.

Atmospheric dry energy tendency peaks in the morning ~6 hours before the afternoon maximum in divergence (see **Figs. 2.14c,d**). The maximum total dry energy values are reached shortly after noon, but before the afternoon maximum temperatures are reached. This maximum is caused by the backward convergence of air leading to a thermally driven high pressure tide, as well as the rising sun beginning to heat the atmosphere. This atmospheric total dry energy maximum is therefore the constructive interference of the diurnal nature of sensible and solar radiative heating as well as the semidiurnal convergence due to the thermal tide. The amplitudes of both the convergence and tendency of total dry energy are largest at low-latitudes, where the strength of the solar forcing causes large thermal tides.

2.8. Summary and Conclusions

Diurnal cycles of water and energy from NARR, SFM6, and RII6 were examined over the summertime Continental United States. A least-squares fit of diurnal and semidiurnal harmonics to a mean day allows for a smooth representation of the diurnal variation. The phase and amplitude of this smoothed cycle characterize the diurnal behavior of the major components of water and energy.

A preliminary comparison with CEOP observations from the ARM SGP site shows some agreement between fundamental surface energy components, but broad disagreement among water cycle components affected by diurnal dynamical structures and the convective parameterizations. The turbulent fluxes (and other surface energy variables) show remarkable consistency in their phases across various regions with unique land types, although the models with the Noah land-surface scheme show, perhaps, more appropriate regional differences in diurnal amplitude. Further comparisons with CEOP observations, as the data become available, in diverse regions will be useful for model evaluations.

The simulated water cycle is strongly affected by regional diurnal circulations, atmospheric convergence, and parameterizations of convection, clouds, and the boundary layer. Despite their coarser resolution, SFM6 and RII6 reproduce the diurnal circulation of vapor convergence centered in Northern Texas and Oklahoma seen in NARR. Their diurnal precipitation patterns, however, lose the distinct regional behaviors seen in assimilated NARR precipitation due to overactive convective parameterizations. The global reanalyses' Arakawa-Schubert based schemes may perform fairly well on seasonal and longer timescales, but overpower subtle driving mechanisms on diurnal precipitation, resulting in a consistent early-afternoon peak and the inhibition of mature convective environments.

Atmospheric total dry energy follows a strongly semidiurnal behavior, driven by solar tides in the upper atmosphere. Isolated from the surface on the diurnal timescale, total dry energy does not show strong regional behaviors due to underlying surface features, aside from an enhanced diurnal contribution in the lower atmosphere over land.

The tendencies of surface water, precipitable water, and atmospheric total dry energy are on the same scale as standard components of their respective diurnal budget equations. Although they are negligible over longer periods, they are significant on the diurnal scale, and can offer great insight into the nature of these cycles.

Among the two global reanalyses (SFM6 and RII6), SFM6 generates more regionally unique behaviors. Its results also more closely mimic NARR, although this may be due to a land-surface scheme (Noah) common to both models. The mostly improved performance of SFM6 over RII6 is gratifying as it is a somewhat newer generation modeling system, and thus would appear to be the best ECPC global reanalysis submitted to the CEOP database for water and energy budget comparisons, although the RAS convective parameterization does not appear to perform as well as SAS.

Many model structures were designed for studies on longer timescales, but the diurnal variations reveal weaknesses in diurnal dynamics and parameterizations that affect stability, convection, and the land-atmosphere interface. Improvements in resolution alone will not solve all of these diurnal problems. Finally, an improved diurnal cycle will improve the statistical distribution of events ranging from hours to weeks in simulations, allowing a better representation of how today's (and tomorrow's) climate affects society.

2.9. Acknowledgements

The text of this chapter, in full, has been published by A.C. Ruane and J.O. Roads in the *Coordinated Enhanced Observing Period* special issue of the *Journal of the*

Meteorological Society of Japan, **85(**2**)**, 117-143. The dissertation author was the primary investigator and author of this paper. The coauthor listed in this publication was fundamental to the research which forms the basis of this chapter. This work was supported by NOAA NA17RJ1231 and NASA NNG05GR40G grants and received partial support from the California Space Institute (CSI) and California Space Grant Consortium (CSGC). The views expressed herein are those of the authors and do not necessarily reflect the views of NOAA, NASA, CSI or CSGC. The authors would like to thank Masao Kanamitsu for his updates to the SFM and frequent advice. We would also like to thank Jack Woollen and Wesley Ebisuzaki for providing the raw files needed for the SFM reanalysis, and Martin Olivera and Jack Ritchie for providing technical support. The authors appreciate the significant contributions from many CEOP participants, especially those who participate in the periodic model output teleconferences. Finally, the authors thank the reviewers and editors for their help in revising this paper.

Table 2.1: Settings and parameterization schemes for the three reanalyses.

	ECPC Seasonal Forecast Model (Kanamitsu et al., 2002a)	**NCEP/DOE Reanalysis-2** (Kanamitsu et al., 2002b)	**NCEP North American Regional Reanalysis** (Mesinger, 2006)
Domain	Global	Global	North America
Resolution	T62, 28 sigma levels	T62, 28 sigma levels	32 km, 45 eta layers
Shortwave Radiation	Chou, 1992; Chou and Lee, 1996	Chou, 1992; Chou and Lee, 1996	Lacis and Hansen, 1974
Longwave Radiation	Chou and Suarez, 1994	Fels and Schwarzkopf, 1975	Fels and Schwarzkopf, 1975
Convection	Relaxed Arakawa-Schubert (Moorthi and Suarez, 1992)	Simplified Arakawa-Schubert (Pan and Wu, 1995)	Betts-Miller-Janjić (Janjić, 1994) Assimilated Precipitation
Clouds	Slingo, 1987	Campana et al., 1994	Zhao et al., 1997
Planetary Boundary Layer	Nonlocal-K (Hong and Pan, 1996)	Nonlocal-K (Hong and Pan, 1996)	Mellor-Yamada, 1982 Mesinger, 1993; Janjić, 1996
Land Surface	Noah 4-layer (Ek et al., 2003) Soil Moisture Adjustment	OSU 2-layer (Pan and Mahrt, 1987) Soil Moisture Adjustment	Noah 4-layer (Ek et al., 2003) Assimilated Precipitation
Vegetation	USGS Monthly Variations	Fixed Vegetation Cover	USGS Monthly Variations
Soils	9 Soil Types	15 Soil Types	9 Soil Types
Orography	Smooth Mean	Smooth Mean	Silhouette/mean, unsmoothed

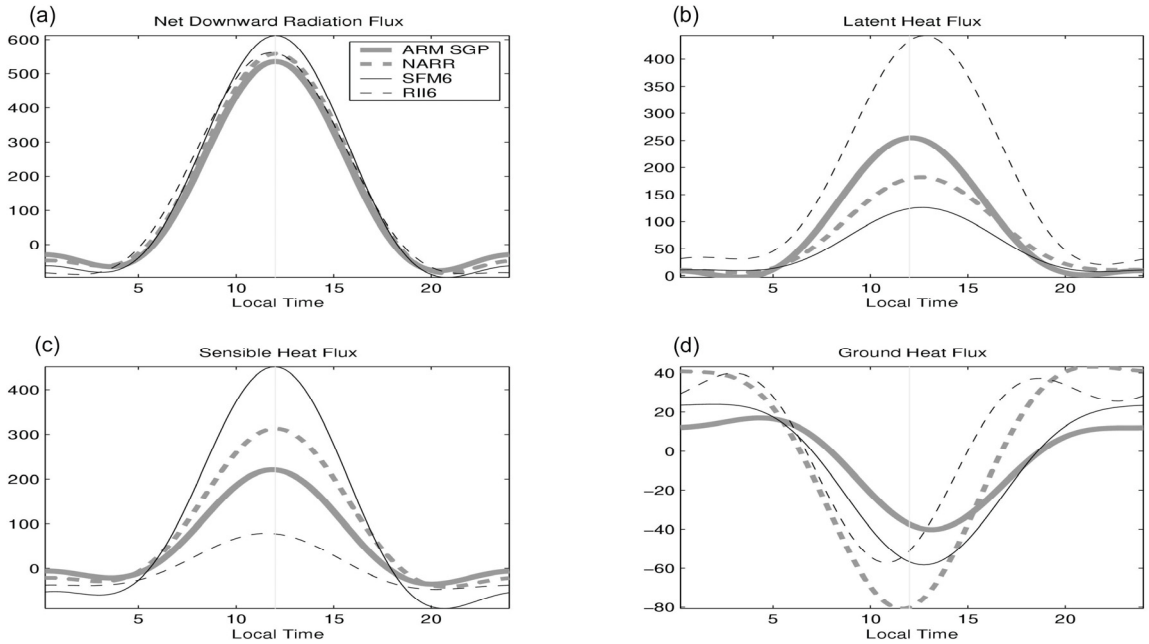

Figure 2.1: The diurnal variation of **a)** net downward radiation flux, **b)** latent heat flux, **c)** sensible heat flux, and **d)** ground heat flux (W/m^2) as fitted harmonics from July, August, and September (JAS) 2001-2003 from NARR, SFM6, and RII6, as well as JAS 2003 from the ARM SGP Observations. The light vertical line represents local noon.

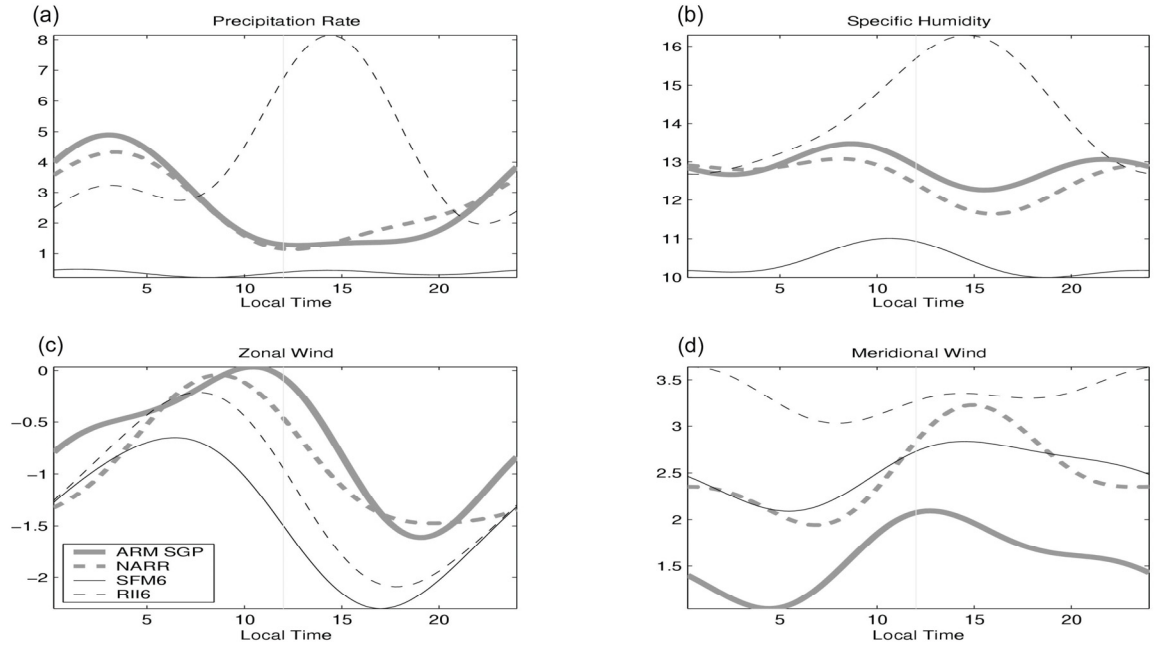

Figure 2.2: As in Fig. 2.1, but for **a)** precipitation rate (mm/day), **b)** 2-meter specific humidity (g/kg), **c)** 10-meter zonal winds (m/s), and **d)** 10-meter meridional wind (m/s).

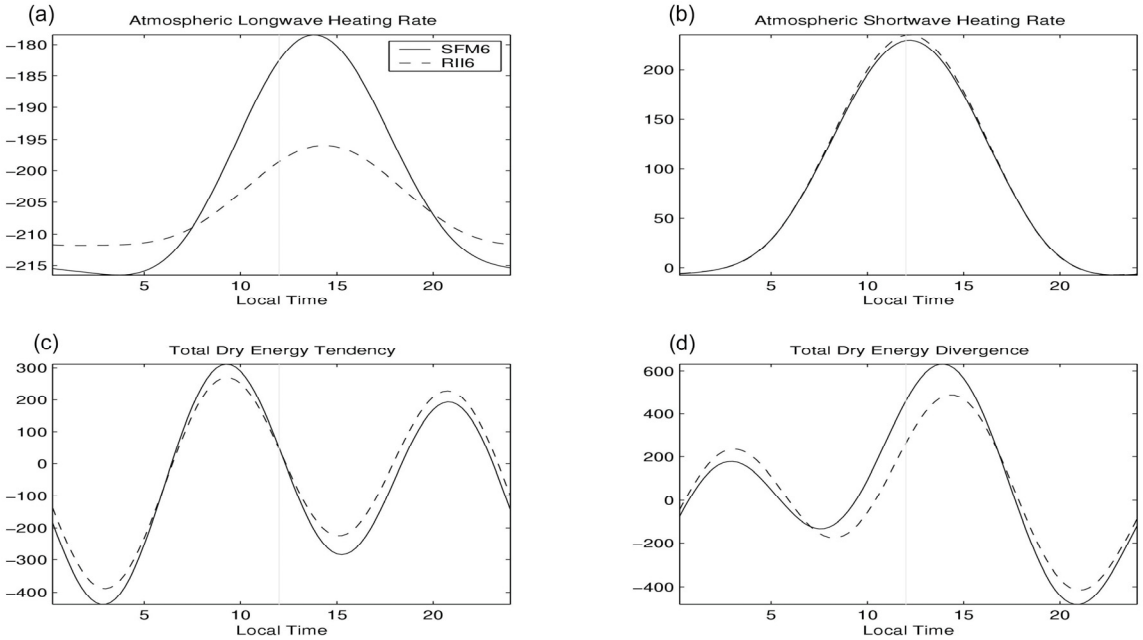

Figure 2.3: As in Fig. 2.1, but for **a)** atmospheric longwave heating rate, **b)** atmospheric shortwave heating rate, **c)** total dry energy tendency, and **d)** total dry energy divergence. These components are only available in the global reanalyses. (W/m^2).

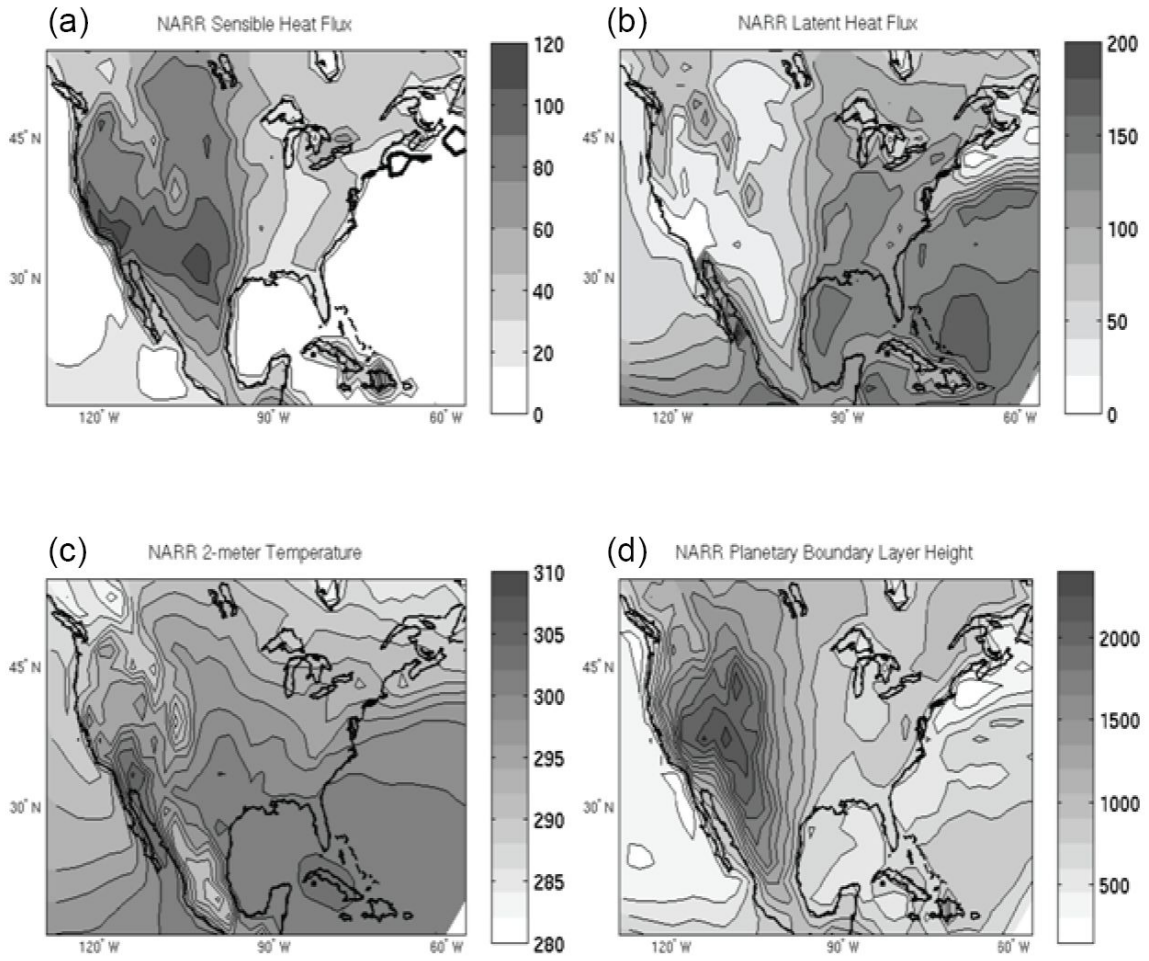

Figure 2.4: NARR July, August, and September 2001-2003 mean (**a**) latent and (**b**) sensible heat fluxes (W/m^2), (**c**) 2-meter temperature (K) and (**d**) planetary boundary layer height (m). Dashed lines indicate negative contours, and the bold line is the zero contour.

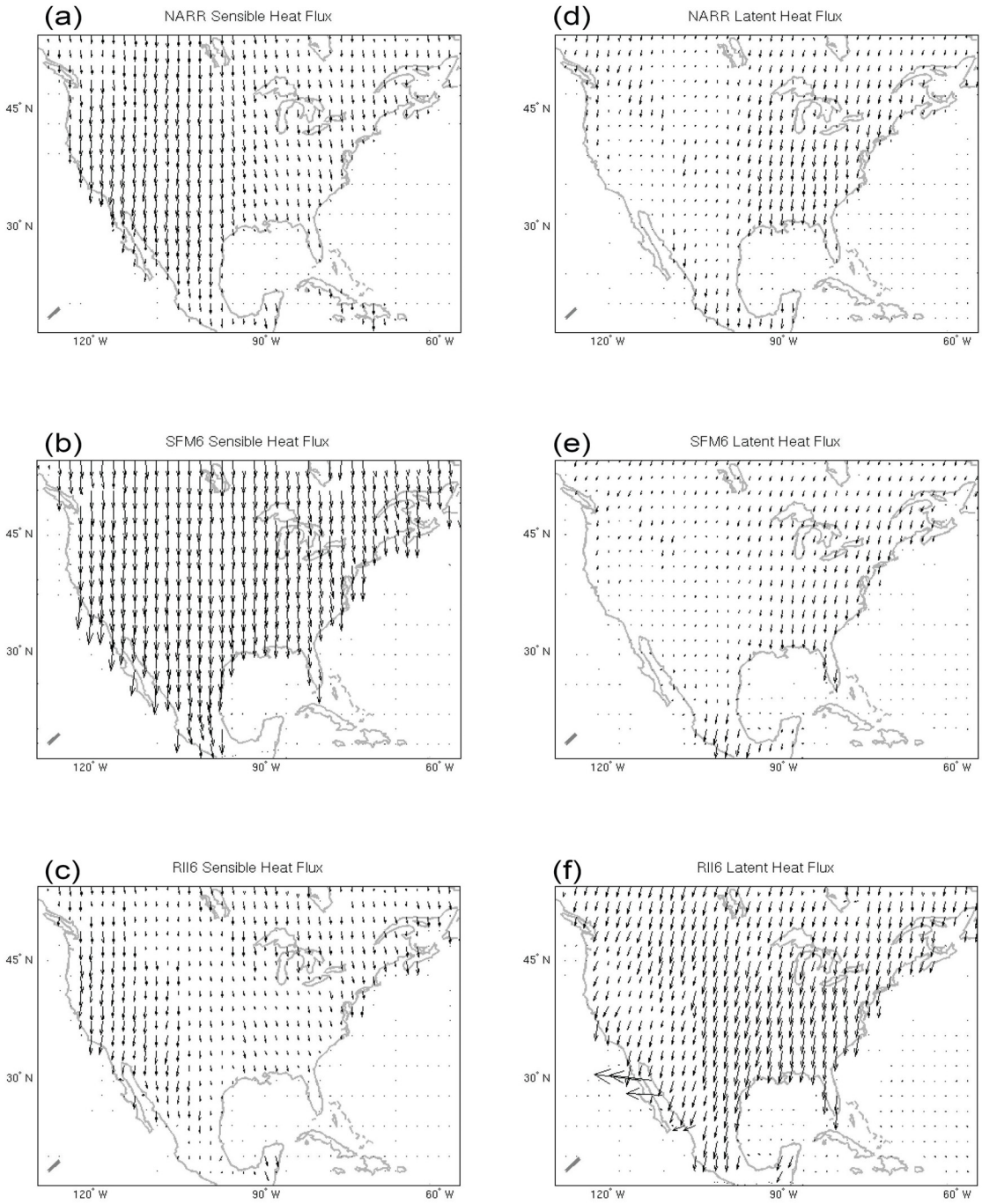

Figure 2.5: The diurnal cycles of sensible heat flux (**a**, **b**, and **c**) and latent heat flux (**d**, **e**, and **f**) from NARR (**a** and **d**), SFM6 (**b** and **e**), and RII6 (**c** and **f**), expressed as a vector whose length corresponds to the amplitude of the peak diurnal anomaly, and whose phase corresponds to the local time of that peak (a vector pointing North corresponds to a peak at local midnight). The sensible heat vectors are all scaled to a reference length of 250 W/m^2, while the latent heat vectors are scaled to 200 W/m^2, represented by the bold line in the southwest corner of each panel. Note that, for clarity, the unit vector in **f** is lengthened to make smaller values more visible.

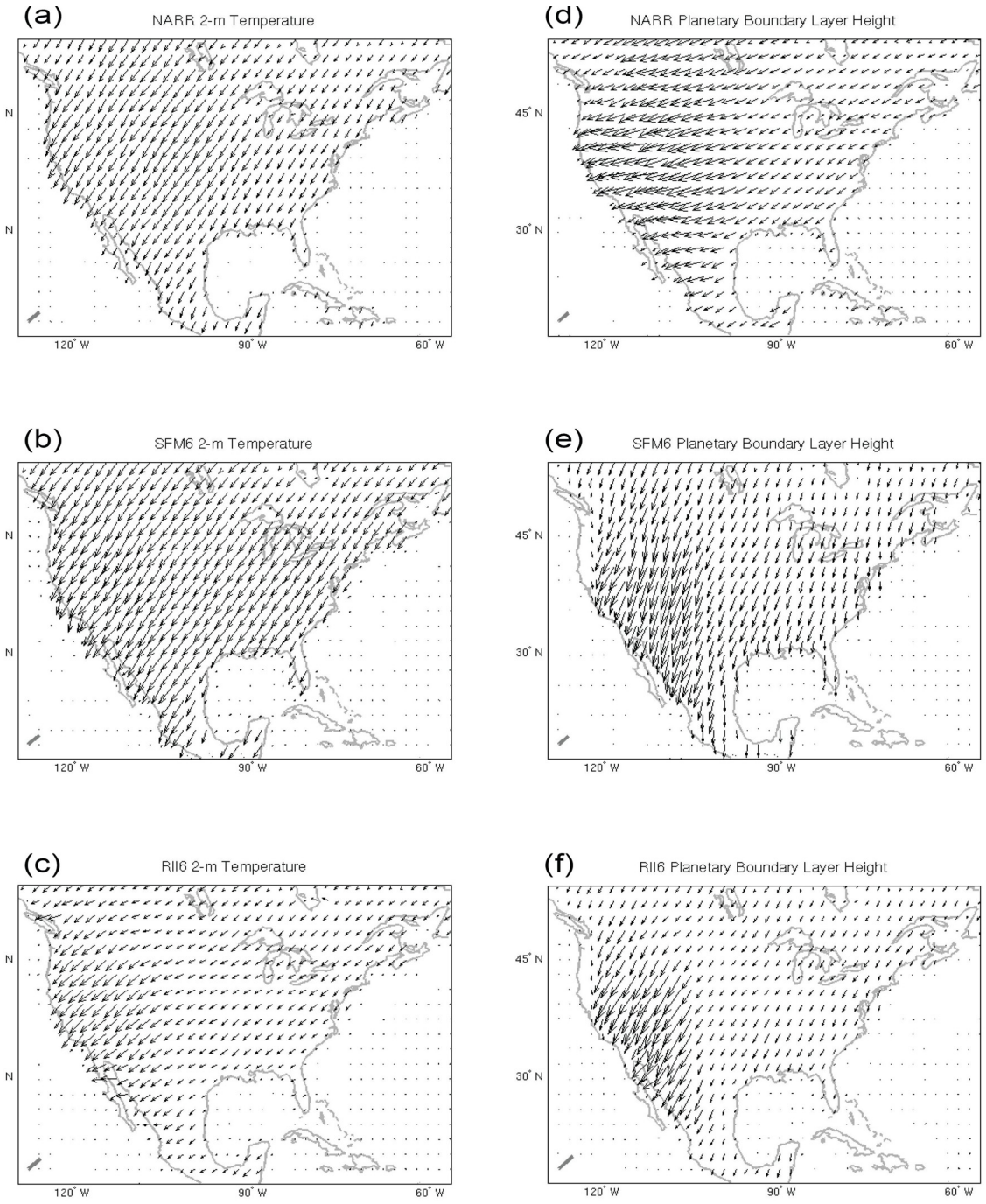

Figure 2.6: As in Fig. 2.5, but for 2-meter temperature (**a**, **b**, and **c**) with a reference length of 5 K, and the planetary boundary layer height (**d**, **e**, and **f**) with a reference length of 1000 m. Note that, for clarity, the unit vector in **b** has been shortened to prevent overlap of larger values, and the unit vector in **f** has been lengthened to make smaller values more visible.

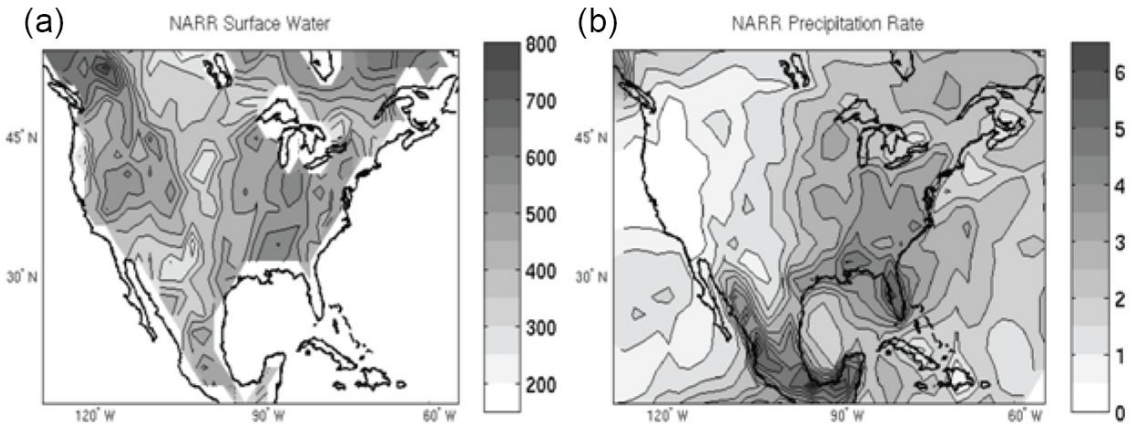

Figure 2.7: NARR July, August, and September 2001-2003 mean (**a**) surface water (soil water + snow pack, mm) and (**b**) precipitation rate (mm/day).

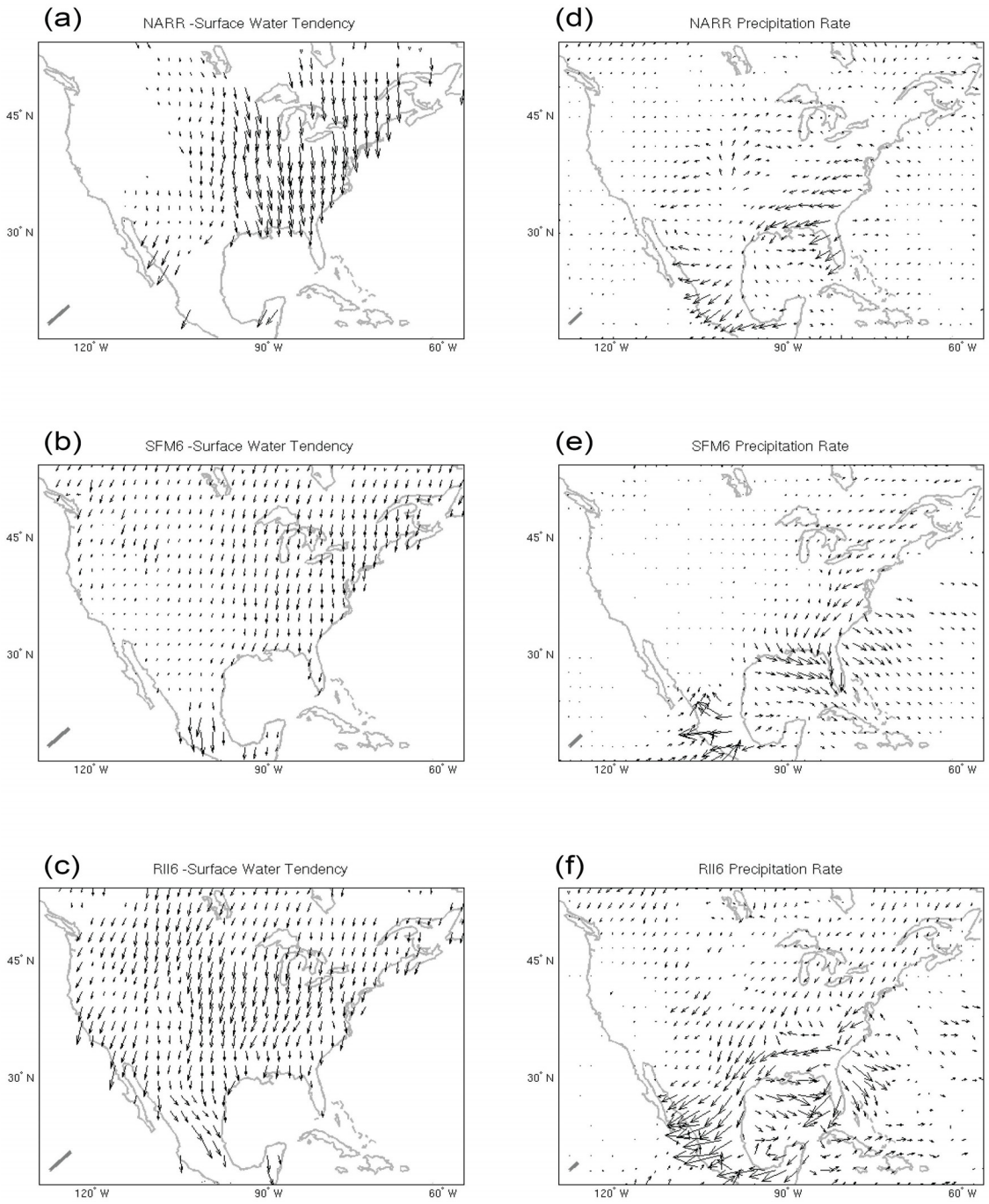

Figure 2.8: As in Fig. 2.5, but for negative surface water tendency (**a**, **b**, and **c**) with a reference length of 10 mm/day and precipitation rate (**d**, **e**, and **f**) with a reference length of 4 mm/day. Note that, for clarity, the unit vector in **f** has been shortened to prevent overlap of larger values.

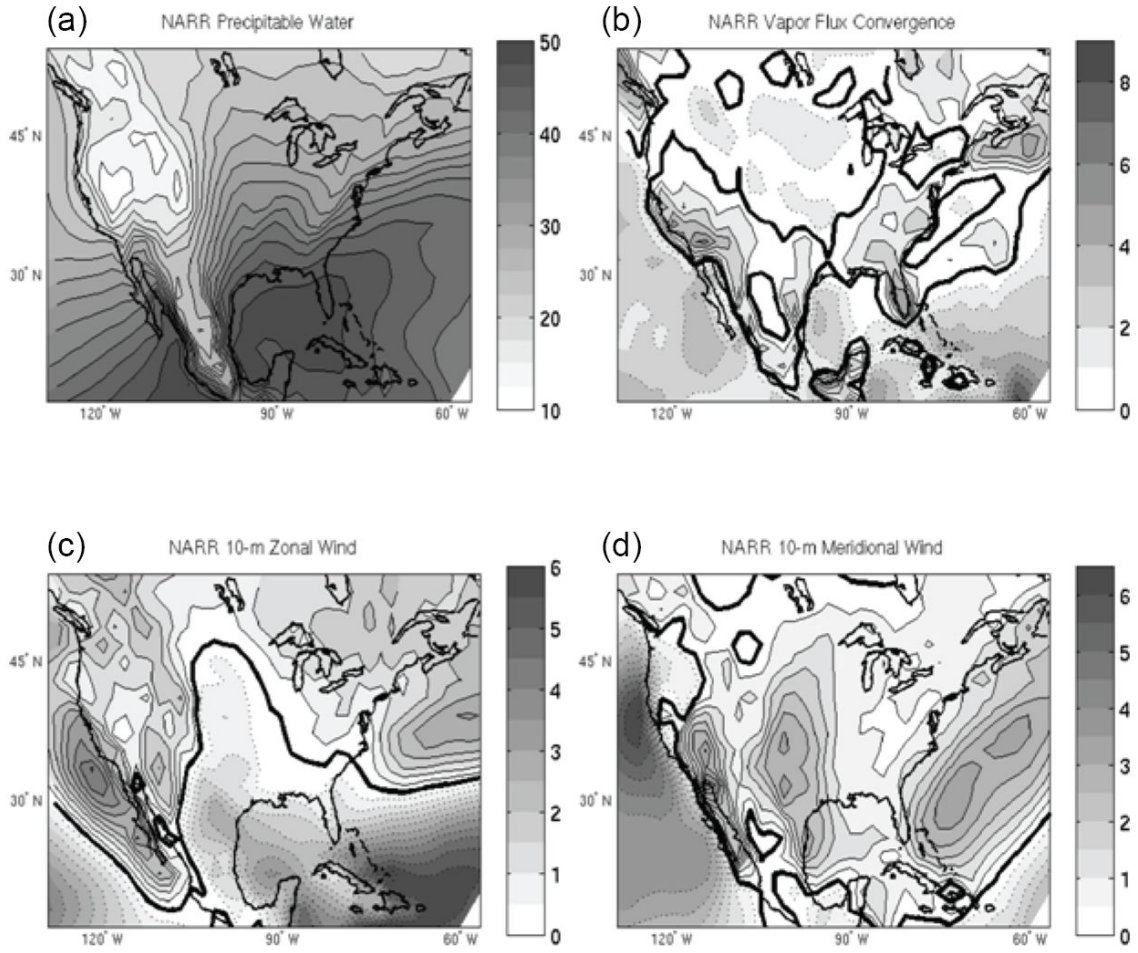

Figure 2.9: NARR July, August, and September 2001-2003 mean (**a**) precipitable water (mm), (**b**) vapor flux convergence (mm/day), and 10-meter (**c**) zonal and (**c**) meridional winds (m/s). Dashed lines indicate negative contours, and the bold line is the zero contour.

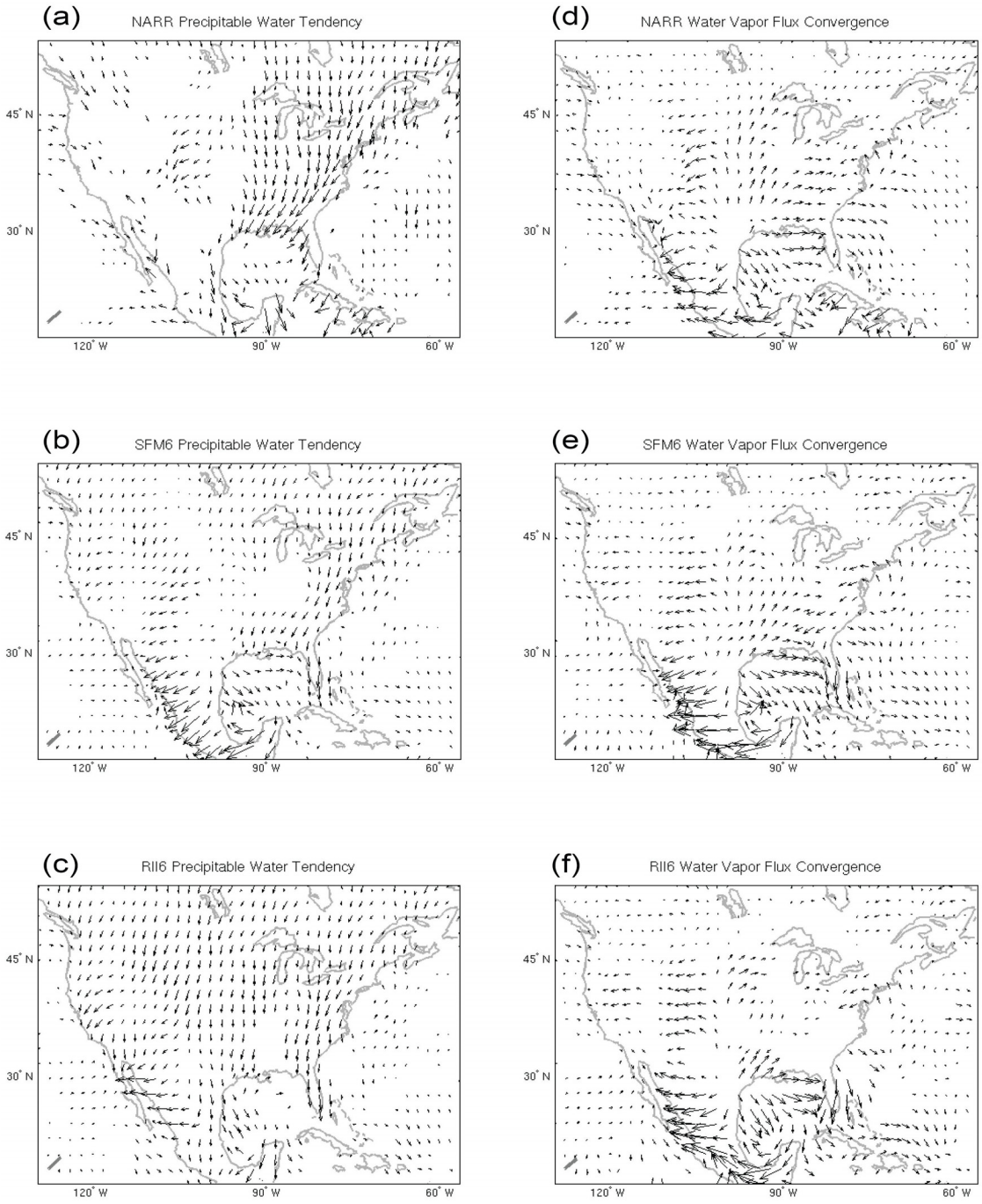

Figure 2.10: As in Fig. 2.5, but for precipitable water tendency (**a**, **b**, and **c**) with a reference length of 10 mm/day, and water vapor flux convergence (**d**, **e**, and **f**) with a reference length of 8 mm/day.

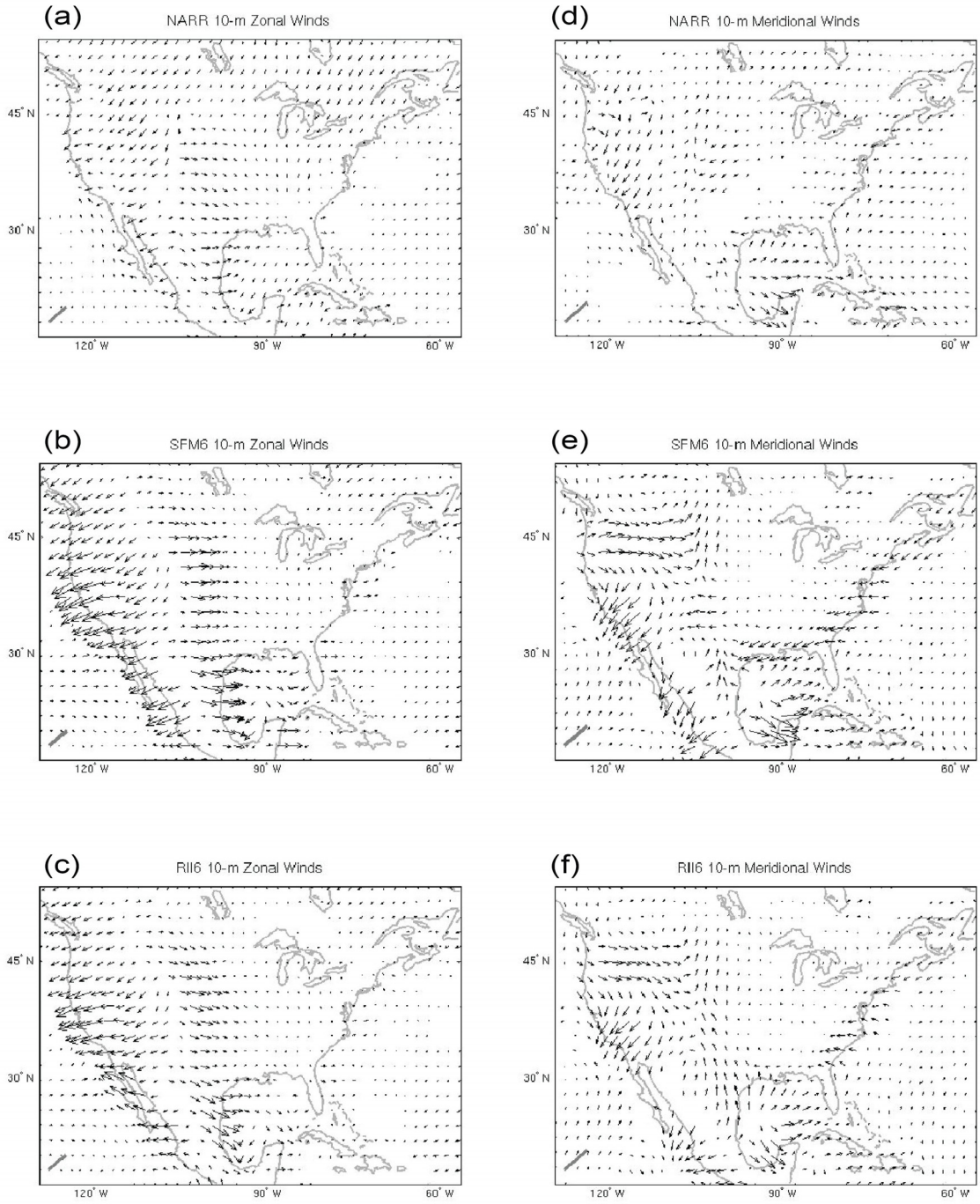

Figure 2.11: As in Fig. 2.5, but for both 10-meter zonal (**a**, **b**, and **c**) and meridional (**d**, **e**, and **f**) winds with reference lengths of 4 m/s. Note that, for clarity, the unit vector for the meridional wind panels has been lengthened to make smaller values more visible.

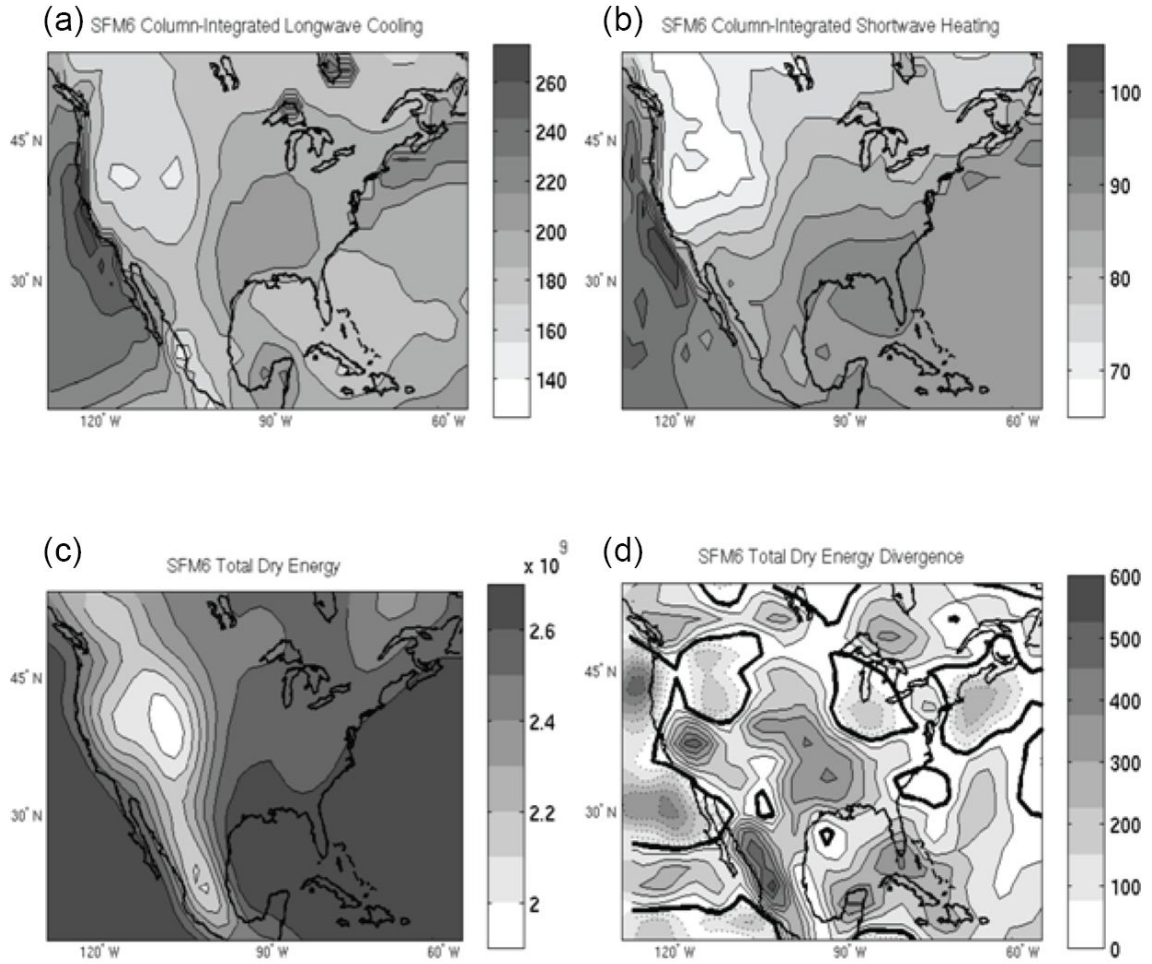

Figure 2.12: SFM6 July, August, and September 2001-2003 mean (**a**) column-integrated longwave cooling and (**b**) shortwave heating (W/m^2), (**c**) total dry energy (J/m2) and (**d**) total dry energy divergence (W/m^2). Dashed lines indicate negative contours, and the bold line is the zero contour.

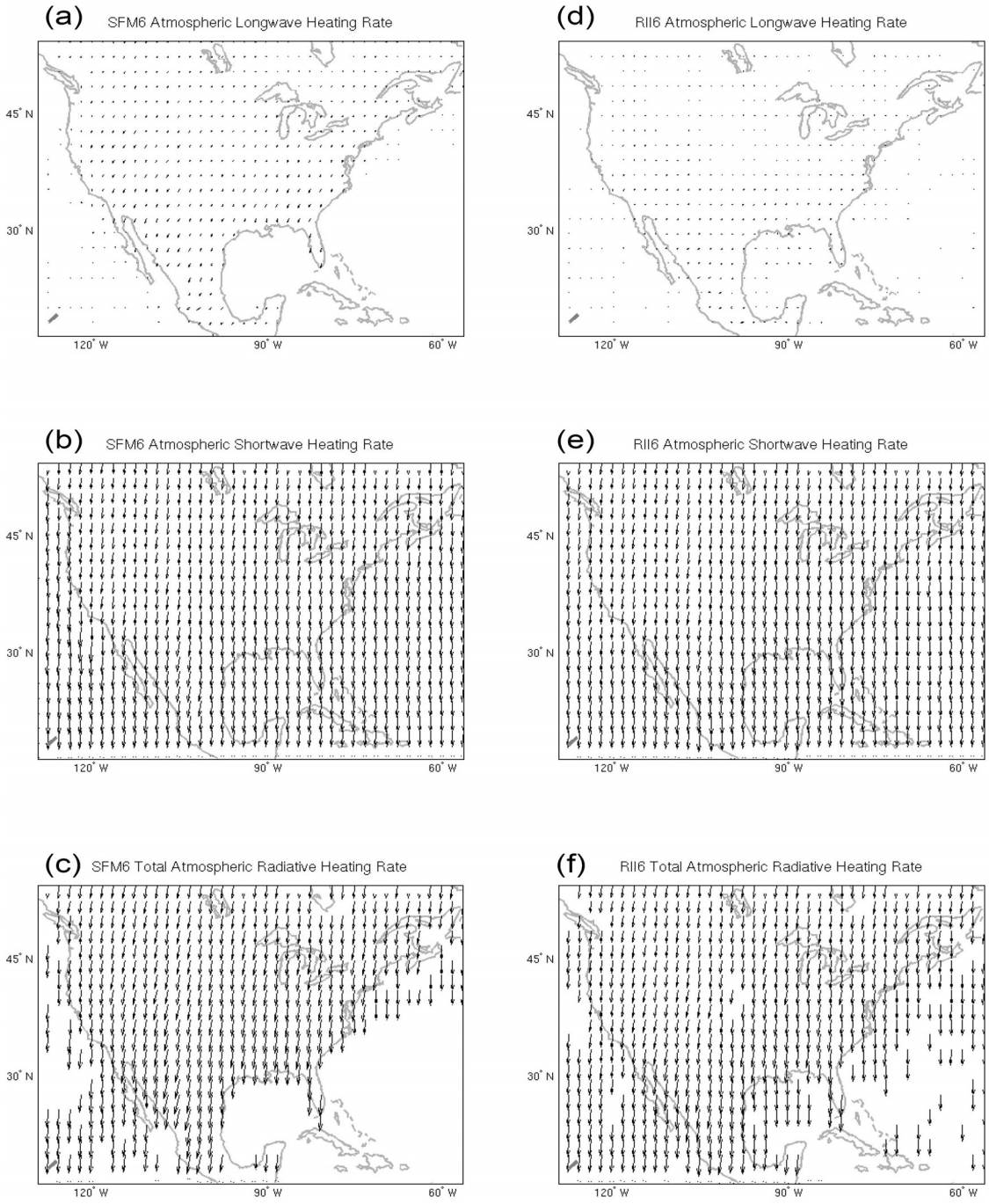

Figure 2.13: As in Fig. 2.5 but for longwave (**a** and **d**), shortwave (**b** and **d**), and total atmospheric radiative heating rate (**c** and **f**), with a reference length of 100 W/m^2. Only the SFM (**a, b,** and **c**) and RII6 (**d, e,** and **f**) reanalyses are available.

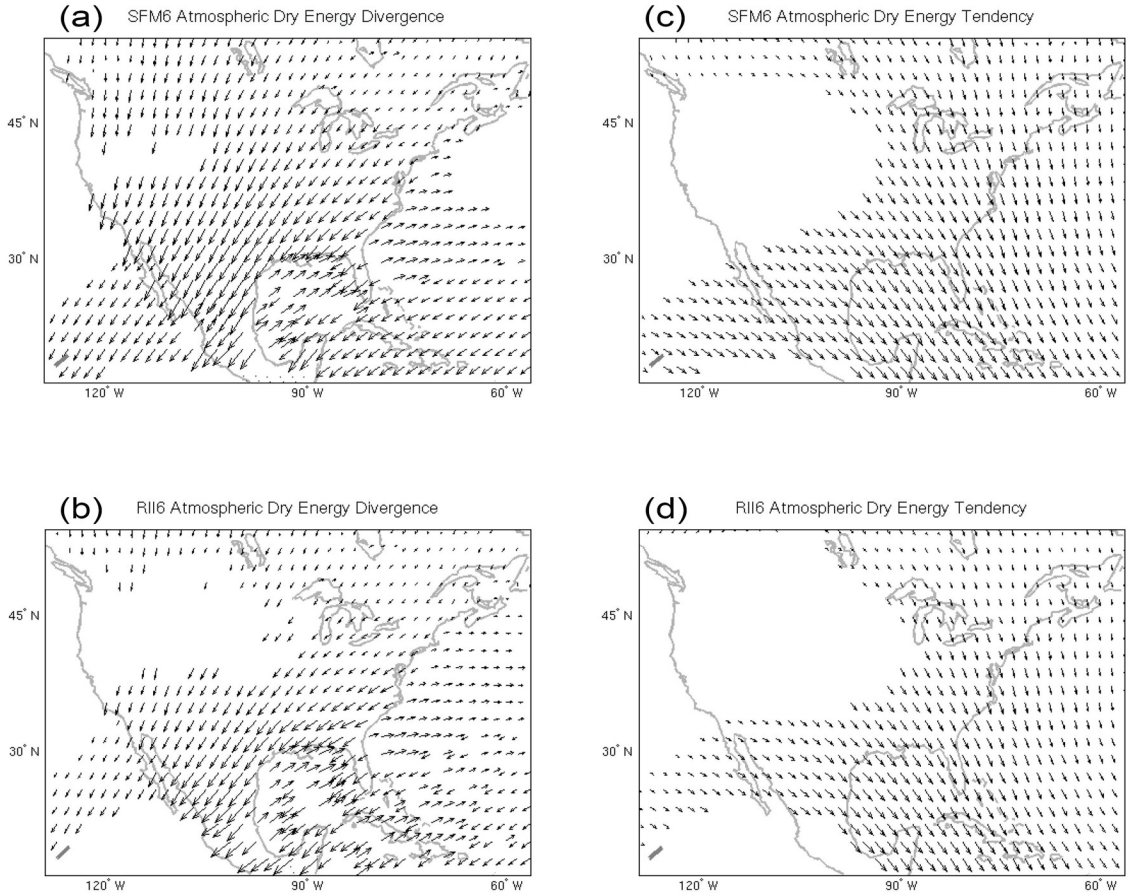

Figure 2.14: As in Fig. 2.5, but for total atmospheric dry energy divergence (**a** and **b**) and total dry energy tendency (**c** and **d**), both with a reference length of 500 W/m^2. Only the SFM (**a** and **c**) and RII (**b** and **d**) reanalyses were available.

CHAPTER III

6-hour to 1-year Variance of Five Global Precipitation Sets

Abstract

Three-hourly time series of precipitation from three high resolution precipitation products (TRMM 3B-42, CMORPH, and PERSIANN) and two reanalyses are examined for their frequency characteristics using broad and narrow variance categories. After isolating the diurnally forced peaks (at 24, 12, 8, and 6 hours), the power spectra are divided into comprehensive broad bands comprising the annual (80 days - 1 year), intraseasonal (20-80 days), slow (6-20 days) and fast (36 hours – 6 days) synoptic, and high-frequency (6-36 hours) periods. Global maps accounting for 100% of precipitation's variance are analyzed to identify unique regional behaviors.

Annual variability is strongest over regions affected by the seasonal migration of the Inter-Tropical Convergence Zone, as well as over monsoonal regions. The intraseasonal band displays off-equatorial evidence of the Madden-Julian Oscillation (MJO), particularly in the Indian Ocean, but the MJO's rainfall is partially manifested in the slow synoptic band and at higher frequencies. The fast synoptic band is particularly strong over the oceans, while high-frequency variability is enhanced over land by more extreme surface gradients. Diurnal variance is strongest at low latitudes and is pronounced over regions with well-known diurnal circulations, including mountains and coastlines. Inter-product and inter-model differences also indicate biases of the precipitation product algorithms and convective parameterizations, including a strong bias toward low-frequency variability in the Relaxed Arakawa-Schubert parameterization

employed by one of the reanalyses, as well as increased white-spectral characteristics over land in the precipitation products.

3.1 Introduction

Precipitation is a very difficult process both to observe and to simulate. Precipitation is generated through complex interactions of dynamical atmospheric convergence, advection, and lifting mechanisms, as well as surface conditions that relate to moisture availability and thermal stability. As each of these processes interacts with the water and energy cycles, they develop unique frequency characteristics. By identifying dominant modes of variability in diverse regions of the globe, one might be able to match key influences that initiate and drive precipitation. In this study, the frequency characteristics of five global precipitation sets (three observational and two atmospheric model reanalyses) are examined for unique regional behaviors as well as biases inherent to each data set.

Many assumptions are taken in the construction of each precipitation set, leading to considerable disagreement that affects each set's frequency characteristics. Continued advancements in computational resources and observations allow for global reanalysis models to be run at higher spatial and temporal resolutions, but observational coverage is still limited and precipitation processes are heavily parameterized. Space-borne global observations capable of resolving both high- and low-frequency variability are only recently becoming available, but algorithm methodologies and missing data still present challenges for High-Resolution Precipitation Products (HRPP). The biases from each HRPP and model parameterization likely have unique frequency characteristics, adding another level of complexity to determining the true behavior of precipitation. Early indications suggest that the satellite-derived products outperform models in more convective regimes (Ebert et al., 2007), although their diurnal variation more closely

resembles surface observations of showery precipitation (Dai et al., 2007). Many additional aspects of the HRPP still need to be inter-compared, although longer time series are necessary before interannual variations may be examined.

Precipitation's dominant behavior is well-known in many portions of the globe, varying by latitude, land/sea cover, local topography, surface temperature and moisture, and large-scale circulations, among other factors. However, disagreements still occur between reanalyses (Newman et al., 2000), and many important geographical areas and portions of the frequency spectrum are neglected (Vincent et al, 1998). Some regions experience shifts in the character of precipitation that are dependent on seasons, often dominated by convective storms in the summertime and synoptic storms in the winter. While it is instructive to examine long time series, future work may examine the dominant frequency behaviors of particular seasons or phases of interannual oscillations.

Many previous studies have examined the diurnal variability of precipitation (Dai, 2001; Dai et al., 1999a,b; Randall et al., 1991; Trenberth et al., 2003; and Ruane and Roads, 2007a, herein referred to as RR2007). The Upper-Midwestern United States is of particular interest due to a unique nocturnal maximum (Wallace, 1975; Carbone et al., 2002), although the amplitude of the diurnal cycle in this region is not notably unusual. Harmonic analysis is often employed to characterize the precipitation in these studies, but significant temporal averaging is necessary to isolate an identifiable harmonic signal, which may or may not be representative of the full time series. For variability that is not so clearly driven by a regular solar forcing, bandpass filters allow the examination of a range of frequencies (Blackmon et al., 1984). Further studies focusing on the Madden-Julian Oscillation (Madden and Julian, 1971, 1972, 1994;

Zhang, 2005) often bandpass filter the data set to examine intraseasonal variability with 30-60 day periods. Additionally, the phase of each mode of variance may be examined to further investigate the role of individual processes with similar periods, although that is not the focus of this study.

This study is a contribution of the Experimental Climate Prediction Center (ECPC) to the Coordinated Enhanced Observing Period (CEOP; Bosilovich and Lawford, 2002; Koike, 2004; Lawford et al., 2006). An element of the World Climate Research Program (WCRP) initiated by the Global Energy and Water Cycle Experiment (GEWEX), CEOP joins together international observational, modeling, and remote-sensing products for a broad inter-comparison. Participants are currently accessing extensive *in situ* observations, customized model variables, and satellite products to characterize, simulate, and predict the Earth's hydroclimate. In particular, a diverse network of 35 *in situ* stations is providing observations at high temporal resolution for comparison to corresponding model output location time series (MOLTS), potentially allowing a broad survey of frequency characteristics during CEOP's comparative period from July 1st, 2001, through December 31st, 2004. The final three years of this time period (2002-2004) is therefore the focus of this work.

Precipitation sets from two reanalysis models and three HRPP are presented in section 3.2. The variance category approaches are discussed in section 3.3, including several example comparisons. Section 3.4 examines the unique aspects of each variance category, as well as the differences between methodologies and precipitation sets, and conclusions are provided in section 3.5.

3.2 Datasets

3.2.1. Reanalysis Models

ECPC contributed two reanalyses of the National Centers for Environmental Prediction (NCEP) Global Spectral Model (GSM) to the CEOP model archive, each with extensive diagnostic variables that allow a detailed examination of the water and energy budgets at all levels of the atmosphere. Augmented 6-hour forecasts were initialized four times each day (at 00, 06, 12, and 18UTC) during the CEOP period for the NCEP/Department of Energy Reanalysis-2 (RII, Kanamitsu et al., 2002b) as well as the Seasonal Forecast Model (SFM, Kanamitsu et al., 2002a) reanalysis. Each forecast time in these models contains the mean precipitation rate during the three preceding hours. For this study, successive 3- and 6-hour forecasts (representing the 0-3 and 3-6 hour forecast periods, respectively) from each augmented run link together to create a comprehensive time series of precipitation. Model spin-up in these early forecast times is non-trivial, and its role in these experiments' atmospheric water cycle is the subject of a manuscript in preparation (Ruane and Roads, 2007c). Preliminary results indicate that the vapor convergence dominates the spin up of the water cycle and acts to moisten the atmospheric column over most extra-tropical land areas.

Each global model uses a primitive equations system of virtual temperature, humidity, surface pressure, and momentum prognostic equations, resolved in the horizontal with spherical harmonics at a triangular truncation of 62 and in the vertical with 28 σ-levels (T62L28). Precipitation is output on a 192x94 gaussian grid, with pixels ~1.9º across. Sea-surface temperatures are represented by a linear interpolation of weekly mean values to daily means. A key difference between the models is that the

RII utilizes the simplified Arakawa-Schubert (SAS, Pan and Wu, 1995) convection scheme, while SFM uses the relaxed Arakawa-Schubert (RAS, Moorthi and Suarez, 1992). RII's land surface is driven by the Oregon State University Land Surface Model (OSU2, Pan and Mahrt, 1987), consisting of two vertical layers in the top 2 meters of soil, while the SFM utilizes the Noah land surface model (Ek et al., 2003) with four layers in the top 2 meters. In addition, both the RII and the SFM adjust the soil moisture as dictated by the biases computed when the model precipitation is compared to observed precipitation over 5-day pentads (see Lu et al., 2005, for a full description). Other notable differences include variations in soil and vegetation classifications, as well as in cloud parameterizations. Finally, it should be noted that the RII forecasts are initialized directly from the NCEP/NCAR Reanalysis-2, whereas the SFM analysis had to be generated beginning in 1998 to allow for soil moisture spin-up (RR2007).

The mean precipitation fields for both the RII and the SFM are presented in panels (a) and (b) of **Fig. 3.1**. Both have the same general pattern, but the RII has higher mean rainfall in many areas, particularly over the continents and much of the Inter-Tropical Convergence Zone (ITCZ), where certain regions' mean precipitation values exceed 20 mm/day. RR2007 demonstrated that although the precipitation characteristics in these reanalyses performed well on seasonal and interannual timescales, they have large errors on the diurnal time scale, suggesting a performance bias in the frequency of precipitation.

3.2.2. High Resolution Precipitation Products

High Resolution Precipitation Products (HRPP) utilize innovative algorithms to dynamically and statistically process observations from geostationary and polar-orbiting satellites to produce gridded precipitation data at high temporal and spatial resolution. These methods have been developed in concert with increasing validation capabilities, including space-borne passive microwave sensors, ground-based observations, and various field experiments. In order to compare the HRPP output to the coarser model output in this study, the HRPP were spatially averaged onto a grid with 1º resolution.

3.2.2.a TRMM

The Tropical Rainfall Measuring Mission (TRMM, Simpson et al., 1988) algorithm 3B-42 precipitation product (see http://trmm.gsfc.nasa.gov/3b42.html and Adler et al., 1994) employs various precipitation assessments to generate rainfall estimations from remotely-sensed observations in a four-part process. High-quality microwave estimates of precipitation from satellites are calibrated and assembled onto a 0.25ºx0.25º grid ranging from 50ºS to 50ºN, centered around 3-hourly intervals (00UTC, 03UTC, etc.). During this study's period of interest, the Climate Prediction Center's Merged infrared (IR) is averaged onto the same grid at the exact 3-hourly intervals, and the monthly histograms of the two sets are used to create calibration coefficients relating the geostationary IR brightness temperatures to precipitation rates (colder brightness temperatures generally indicating higher precipitation rates). After the IR time series has been calibrated each month, an optimal precipitation estimate is made taking the direct high-quality microwave estimates of precipitation whenever available, and filling

in the remaining locations with the calibrated IR estimates. Finally, the merged precipitation set is scaled to match the monthly totals of available gauge observations.

The mean precipitation rate for the TRMM HRPP from the 2002-2004 period is displayed in **Fig. 3.1c**. There is a strong ITCZ and increased precipitation over the cyclogenesis regions, but few regions exceed 12 mm/day. Potential discrepancies in this dataset were introduced through the addition of additional high-quality microwave estimates over time. The use of brightness temperatures to determine precipitation rates also performs best in convective environments, with poorer results in seasons and regions where non-convective rainfall occurs (Arkin and Xie, 1994). Additional errors may be introduced by the microwave channels used by TRMM and as a portion of the other HRPP examined below. The physics of microwave emissions are technically more difficult to observe over land than over the ocean, leading to less certainty over the continents (Ebert et al., 2007). This dataset is extensively used, including as a basis for comparison of 20th century diurnal variations by Dai (2006).

3.2.2.b CMORPH

Geostationary observations are treated differently in the Climate Prediction Center's morphing method (CMORPH, see Joyce et al., 2004, for a thorough overview). Instead of utilizing IR brightness temperature algorithms to estimate unobserved rainfall rates, CMORPH uses IR-derived advection vectors to track precipitating features between satellite overpasses, foreward- and back-interpolating each feature to mimic its propagation and evolution; thereby "morphing" from one microwave observation to the next. Incorporating eight passive microwave instruments along with five

geosynchronous satellites providing IR data, the result is a dataset of estimated precipitation emphasizing feature coherence and free of brightness temperature-based algorithms.

CMORPH data in this study were downloaded at 0.25ºx0.25º spatial and 3-hourly temporal resolutions (ranging from 60ºS to 60ºN), although its native resolution allows for half-hourly values at up to ~8 km resolution (near the equator). CMORPH is only available beginning in December, 2002, and is therefore not available throughout the entire CEOP period of interest for this work. Rather than exclude this HRPP, it is examined here over the three years from 2003-2005. The mean precipitation rate estimated by CMORPH during this period is shown in panel (d) of **Fig. 3.1**. Although it is slightly wetter than TRMM (which may be due to the different temporal coverage), it is still significantly drier than the model simulations over the oceans. Although the different microwave sensors are subject to normalization, potential errors in CMORPH may be introduced when successive microwave observations come from different instruments, causing a "morph" from one set of instrument biases to a different set. In addition, if precipitation forms and dissipates between overpasses, it will not be registered by CMORPH.

3.2.2.c PERSIANN

The automated Precipitation Estimation from Remotely Sensed Information Using Artificial Neural Networks (PERSIANN, see Hsu et al., 1997, for a detailed description) system utilizes far more input parameters in producing rainfall estimates from geosynchronous IR information. In addition to passive microwave sensors, visible

imagery, gauge data, ground-based radar, and surface conditions may be passed into the neural network for each region. The result is an IR analysis algorithm that may be tailored to diverse regional conditions, seasons, and data availability. In addition, each input parameter may be individually analyzed for its impact on the precipitation estimate. The PERSIANN algorithm (Sorooshian et al, 2000) used in this study classifies cloud features from geosynchronous IR imagery and estimates rain rates based on neural network mapping functions that are updated with a TRMM instantaneous rain product (Kummerow et al., 2000) whenever it is available, as well as additional passive microwave imagery from an array of polar orbiting satellites which have been implemented into the current operation (Kuolin Hsu, 2006 personal communication).

PERSIANN estimates are generated at half-hourly resolution, but were downloaded at 3-hourly accumulations from 60ºS to 60ºN at 0.25º resolution for this study, although like the other HRPP they were averaged to 1º resolution. The mean PERSIANN-derived precipitation rate over the period of study appears in panel (e) of **Fig. 3.1**. Sorooshian et al. (2000) pointed out that PERSIANN estimates higher rain rates over portions of the western Pacific Ocean, but in this period precipitation rates are the highest of the three HRPP over most ocean regions as well as the Tropical continents. Rainfall is especially intense over Panama, where it exceeds 20 mm/day. The mean PERSIANN rainfall rates over the ocean lie between the RII and SFM model results. The coverage of geosynchronous satellite causes several significant gaps in the PERSIANN data, so grid points missing more than 20% of their temporal estimates were not included in the Fourier analysis below (for comparison, Sorooshian et al., 2002, omitted points where more than 40% of data was missing).

3.3 Methodology

3.3.1. Spectral Bands

Fourier analysis (Emery and Thomson, 2004) disaggregates a time series into its orthogonal sinusoidal frequency components, allowing variability at individual periodicities to be examined. For simplicity, summing all of the sinusoidal frequency components back together reconstructs the time series for the variable of interest

$$Q(t) = \overline{Q} + \sum_{h=1}^{H} A_h \cos\left(2\pi f_h [(t - \phi_h)]\right), \qquad (3.1)$$

where $\overline{Q}$ is that variable's mean over the record, H is half the number of records in the time series, A_h is the power of the h^{th} frequency band, t is time (in hours), ϕ_h is the phase of the h^{th} frequency band (in hours), and f_h is the frequency of the h^{th} band (in hours^{-1}).

To capture the full frequency characteristics of global precipitation rates, the 3-hourly time series from each model and HRPP grid point was passed through a fast-Fourier transform (FFT) to compute power spectra representing each of 3 years. This procedure requires a continuous time series, so missing data were filled by random values normally distributed about the mean precipitation rate, with variance and standard deviation also equal to the mean rate (negative random values were set to zero). It is also important to note that these time series already average precipitation rate over a 3-hour period and over the geographical region covered by the grid point. Janowiak et al. (2005) also performed Fourier analysis on one year of global-mean 3-hourly CMORPH data, identifying a strong diurnal signal, but the power spectra in this study are noisier because we examine individual pixels rather than the global mean.

To draw out a physical signal, each power spectrum's variance bands were divided into one of six categories in order to get a robust estimate of variance at frequencies that fall under fundamentally different forcing regimes (**Fig. 3.2a**), which are defined below. To cover the diurnal radiative forcing, narrow bands were defined according to the spectral peaks of downward shortwave radiation (**Fig. 3.2b**). With 3-hourly resolution, the mean day contains 8 points that can be described by harmonics covering 1, 2, 3, and 4 cycles per day, resulting in spectral peaks centered upon periods of 24, 12, 8, and 6 hours, respectively. Spectral leakage makes these peaks inexact, but a narrow band only three spectral bands wide and centered on each peak contains >98% of the variance that a 10-wide spectral band would contain for shortwave radiation. By summing these 4 narrow bands, the mean diurnal cycle may be captured. The remaining variance is divided among broad bands that cover forcings that are not so clearly defined by the temporal resolution of the precipitation sets.

First, the *annual* band contains spectral bands that cover the first 4 harmonics of the annual cycle (with cycles repeating 1, 2, 3, and 4 times per year), covering all variability with more than ~80 day periods including seasonality and monsoonal circulations. As it is not likely that any rainfall event would persist over time scales this long, the annual band represents low-frequency cycles that affect broader conditions that favor or hinder precipitation. As substantial low-frequency drivers of precipitation often manifest themselves through higher-frequency systems, their percentage variability described in these bands can still be quite low (Dunkerton and Crum, 1995).

Second, the *intraseasonal* band covers all variability with periods between 20 and 80 days. This band includes the Madden-Julian Oscillation (MJO) from both infrared

observations (generally between 30-60 days; Knutson and Weickmann, 1987) and model simulations (which tend to be too weak and in the faster portion of the range; Lin et al., 2006; Slingo et al., 1996). Like the annual band, the intraseasonal band does not indicate storms lasting for weeks and months, but long-period shifts in how conducive an environment is to rainfall.

Third, the *slow synoptic* band contains the variance associated with periods between 6 and 20 days. As noted by Vincent et al. (1998), this band contains easterly waves, monsoon depressions, typhoons, Rossby wave trains, and circulations involved in tropical-extratropical interactions, many of which are manifestations of annual and intraseasonal conditions.

Fourth, the *fast synoptic* band holds the variance associated with periods between 36 hours and 6 days. This band includes many known processes with a range of forcing periodicities, including westward propagating Rossby-gravity waves, extratropical baroclinic modes, and Kelvin waves. Examining 14 coupled models from the Intergovernmental Panel on Climate Change's Fourth Assessment Report, Lin et al. (2006) found that variance between 2-128 days was too weak.

Finally, the *high-frequency* band captures the variance whose period falls between 6 and 36 hours, with the exception of the narrow bands that make up the diurnal cycle. Mesoscale systems and quick enhancements and deintensifications of precipitation lie in this band, along with diurnally forced variations whose phase is different from the mean phase. In addition, reanalysis data assimilation and spin-up noise are contained in the high-frequency band.

It is necessary to remember, however, that forcings on one time scale may affect precipitation on another. For example, upper-level MJO disturbances are often led by higher-frequency transients (Matthews and Kiladis, 1999; Lau et al., 1989; Haertel and Kiladis, 2004) and contain synoptic systems inside the "envelope" of MJO activity (Vincent et al., 1998). Zhao and Weare (1994) suggested that increased diurnal variation could reduce low-frequency variability over the tropical continents, while Sui and Lau (1992) found that the MJO diminished diurnal variability over the maritime continent during its active phase. Also, "active" and "break" regimes of monsoonal circulations lead to variability with a period of ~5 days (Jones and Carvalho, 2002).

The percentage variances described by each category are averaged over all annual realizations, resulting in 3-year mean percentage variances for each grid point. Together, the six variance categories (annual, intraseasonal, slow synoptic, fast synoptic, high-frequency, and diurnal) account for the entire variability of the precipitation set between 6 hours and 1 year, however the variance categories do not all have the same spectral widths. 82.5% of the variance bands fall in the high-frequency, 12.5% in the fast synoptic, 3% in the slow synoptic, 1% in the intraseasonal, 0.25% in the annual, and 0.75% in the diurnal variance category. Therefore, it is important to examine the variance categories remembering that a white-noise spectrum (with no real signal) would produce percentages of variance that are equal to the percentages of total variance bands in each category. Values which are much higher than the theoretical white-noise spectral values indicate a strong signal regardless of their magnitude in comparison to other variance categories. For example, a grid point that contains 5% of its variance in the annual category is displaying 20x more annual variance than a comparable white

spectrum would. In contrast, a grid point which demonstrates much less variance in a particular category than the theoretical white-noise spectrum indicates a preference for other variance categories in the complete series. The annual variance category contains the least degrees of freedom in each grid point (4 variance bands over 3 years = 12), but for higher statistical significance it is important to examine the general behavior of multiple grid points rather than any single point in isolation. HRPP have 16x the degrees of freedom as the reanalysis models, owing to the sixteen ¼ º grid boxes that are averaged into a single 1º box.

To ensure that each grid point was independent from a white noise spectrum, several statistical tests were performed. First, if the absolute difference between a particular grid point's three-year average value and the white noise spectral value in each variance band was less than twice the range of values between the three annual spectra in each band, that grid point was omitted on the basis of too much inter-annual variability to distinguish itself sufficiently from the white noise spectrum. Second, if the absolute difference between the three-year average grid point value and the white noise spectral value in each variance band was less than twice the standard deviation of all the grid points' values in each variance category, then the grid point was omitted for failing to distinguish itself from the white noise spectrum in any variance category map. Finally, as mentioned above, if a grid point was missing more than 20% of its values, it was omitted for incompleteness. As a result of these tests, many grid points are omitted over areas not covered by the satellites and regions with very little rainfall (such as the deserts and stratocumulus regions). In these regions, events were too sporadic to provide significant deviations from the white noise spectrum.

Additional methodology caveats are also worth pointing out. The relatively short time period covered by these precipitation sets leads to potential artifacts in the lower-frequency bands. For example, the intraseasonal band has 60 day cycles that only repeat ~18 times over three years, while the high-frequency band's 36-hour cycle has 730 realizations over three years. Therefore, it is more useful to examine the lower-frequency bands for general larger-scale behaviors rather than comparing neighboring pixels' values. Additional tests (not shown) using varying broadband definitions and segments of the time series displayed similar results to those shown here. Finally, decreased horizontal resolution (for example between the reanalyses and the HRPP) leads to a decrease in high-frequency variance, as larger spatial averaging diminishes the power of high temporal and spatial resolution events.

3.3.2. Example Applications

To demonstrate the methodology in this study, additional variables with known forcing were analyzed. **Figure 3.3** shows the square-root of the mean SFM annual power spectra from 2002-2004 for surface downward shortwave radiation flux, precipitation rate, 500-hPa geopotential height, precipitable water, and the moisture content of the top 10 cm of soils at the grid point corresponding to one of the CEOP reference locations, the Atmospheric Radiation Program's Southern Great Plains site (ARM SGP). Strong diurnal peaks are evident in the radiation flux, and appear to a much smaller extent in the 500-hPa geopotential (due to diurnal heating) as well as the precipitable water and soil moisture (due to evaporation). Aside from the annual peak, it would be very difficult to capture the rest of the variance in narrow bands, as

variability is spread across many high-frequency, synoptic, and intraseasonal bands; particularly in the precipitation spectrum. As either the diurnal or annual peak is very strong in all locations, none of these points could be confused with the white-noise spectrum.

To demonstrate regional variations, **Fig. 3.4** shows the square-roots of the same variables' spectra at ARM's Darwin, Australia, site (another CEOP reference location). At this tropical location, the diurnal cycle is enhanced in most variables, with only the drier soils showing a decrease in diurnal variance when compared to the ARM SGP location. The 500-hPa geopotential height also displays a pronounced semidiurnal thermal tide (Lindzen, 1967). Further analyses on these (and other water and energy component) spectra are under way.

Figure 3.5 shows the percentage of surface downward shortwave radiation flux variance described by the annual, intraseasonal, slow synoptic, fast synoptic, and high-frequency wide bands, as well as the sum of the narrow diurnal bands at each SFM grid point averaged over annual spectra from 2002-2004. As expected, the diurnal cycle dominates most of the globe, but high-latitudes are dominated by the annual band that contains the seasonal forcing. The high percentage of variance described by the narrow diurnal peaks suggests that this variable may be adequately represented by select harmonics over most of the globe. Annual variability is weakened outside of the Arctic and Antarctic Circles, where the diurnal variation is significantly higher than the variation of the mean. The remaining variance is mostly spread between the synoptic and high-frequency bands, capturing cloud cover variability across many frequencies in the northern storm tracks and the Southern Ocean.

3.4 General Frequency Behaviors

The percentage variances of all variance categories for each of the HRPP (TRMM 3B-42, CMORPH, and PERSIANN) are shown in **Figs. 3.6-8**, and for each of the reanalyses (the RII and the SFM) in **Figs. 3.9-10**. Note that the color bars differ between panels to demonstrate unique regional behavior in each band, and that the theoretical white-noise spectral value for each band is included for comparison. Differences between these figures stem from a series of potential distinctions. First, each variance category has unique physical forcings that are emphasized in different regions of the globe. Second, there are differences between each HRPP, including the coverage and availability of data. Third, inter-comparison of the reanalyses requires recognition of the effects of their unique parameterizations and tuning. And, finally, comparisons between the reanalyses and the HRPP indicate areas of simulation that could be improved.

3.4.1. Band Comparison

The high-frequency band contains the highest proportion of variance in every precipitation set but the SFM (the unique aspects of the SFM results are discussed below) both over land and over the sea, but shows enhanced variance over land points. The stark land/sea contrast is due to a combination of several mechanisms. First, the land's lower heat capacity and reduced evaporative potential allow for faster variations in atmospheric stability and convective available potential energy, leading to more mesoscale variability. Second, sharp horizontal gradients in topography and land cover lead to more rapid intensifications and moderation of existing lower-frequency storms as

they pass over land. Finally, seasonal shifts in daylight and surface conditions lead to inconsistent diurnal behaviors over the course of the year, leading to increased high-frequency variance to account for the discrepancies. One interesting regional feature is the Southern Ocean, where precipitation is apparently dominated by fast-moving storms and high-frequency enhancements leading to irregular variability.

Despite the large percentages of variance described by the high-frequency band, in almost every location the values are well below the theoretical white-noise spectrum. This suggests that these precipitation sets are best represented by a reddened spectrum, and generally deemphasize the high-frequency variability. Regions with rare and sporadic precipitation are not distinguishable from the white-noise spectrum (as mentioned above), but the regions with a significant signal follow this redder spectrum. Similar red spectra have been identified in many atmospheric variables (Hendon and Woodberry, 1993; Torrence and Compo, 1998).

The diurnal category captures surprisingly little variance from the full annual series, but several times the white-noise values along coastlines, mountain ranges, and in many tropical regions. Consistent diurnal precipitation comes from mountain-valley and land/sea circulations that are thermodynamically forced by the diurnal solar forcing, but the increased seasonality of the higher latitudes reduces the power of a consistent diurnal cycle (as discussed above). Mountainous tropical coastlines (like New Guinea, Indonesia, Central America, and Madagascar) have the most consistent diurnal cycles. Interestingly, the eastern slope of the Rocky Mountains shows enhanced diurnal variability in many of the precipitation sets.

The fast synoptic variance category contains most of the remaining variability over land areas, but is notably strongest over the oceans, where it regularly captures more than twice the white-noise theoretical value. Synoptic systems do not encounter the same sharp gradients in atmospheric conditions over the ocean, and therefore are able to maintain their structure. Regional enhancements over the ocean in this frequency range appear in the northern hemisphere storm tracks, as well as in East Pacific portions of the ITCZ (as noted by Rasmusson and Arkin, 1993). Precipitation over the glacial surface of Antarctica and Greenland appears to be mostly a fast synoptic process in both reanalysis models.

The intraseasonal and slow synoptic bands appear to share many similarities, suggesting that the MJO disturbances that dominate the intraseasonal band set an environment conducive to slow synoptic precipitation features. Both bands show their highest percentage variances over the Tropical Indian Ocean and West Pacific Warm Pool, where sea surface temperatures (SSTs) are warm enough to maintain the MJO. The MJO's precipitation signal is not exclusive to the intraseasonal band, demonstrating common regional behaviors in the slow synoptic band. The long-period variability is also obscured by slow synoptic, fast synoptic, and high-frequency variance as shown by Vincent et al. (1998). In the subtropics, where descending portions of the Hadley circulation lead to large-scale convective inhibition, slow synoptic systems that are organized enough to penetrate what is otherwise a stable region contain a larger percentage of variance. In these latitudes, so-called "tropospheric rivers" (Newell et al., 1992) that provide low-level tropical moisture to the subtropics on similar time scales appear to make a significant contribution to rainfall. Off-equatorial enhancement of the

intraseasonal oscillation was also observed by Matthews and Kiladis (1999) and in the slow synoptic band by Vincent et al. (1998). Similar penetration by slow synoptic disturbances accounts for significant variance over the Sahara and Arabian deserts in some precipitation sets.

The behavior of the intraseasonal variability in the Pacific Ocean is particularly compelling, extending much further poleward in the eastern portions of the basin than in the western. This suggests a poleward propagation of the MJO signal as it moves across the Pacific, possibly through the excitation of upper tropospheric wave trains (as suggested by Vincent et al., 1998 and Lin et al., 2006), although the equatorward return in the Atlantic is not clear. Bandpass-filtered analysis would allow the propagation characteristics of these variance patterns to be tied to specific forcing mechanisms.

The annual band also shows clear evidence of the ITCZ's seasonal migration, although it is diminished over the Indian Ocean and Western Warm Pool, where the MJO seems to dominate the low-frequency variability. Increased annual variance in the equatorial East Pacific seems to correspond to the seasonal appearance of the southern portion of a double ITCZ in the Boreal springtime. Monsoonal circulations in India, Southeast Asia, Australia, North America, and South America are also evident. Although precipitation driven by such low-frequency oscillations is manifested mostly at higher frequencies, the variance described by the annual category is often greater than 10x the theoretical white noise value, validating a strong annual component to many regions' precipitation record.

3.4.2. HRPP Inter-comparison

In addition to the percentages of variance described at each point over the entire HRPP and model domains (Figs. 3.6-10), the zonal mean percentages of variance for land and sea from each category are shown for each precipitation set in **Fig. 3.11**. Examining first the HRPP (Figs. 3.6-8 and Fig. 3.11, *panels a-c*) it is apparent that while CMORPH and PERSIANN estimate overall patterns that are remarkably similar, TRMM estimates are much closer to the white-noise spectral values. In addition, TRMM shows little latitudinal variation in the percentage of zonal mean variance in comparison to the other HRPP. The statistical test that ensures each grid point distinguishes itself from the white-noise spectrum on each variance map is failed by most continental points in the TRMM precipitation set, most likely due in part to errors introduced by microwave channels over land (Hendon and Woodberry, 1993, noted a similar whitening of land spectra in their IR-based observations of precipitation). To show more of the regional variation over land points, grid points were eliminated if they were never more than one standard deviation away from the white-noise value, as opposed to a two standard deviation test applied to all other sets (all other statistical examinations have identical criteria). While the variance maps for the TRMM set still have the most grid points omitted for statistical reasons, the general pattern of omissions using the less stringent geographical test is consistent with the other sets.

PERSIANN, on the other hand, displays the greatest regional contrasts in variance, as well as the highest percentage variances in the low-frequency categories. PERSIANN contains the largest zonal mean differences, with a particularly strong oceanic interchange between the high-frequency and synoptic bands at the ascending and

descending regions of the Hadley circulation. Slow and fast synoptic variabilities also make slightly larger contributions over the mid-latitude continents than in the TRMM and CMORPH results, indicating the persistent tracking of storms with longer lifetimes in these regions. PERSIANN produces the highest percentage of variance in the narrow diurnal bands (especially in the Tropics), and is notable for having the largest land/sea contrasts in the high-frequency and synoptic categories (particularly in the Northern Hemisphere).

CMORPH is missing a significant number of values over snow-covered regions in 2003. The replacement of these missing values with randomly distributed data generates a spectrum that is biased toward the white spectrum. This makes the high annual variance over these snowy regions even more impressive, as the years that are not missing many values show even stronger annual variance than the three-year mean indicates. CMORPH is unique among the HRPP for having such strong annual variance at high latitudes, although PERSIANN shows slightly enhanced Siberian variance. Surprisingly, the annual band in both CMORPH and PERSIANN show a Pacific connection between the tropics and extratropics that suggest a seasonal excitation of the same upper tropospheric wave trains that appear in the intraseasonal band. These are also the only two HRPP which show slow synoptic systems that penetrate the Sahara and Arabian deserts.

3.4.3. Reanalysis Model Inter-comparison

The difficulties in simulating the complex mean states and variability of precipitation in reanalyses was put nicely by Newman et al. (2000), who noted that

reanalyses may have internally consistent datasets, but that external consistency between separate reanalysis datasets was "so low as to defy a simple summary". Despite very similar core model structures, the RII and SFM precipitation sets display very different temporal frequency characteristics. Although they are very similar at high latitudes, elsewhere SFM features a dramatic shift in variance toward lower frequencies in comparison to RII (see Fig. 3.11, *panels d-e)*. From ~60ºS - ~70ºN, RII is dominated by high-frequency variance (although it is still well below the white-noise expected value), with the annual and intraseasonal bands each representing less than 10% of the variance and the fast synoptic band matching latitudinal variations in the high frequencies. In the mid-latitudes, SFM's high-frequency and fast synoptic bands split ~75% of the variance, while in the Tropics the lower-frequency bands become more prominent. These unique SFM frequency characteristics also correspond to reduced mean Tropical precipitation in comparison to the RII. The SFM's fast synoptic band lacks a substantial land/sea contrast, and is the dominant frequency band for precipitation in many locations.

The most likely culprits for this major shift in precipitation frequencies in the Tropics are the convective parameterizations. Kanamitsu et al. (2002a) noted that the SFM's RAS scheme significantly improves the Pacific-North American pattern of interannual variability, but the improved low-frequency characteristics appear to hinder the high-frequency performance of the parameterization. A major difference between RAS and SAS is the treatment of downdrafts, which are not considered in the RAS scheme. The omission of this feature in RAS appears to weaken the short-lived power of convective storms, which are especially prevalent in the Tropics. Similarly, Slingo et

al. (1996) and Lin et al. (2006) noted that the closure mechanisms used in a convective parameterization can significantly influence the signal of the MJO.

Analysis of the narrow diurnal bands also indicates that the RII produces more consistent daily precipitation around mountainous regions at all latitudes as well as tropical coastlines, while the SFM's diurnal variance seems to be tied only to tropical landmasses. Whether this is due solely to the convective parameterization or to a combination of other factors is the subject of ongoing work. Additional synoptic power in the SFM could also come from the increased soil moisture resolution used in the NOAH land-surface model. With 3 soil layers in the top meter alone, the NOAH soil moisture contains a more precise memory, allowing for increased synoptic variability.

3.4.4. HRPP and Model Comparison

Despite some obvious discrepancies, many aspects of the HRPP's frequency behaviors are captured by the reanalyses. Monsoons and a migrating ITCZ show up in all precipitation sets, as does an MJO that manifests itself partially in the slow-synoptic band (Lin et al.. 2006, found that most global coupled models produce an MJO signal that is too weak, but these reanalyses actually produce stronger intraseasonal variance than is seen in the HRPP). The use of reanalysis experiments are not necessarily indicative of a longer free simulation, as Reichler and Roads (2005) showed that the effect of initial conditions are only noticeable out to ~40 days. High-frequency variability is a major portion of the variance in all time series, although errors introduced by the use of microwave channels lead to a whiter spectrum over land in the HRPP and larger high-frequency variance.

Diurnal variability in all precipitation sets is concentrated in the tropics. The RII distinguishes itself from the SFM in that it also captures the diurnal influence of mountains, land/sea contrasts in all variance categories, and restrained low-frequency enhancements; features that are all common in the HRPP. PERSIANN, CMORPH, and the RII also all show ocean precipitation to be nearly evenly split between the high-frequency variance category and the rest of the spectrum. Both reanalyses have much larger latitudinal variations than are seen in the HRPP (although the RII shares many of the meridional structures), and only the RII captures the wave train excitation in the intraseasonal band.

The apparent overestimate of synoptic and low-frequency variability in the reanalysis models corresponds to a well-known problem in numerical weather prediction models, where convection is triggered prematurely, precipitation falls too frequently with intensities that are too light (Trenberth et al., 2003). The enhanced diurnal variability over northern continents in the RII are likely due to a preference for diurnally forced convective activity even in regions where it is not seen in the HRPP. The actions of the Arakawa-Schubert convection parameterizations used in this study are too strongly dependent on non-local driving mechanisms on longer temporal scales, leading to reduced high-frequency amplifications but longer periods of light precipitation. As sea-surface temperatures in both models are interpolated from weekly mean values, the tendency toward synoptic variability is increased.

RII and SFM coastlines do not appear to be as stark as the HRPP coastlines, owing to coarser horizontal resolution and the reanalysis models' inability to resolve mesoscale coastal circulations and contrasts properly. The percentage of diurnal

variance is enhanced along the coastlines in the RII model, but the coarse topographic resolution appears to drive overly consistent diurnal variation over the mountains.

3.5 Summary and Conclusions

Three-hourly precipitation time series from three observational HRPP (TRMM 3B-42, CMORPH, and PERSIANN) and two reanalysis models (RII and SFM) were analyzed for their frequency characteristics over a three year portion of the CEOP time period (with the exception of CMORPH, which used a more recent 3-year period). By dividing each series' power spectrum first into narrow diurnal bands defined by the solar radiation's spectrum, and then into broad annual (periods from 80 days - 1 year), intraseasonal (periods from 20-80 days), slow (periods from 6-20 days) and fast (periods from 36 hours – 6 days) synoptic, and finally high-frequency (periods from 6-36 hours) variance bands, major frequency behaviors in global precipitation patterns were identified.

The individual variance categories demonstrated signatures of unique dynamic and thermodynamic regimes, including monsoons, the ITCZ, the Hadley circulation, stratocumulus banks, land/sea contrasts, and arid regions. Precipitation generally has a red spectrum. High-frequency variability is the strongest component, and demonstrates a strong enhancement over land, particularly in the HRPP where data issues are a factor. Fast synoptic variability is increased over the sea, where dynamical and thermodynamical gradients in the surface boundary are not as sharp as over the land. Slow synoptic variability is stirred up by intraseasonal MJO disturbances over the tropical oceans, but makes up an increased proportion of the variance in the downwelling regions of the

Hadley circulation where convective storms are inhibited by large-scale subsidence. Annual variability captures monsoonal circulations as well as the seasonal migration of the ITCZ outside of the MJO-dominated regions.

The precipitation sets still demonstrate considerable disagreement. While CMORPH and PERSIANN appear to capture a wider array of frequency behaviors, TRMM is dominated by the high-frequency variability and a tendency to approach a white-noise spectrum over land, while PERSIANN shows the highest contrast between different regions. The convective parameterization in the SFM produces a large increase in low-frequency tropical variance at the expense of the high-frequency variance, making it the outlier among the five precipitation sets. The relaxed Arakawa-Schubert scheme was selected for its increased interannual skill, but appears to sacrifice its high-frequency characteristics. Also, the SFM contains higher fast synoptic variability over the continents, likely due in part to the longer soil moisture memory in the Noah land-surface scheme. Both reanalyses show signs of an overactive convective triggering mechanism.

There remains significant room to improve the frequency characteristics of precipitation in reanalysis models, as well as the accuracy of precipitation observation methodologies. As more CEOP reference sites report their precipitation data, they will provide an exceptional basis on which to compare various precipitation sets. Characterizing the variability of precipitation in the current climate is vital to understanding how the nature of precipitation across the globe may react to a changing climate. Broad band frequency analysis may be applied to characterize discrepancies between the parameterized treatments of additional reanalysis variables, which is the

subject of future work. In addition, broad band analysis more completely describes exchanges between different components of the water cycle (Ruane and Roads, 2007c). For variables with clearer power spectra, narrower bands may be utilized to further isolate particular forcings.

3.6 Acknowledgements

The text of this chapter, in full, is in press at *Earth Interactions* by A.C. Ruane and J.O. Roads. The dissertation author was the primary investigator and author of this paper. The coauthor listed in this publication was fundamental to the research which forms the basis of this chapter. We gratefully acknowledge the support received through NOAA NA17RJ1231 and NASA NNG05GR40G and NNG06GC85G grants. The views expressed herein are those of the authors and do not necessarily reflect the views of NOAA and NASA. The authors would like to thank Masao Kanamitsu for his updates to the SFM and frequent advice. We would also like to thank Jack Woollen and Wesley Ebisuzaki for help with the SFM reanalysis, the data management teams for the PERSIANN, CMORPH, and TRMM 3B-42 products, Martin Olivera and Jack Ritchie for providing technical support, and two reviewers for their helpful comments.

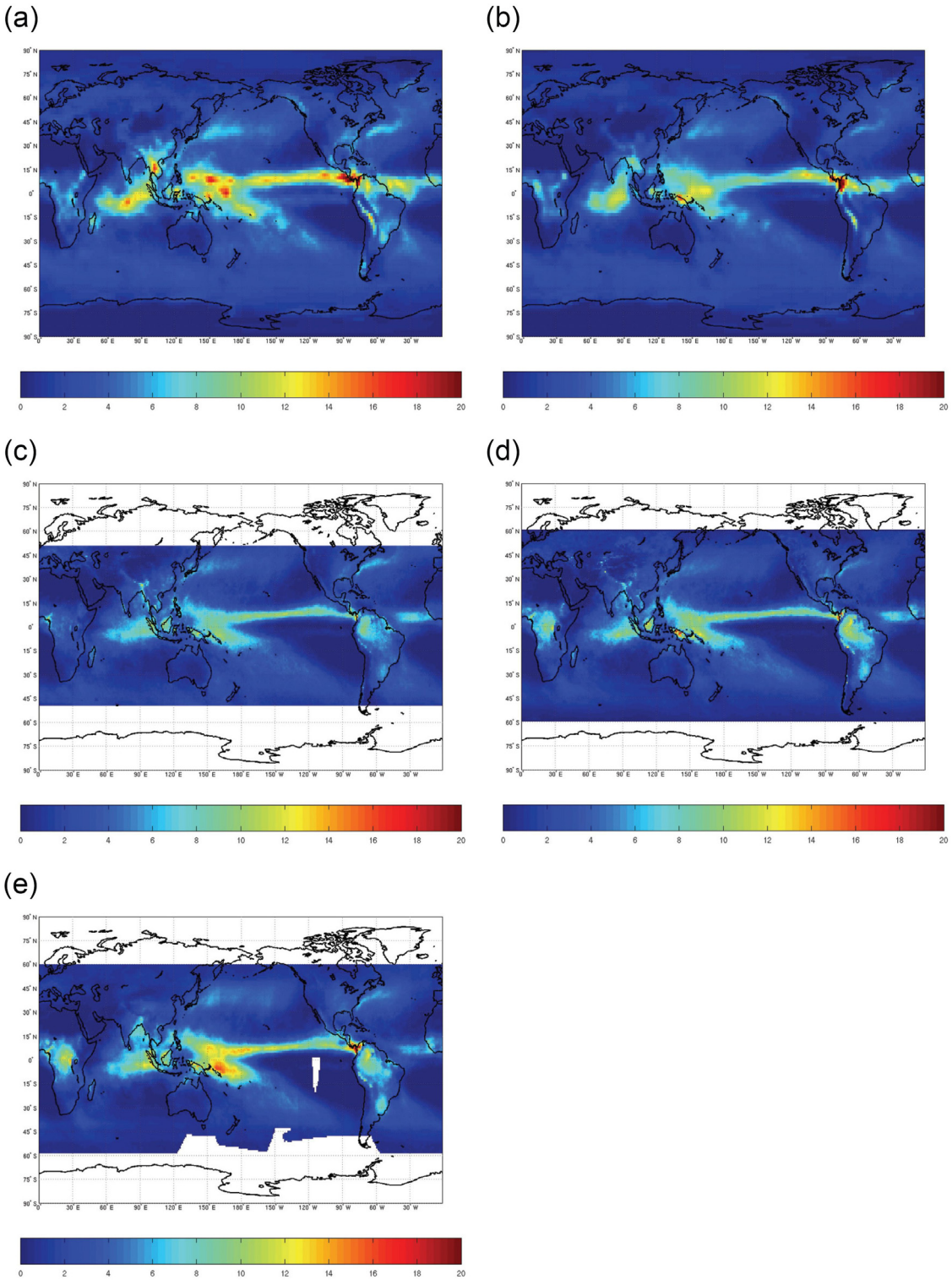

Figure 3.1: Mean precipitation (mm/day) from *(a)* RII, *(b)* SFM, *(c)* TRMM, *(d)* CMORPH, and *(e)* PERSIANN. All panels cover 2002 – 2004 with the exception of CMORPH, which covers 2003 – 2005. Grid points in the PERSIANN dataset that were missing more than 2/3 of an individual year's values were omitted.

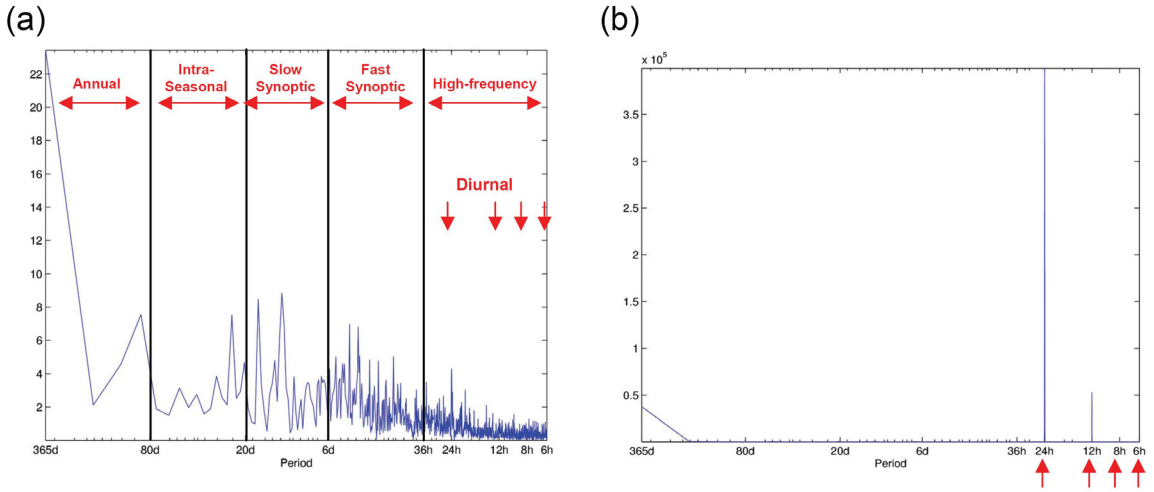

Figure 3.2: Variance category definitions demonstrated on the square-root of the 2002-2004 average RII power spectra at the ARM SGP site; (a) precipitation rate (mm/day) with variance category limits; *(b)* surface downward shortwave radiation (W/m2) with 4 diurnally forced peaks.

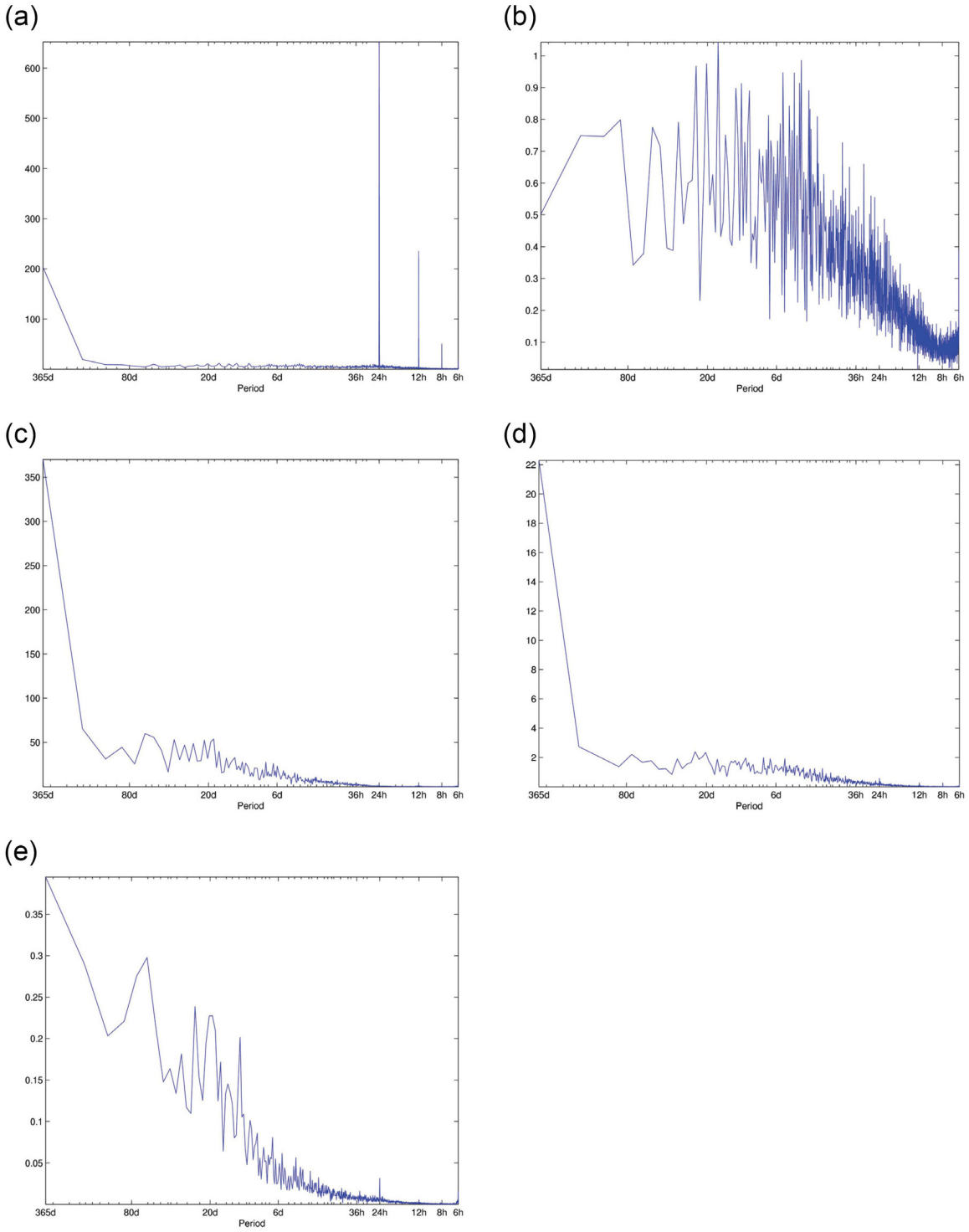

Figure 3.3: Square-root of the average 2002-2004 SFM power spectra at the ARM SGP site, of *(a)* surface downward shortwave radiation (W/m2), *(b)* precipitation rate (mm/day), *(c)* 500-hPa geopotential height (m), *(d)* precipitable water (mm), and *(e)* soil moisture content from the top 10 cm (cm).

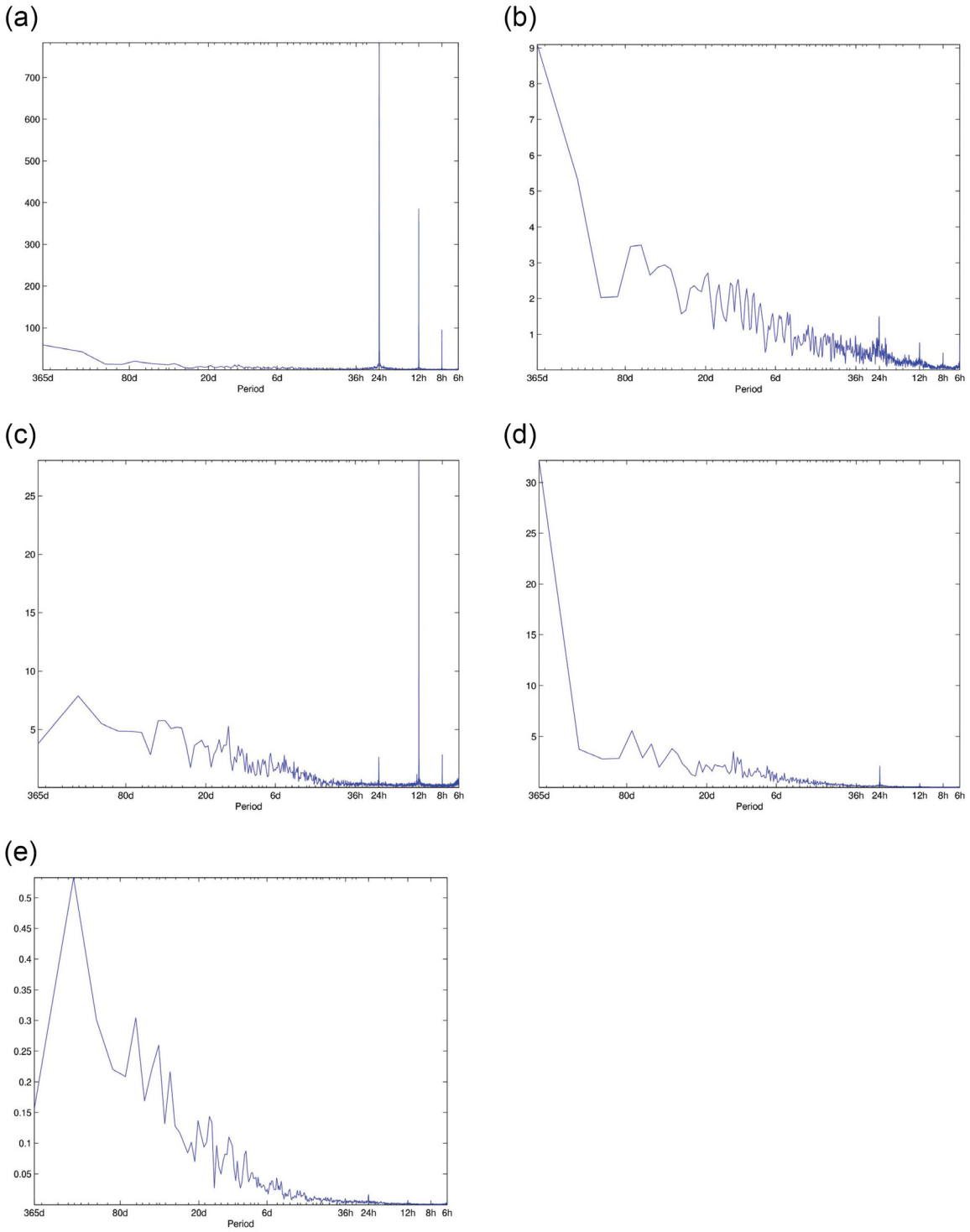

Figure 3.4: Square-root of the average 2002-2004 SFM power spectra at Darwin, Australia, of *(a)* surface downward shortwave radiation (W/m2), *(b)* precipitation rate (mm/day), *(c)* 500-hPa geopotential height (m), *(d)* precipitable water (mm), and *(e)* soil moisture content from the top 10 cm (cm).

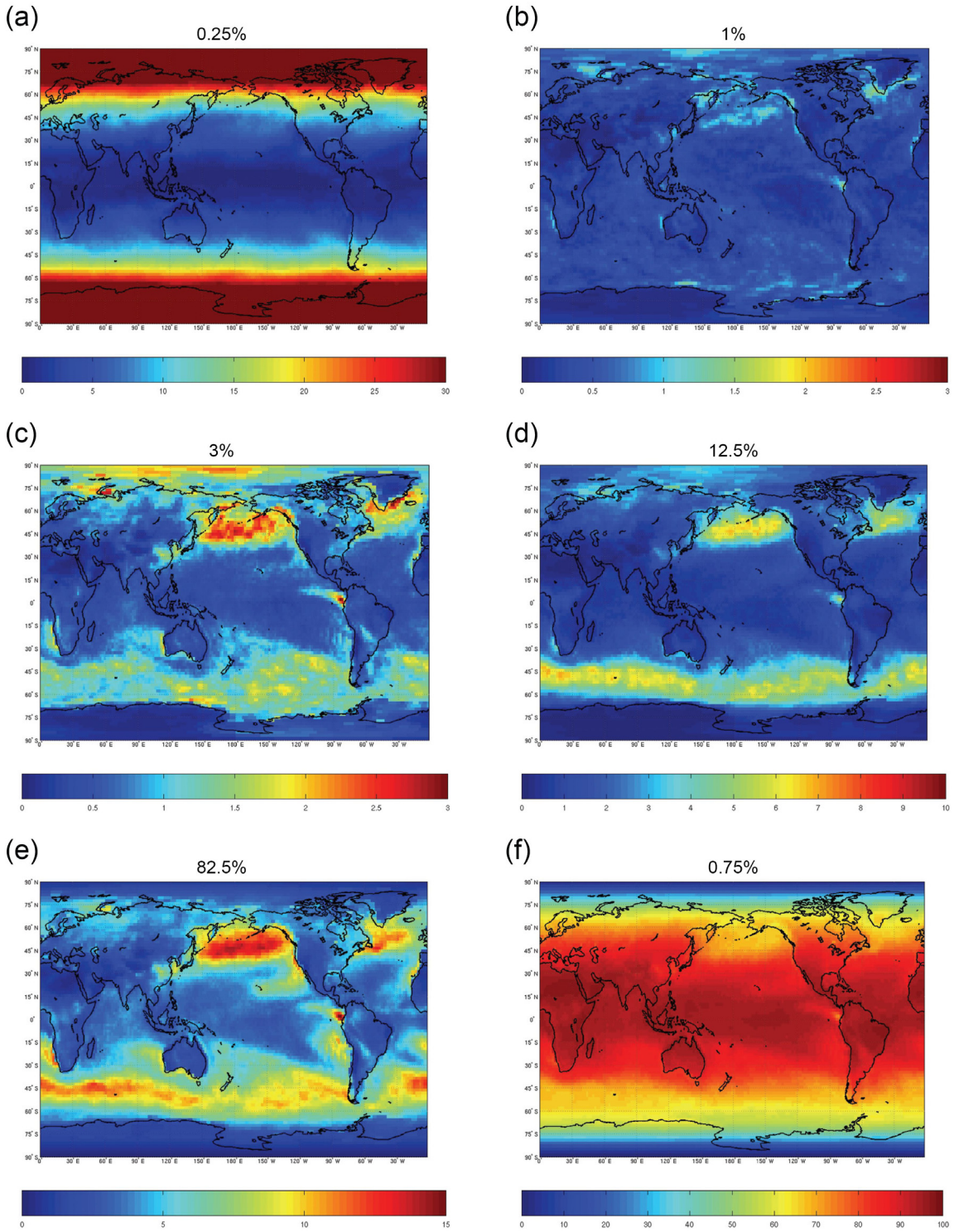

Figure 3.5: SFM surface downward shortwave radiation flux percentage variance (2002-2004) described by the *(a)* annual, *(b)* intraseasonal, *(c)* slow synoptic, *(d)* fast synoptic, *(e)* high-frequency, and *(f)* diurnal variance categories. The percentages listed show the theoretical values of each variance category from a white-noise spectrum.

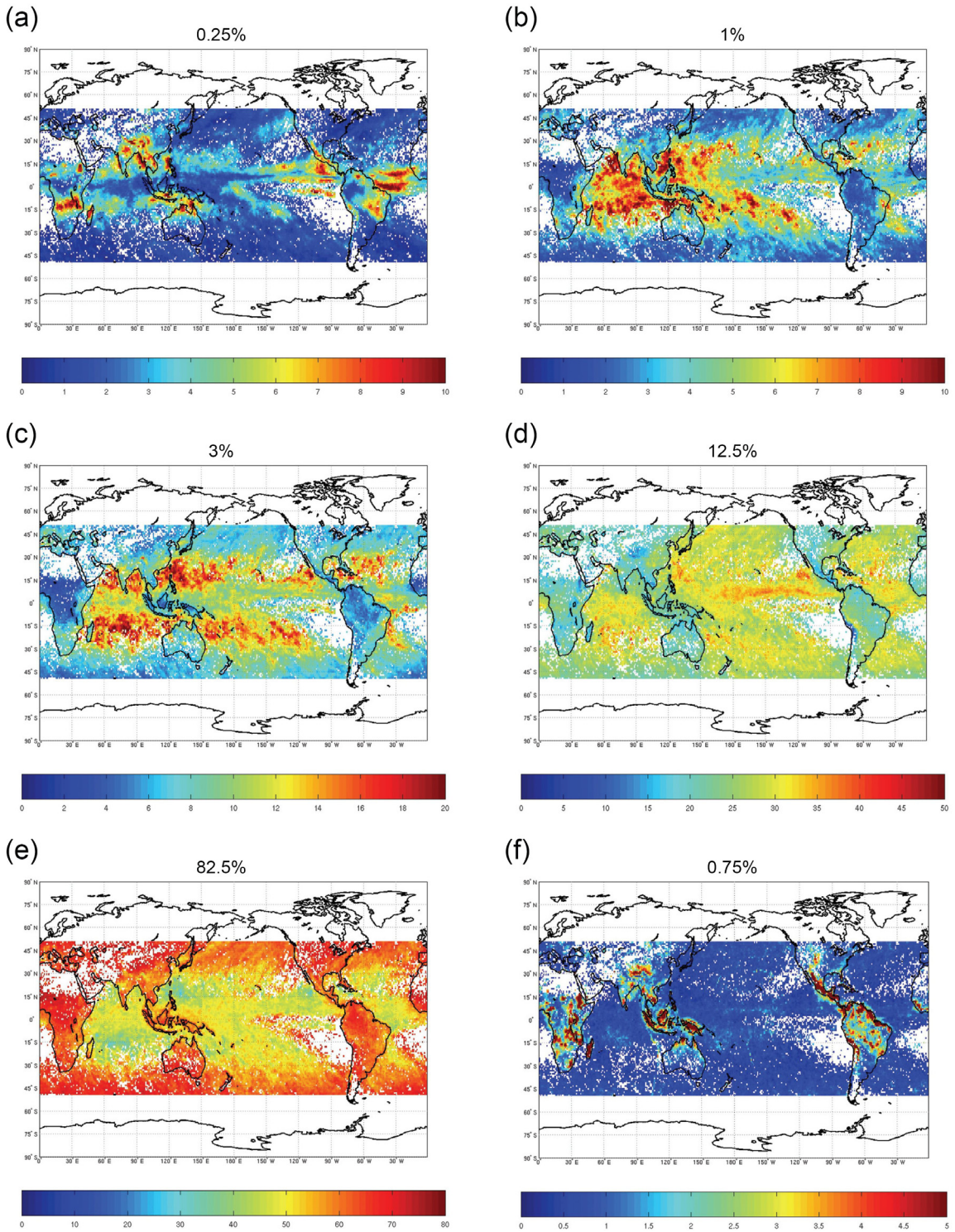

Figure 3.6: Percentage variance from the TRMM 3B-42 precipitation product (2002-2004) described by the *(a)* annual, *(b)* intraseasonal, *(c)* slow synoptic, *(d)* fast synoptic, *(e)* high-frequency, and *(f)* diurnal variance categories. The percentages listed show the theoretical values of each variance category from a white-noise spectrum.

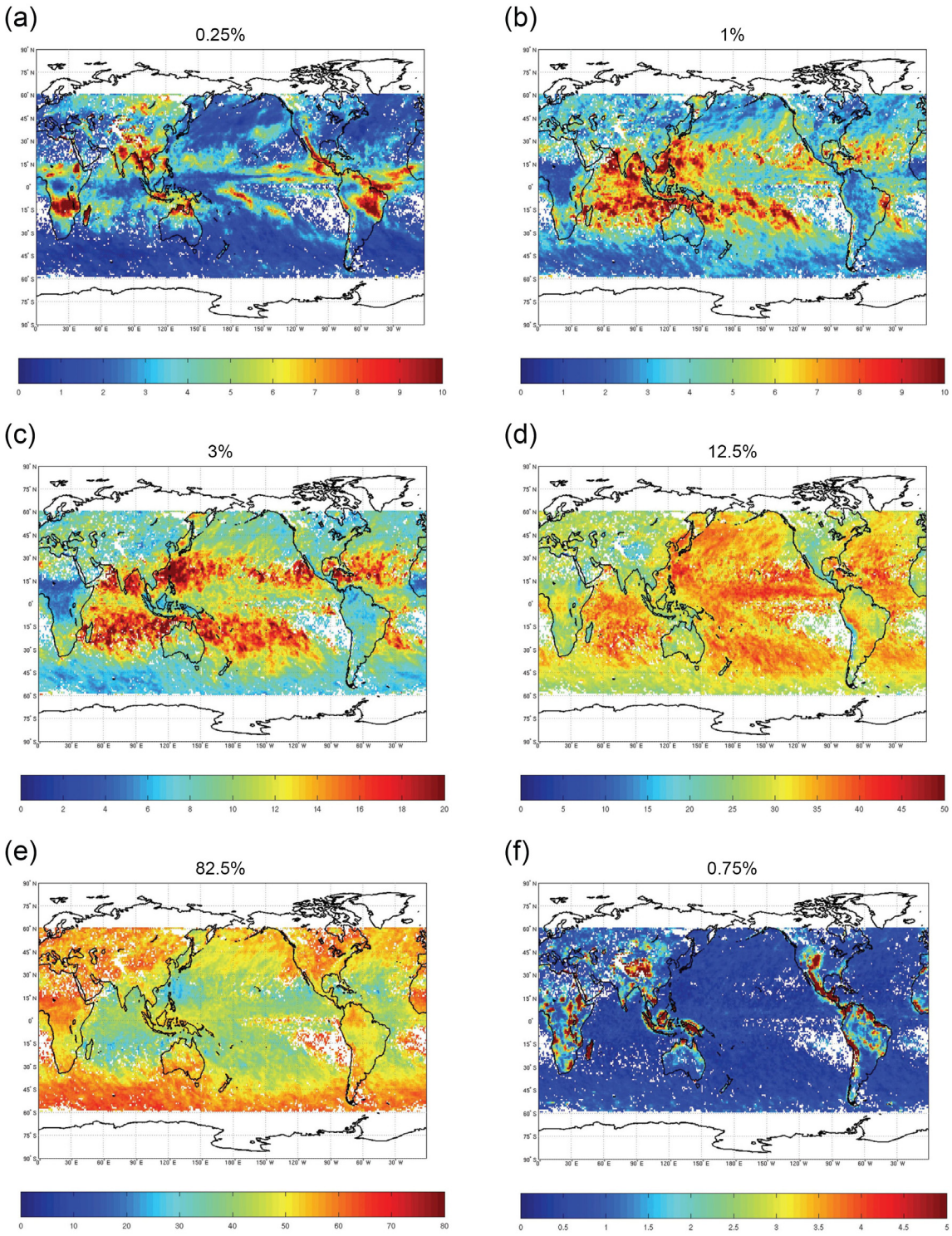

Figure 3.7: As in Fig. 3.6, but for the CMORPH precipitation product from 2003-2005.

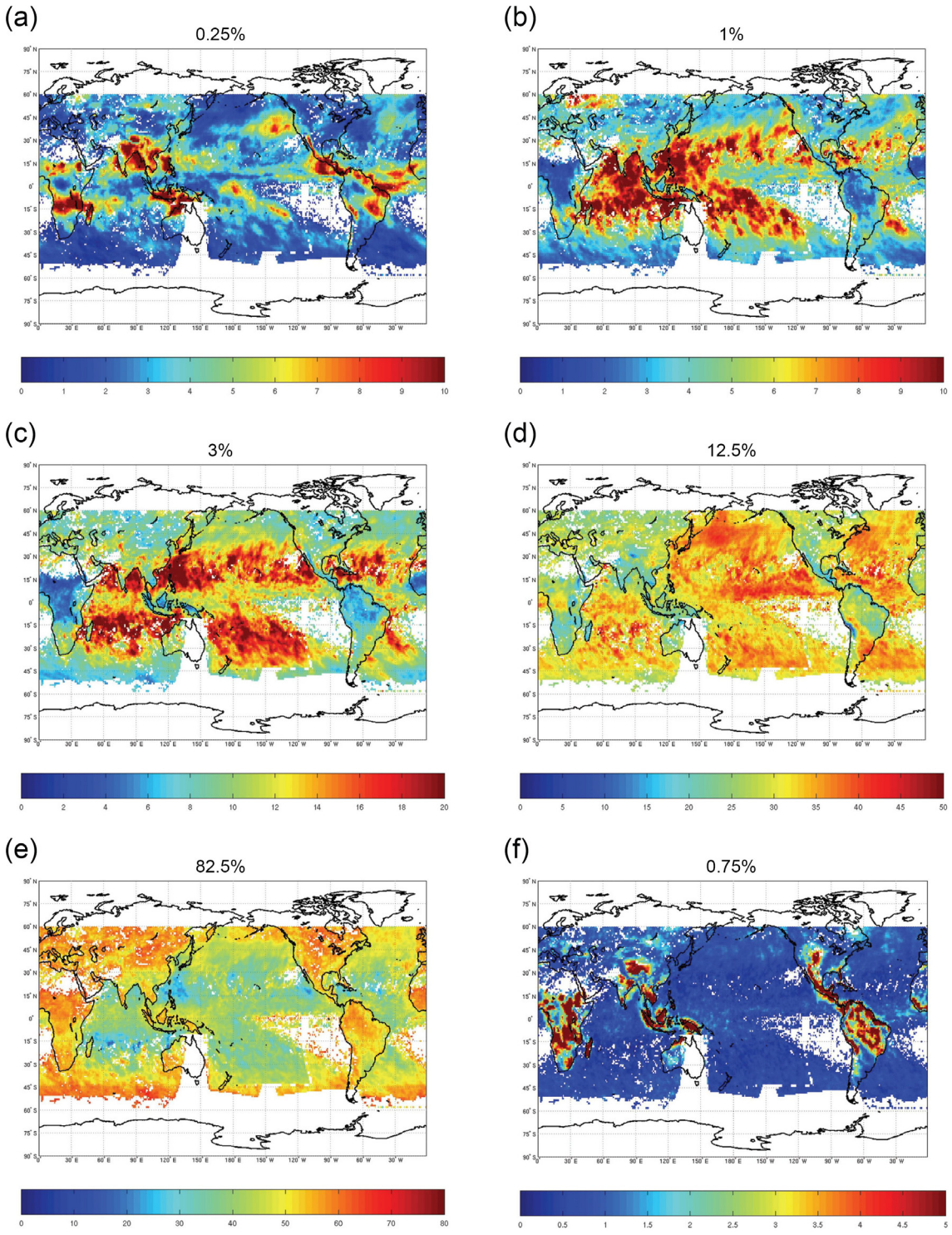

Figure 3.8: As in Fig. 3.6, but for the PERSIANN precipitation product.

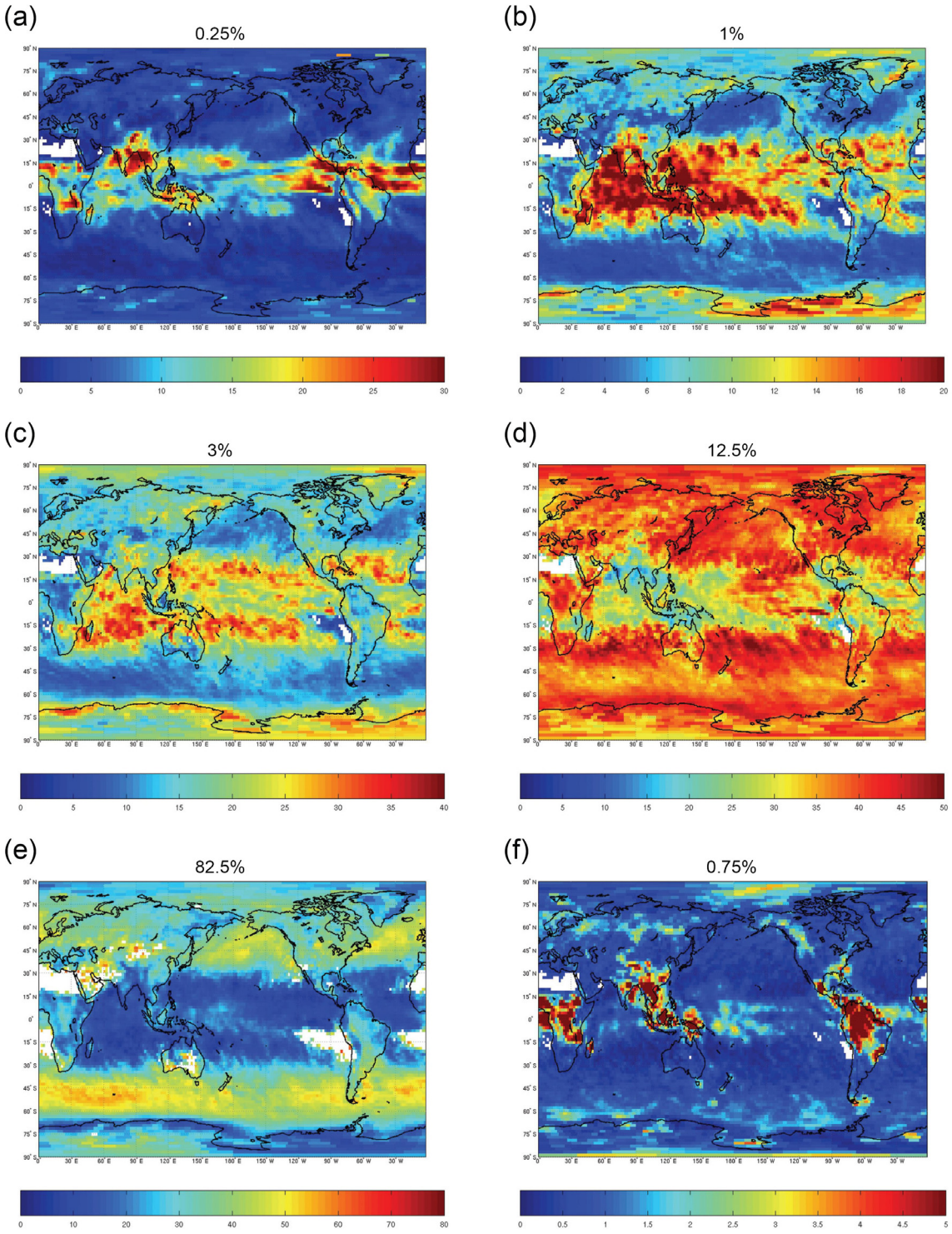

Figure 3.9: As in Fig. 3.6, but for precipitation from the SFM reanalysis. Note that the color bar limits have been altered in panels *(a)*, *(b)*, and *(c)* to show more regional detail.

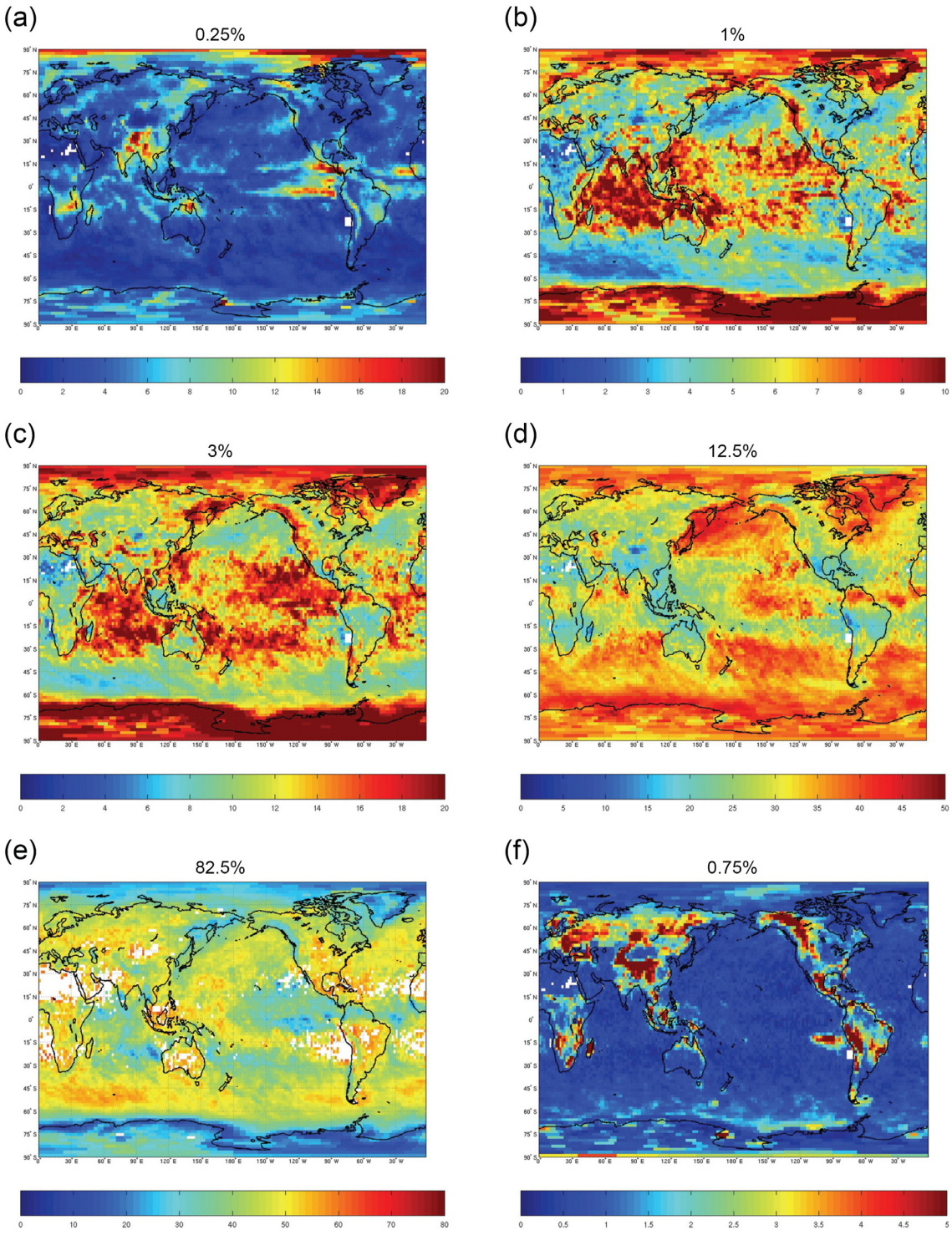

Figure 3.10: As in Fig. 3.6, but for precipitation from the RII reanalysis. Note that the color bar limit has been altered in panel *(a)* to show more regional detail.

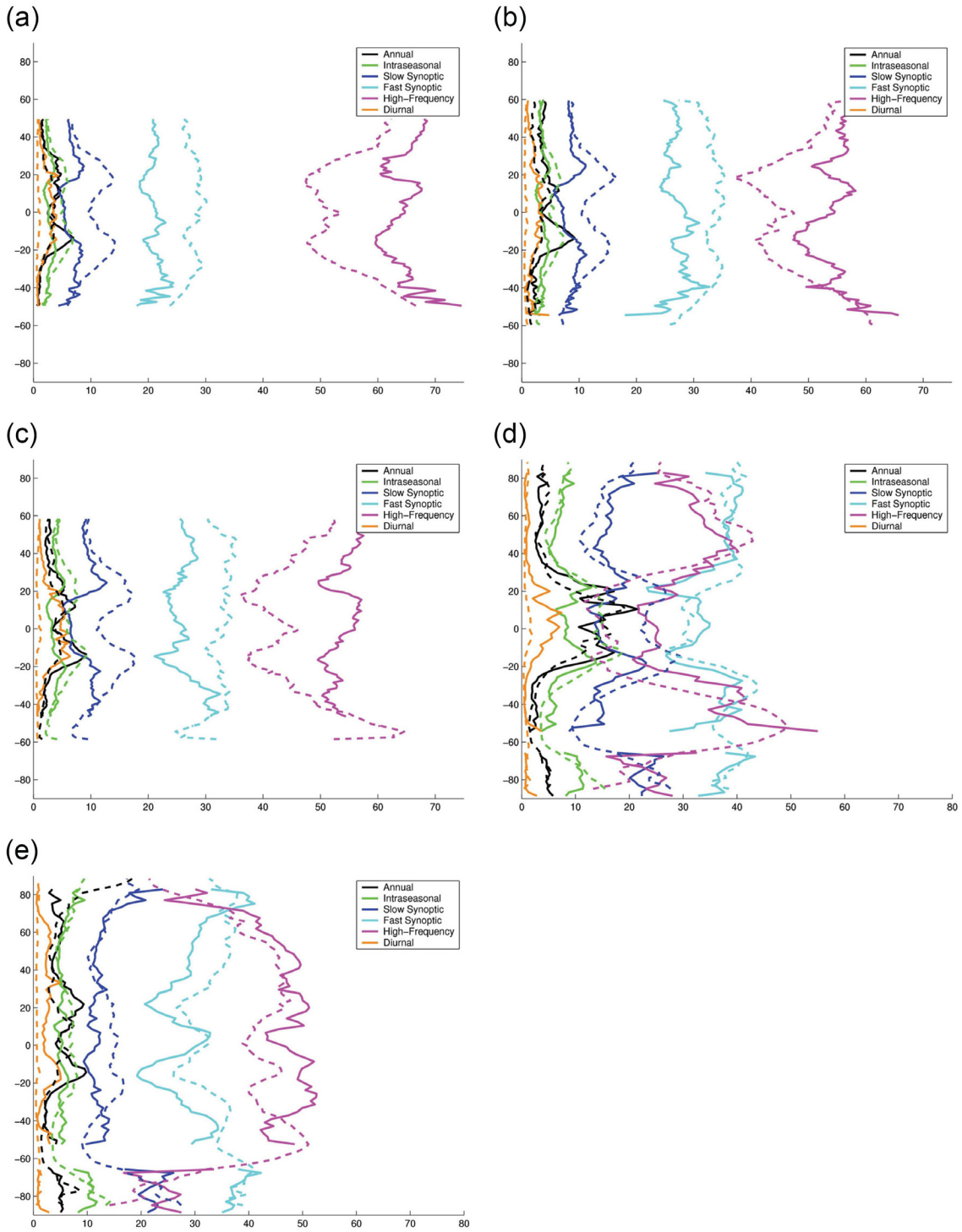

Figure 3.11: Zonal mean percentage of variance of precipitation described by each variance category from *(a)* TRMM, *(b)* CMORPH, *(c)* PERSIANN, *(d)* SFM, and *(e)* RII for land points (solid lines) and sea points (dashed lines). Note that the diurnal and high-frequency variance categories are summed together to represent an exhaustive 6-36 hour broadband.

CHAPTER IV

Dominant Balances and Exchanges of the Atmospheric Water Cycle of the Reanalysis-2 at Diurnal, Annual, and Intraseasonal Time Scales

Abstract

Output from the National Centers for Environmental Prediction / Department of Energy (NCEP/DOE) Reanalysis-2 is passed through a broadband filter to determine the normalized covariances that describe the variance of the atmospheric water cycle at diurnal, annual, and intraseasonal (7-80 days) time scales. Vapor flux convergence is residually defined to close the water cycle between successive 3-hourly output times from 2002-2004, resulting in a balance between precipitation, evaporation, precipitable water tendency, and vertically-integrated vapor flux convergence. The same balance holds at each time scale, allowing 100% of each variable's temporal variance to be described by its covariance with other water cycle components in the same variance category. Global maps of these normalized covariances are presented to demonstrate the unique balances and exchanges that govern temporal variations in the water cycle.

The diurnal water cycle is found to be dominated by a land/sea contrast, with continents controlled thermodynamically through evaporation and the oceans following dynamic convergence. The annual time scale features significant meridional structure, with the low-latitudes described mostly through variability in convergence and the extra-tropics governed by the properties of advected continental and maritime air masses. Intraseasonal transients lack direct solar oscillations at the top of the atmosphere and are

characterized by propagating dynamic systems that act to adjust the precipitable water content of unsaturated regions or exchange directly with precipitation in saturated areas.

By substituting the modeled precipitation with observation-based fields, a detailed description of the water cycle's exchanges relating to the nocturnal precipitation maximum over the US Midwest is obtained.

4.1 Introduction

Nearly all atmospheric activity is originally derived from external solar forcing. On time scales of a year and less, this forcing arrives in the form of a strong daily signal resulting from the rotation of the earth and a seasonal signal due to the Earth's orbit and inclination. The diurnal and annual cycles of solar insolation are therefore fundamental to the earth's water cycle, but do not necessarily drive an equivalent response. Energy from these solar forcings interacts with the earth system to excite other time scales, leading to many possible regimes in the water cycle's behavior.

Examinations of the water cycle have been conducted on seasonal (e.g. Roads and Betts, 1999; Roads et al., 2002) and diurnal (e.g. Anderson and Kanamaru, 2005, Lee et al., 2006) time scales. Ruane and Roads (2007a; herein referred to as RR2007a) examined the atmospheric water cycle's diurnal phase and amplitude over North America as part of an investigation into the water and energy cycles of reanalysis models, finding that parameterization errors propagate throughout the system. In particular, the convective parameterizations employed by global reanalyses were found to have a quick trigger that initiated weak convection in the afternoons over land despite the proper supply of moisture for the more diverse observed precipitation maxima.

Ruane and Roads (2007b; herein referred to as RR2007b) analyzed the variance distribution of five global precipitation sets at high temporal and spatial resolution, identifying significant regions of activity across many variance categories between 6-hour and 1-year periods. In addition to a considerable land/sea contrast, signatures of the Hadley Circulation, major monsoons, diurnal circulations, and the Madden-Julian Oscillation (MJO; Madden and Julian, 1994) were present in the three satellite-derived

precipitation products and the two reanalysis models. To further explore the role of these and other features in the water cycle, this study compliments RR2007b by analyzing the variance of balanced water cycle components; isolating unique water cycle mechanisms in many regions of the globe. The results may be used to diagnose model biases or to isolate the underlying water cycle behaviors that cause diverse regional hydroclimates.

Section 4.2 introduces the reanalysis modeling system and methodologies employed in this study, including a comparison between model spin-up and natural precipitable water tendency. Section 4.3 describes the variance of each water cycle variable through its normalized covariance with the other components of the water cycle at diurnal, annual, and intraseasonal time scales. This process is repeated in Section 4.4 utilizing a satellite-derived precipitation product to replace modeled precipitation, followed by a brief conclusion in Section 4.5.

4.2 Datasets and Methodologies

4.2.1. The NCEP/DOE Reanalysis-2 Model

Simulations of the National Centers for Environmental Prediction and Department of Energy (NCEP/DOE) Reanalysis-2 model (herein referred to as the R2; Kanamitsu et al., 2002b) are the basis of this study. The R2 is a global spectral model utilizing a primitive equations system of virtual temperature, humidity, surface pressure, momentum prognostic equations, and various physical parameterizations (for land-surface processes, precipitation, radiation, etc.). Precipitation and evaporation are put out on a 192x94 Gaussian grid (each pixel ~1.9º across), but the model uses 62 spherical harmonics with a

triangular truncation and 28 σ-levels (T62L28). Vertically-integrated variables (such as precipitable water) are calculated from their comprehensive model values to prevent interpolation errors.

The model output examined here covers 2002-2004 and was generated as part of the Experimental Climate Prediction Center's contribution to the Coordinated Enhanced Observing Period (CEOP; Koike, 2004; Lawford et al., 2006). This time period also facilitates comparisons with the precipitation sets examined in RR2007b. Augmented 6-hour forecasts were initialized from reanalyzed observations four times each day (at 00, 06, 12, and 18UTC), and successive 3-hour and 6-hour forecasts link together to form a comprehensive time series. Each forecast time represents the 3-hour period preceding it from the same initialization, so a 6-hour forecast of precipitation represents the mean precipitation rate between 3-6 hours of model time, for example. As precipitation and evaporation are not assimilated, these short model forecasts are required to simulate the water cycle's evolution from the assimilated atmospheric states.

Notable parameterizations employed by the R2 include the Simplified Arakawa-Schubert convection scheme (SAS; Pan and Wu, 1995) and the Oregon State University Land-Surface Model (OSU2; Pan and Mahrt, 1987). To prevent run-away soil moisture values, adjustments in the reanalysis are made according to biases between simulated and observed precipitation over each 5-day pentad (see Lu et al., 2005, for a full description). The model's atmosphere is forced by weekly mean sea-surface temperatures (SSTs) that are linearly-interpolated into mean daily values, resulting in diurnally constant SSTs. This assumption stems from the fact that the open ocean surface's large heat capacity drastically diminishes the daily range of surface temperature compared to land.

Diurnally constant SSTs therefore have only a small impact on the diurnal magnitude of turbulent energy fluxes, but the phases are strongly affected (RR2007a).

4.2.2. Water Cycle Balance

At any given time, the total amount of water vapor in the atmospheric column is represented by the precipitable water

$$w = \int_0^1 \pi q \partial\sigma , \qquad (4.1)$$

where q is the specific humidity and π represents the atmospheric mass, which is the surface pressure divided by gravity: $\pi = p_s/g$. The tendency of precipitable water between successive model output times may be calculated via

$$T = \frac{1}{t - t_0} \int_{t_o}^{t} \frac{\partial w}{\partial t} \partial t . \qquad (4.2)$$

Precipitable water tendency has both a natural and a model component, the latter a result of model biases, spin-up, and reinitializing the atmospheric state every 6 hours. These dual tendency components may be separated by comparing overlapping forecasts from successive initializations, and are discussed in more detail in Section 4.2.5.

While vertical vapor fluxes do not change precipitable water content, the precipitable water amount does change due to horizontal convergence of vapor flux, given by

$$C = -\int_0^1 \left(\vec{\nabla} \bullet \pi q \vec{v} \right) \partial\sigma . \qquad (4.3)$$

Atmospheric moisture may also be added through evaporation (E) from the surface or lost to precipitation (P) that falls out of the column. Together, the exchanges of the water cycle may be balanced by

$$T = C + E - P \quad . \qquad (4.4)$$

In short, any exchange of moisture through one of these four processes must be balanced by changes in the others. Vapor convergence and evaporation add moisture to the column, leading to either a positive moisture tendency or a corresponding loss of moisture through precipitation. Dominant balances occur when two terms dwarf the other two components of the water cycle, while dominant exchanges exist when moisture is commonly interchanged between two components in a given region, regardless of their magnitude.

The output of the R2 allows exact accounting for the *T*, *E*, and *P* terms of this balance in principle, but puts out only instantaneous values of *C*. Interpolations of these instantaneous values do not correctly represent the variation of horizontal vapor fluxes over a 3-hour period, so vapor flux convergences in this study were residually calculated ($C=T-E+P$) to perfectly close this balance for every forecast time. A similar residual vapor flux convergence closure compared favorably with comprehensive output over North America in RR2007a, where it even captured the nocturnal maximum seen over the upper Midwestern United States.

T is derived from assimilated observations, but each term on the right-hand-side of *Eqn. 4.4* is driven by a different mechanism in the R2. *C* is determined by dynamic activity throughout the atmospheric column, although changes in motion in the moist lower troposphere generally have the greatest influence on the water cycle. *E* is a function of the atmospheric boundary layer's thermodynamic influence on evaporative parameterizations, and is therefore strongly affected by radiative forcings (see e.g. RR2007a). *P* is heavily parameterized in the R2, and is therefore dominated by the

triggering mechanisms and dynamic algorithms hard-wired into the SAS convection scheme, although boundary layer and other parameterizations also feed into the environmental conditions that drive convection. Like the other convection schemes noted by Trenberth et al. (2003), SAS convective precipitation is too light and initiates prematurely over many land areas.

Each term in *Eqn. 4.4* may also be considered as a sum of its mean (denoted with an overbar) and transient (denoted by a prime) components

$$\left(\overline{T}+T'\right)=\left(\overline{C}+C'\right)+\left(\overline{E}+E'\right)-\left(\overline{P}+P'\right) \quad . \qquad (4.5)$$

The atmospheric water balance therefore holds over both the long-term mean and among the transients at any orthogonal frequency

$$\overline{T}=\overline{C}+\overline{E}-\overline{P} \quad , \qquad (4.6a)$$

$$T'=C'+E'-P' \quad . \qquad (4.6b)$$

4.2.3 Mean Water Cycle Balance

Following *Eqn. 4.6a*, the mean of each water cycle component over the 2002-2004 period is shown in **Fig. 4.1**. As expected, $\overline{P}$ is strongest in the Inter-Tropical Convergence Zone (ITCZ) and over the Indonesian Warm Pool. The storm track regions just downwind of the Kuroshio and Gulf Stream also appear as local maxima. $\overline{E}$ is strongest over these western boundary currents as well as where large-scale subsidence from the Hadley circulation provides hot and dry air over warm subtropical oceans. Moist and arid continental regions also have noticeable differences in $\overline{E}$. The residually defined $\overline{C}$ identifies a pattern of divergence from the high-evaporation

regions over the subtropical oceans and convergence in the ITCZ. Weak net convergence is also apparent in the storm track areas over the mid- and high-latitude oceans. Over long time periods the precipitable water tendency is expected to be negligible, as accumulated vapor flux convergence, evaporation, and precipitation are far greater than their net impact on the reservoir term. $\overline{T}$ is the smallest term in the mean balance, but its non-negligible values indicate the importance of model tendencies; these are discussed further in Section 2.5.

4.2.4 Transient Water Cycle Balance

Global maps of the transient balances of the water cycle (*Eqn. 4.6b*) for the diurnal, annual, and intraseasonal time scales were generated in a 4-step procedure. First, time series of the deviation from the annual mean of each component of the water cycle were generated at each grid point (see e.g. **Fig. 4.2a**).

Second, each component's series were bandpass-filtered using a fast-Fourier transform (Emery and Thomson, 2004) that casts each component into frequency space and isolates orthogonal frequencies in the three variance categories shown in **Fig. 4.2b**. The annual category contains variance with periods between ~80-365 days, containing seasonal shifts such as the monsoons and the migration of the ITCZ. The intraseasonal category captures variance between 7 - ~80 days, which is independent from direct solar forcing oscillations at the top of the atmosphere and includes the frequencies associated with the MJO and many propagating synoptic systems. Variance categories between 6-hours and 7-days, with the exception of the exact diurnal frequencies, were not examined here.

Our definition of the diurnal category is based upon the spectral signature of diurnal solar forcing (**Fig. 4.2c**). The sharp peaks generated by the solar radiation correspond to the 4 harmonics (with 24-hr, 12-hr, 8-hr, and 6-hr periods) that are needed to capture the mean diurnal cycle at 3-hourly resolution, but the mean diurnal cycle is not repeated consistently every day. Over a full year, many slightly different daily realizations broaden the spectral peaks, so the diurnal variance category is defined to capture at least 98% of the variance of each of these sharp solar forcings in narrow bands that contain three frequencies centered upon each diurnal peak. **Figure 4.2d** shows the bandpass-filtered diurnal, annual, and intraseasonal variance categories for 2002 precipitation for the grid point that contains Lindenberg, Germany. By capturing slightly offsetting frequencies around these diurnal peaks, a longer time scale is aliased that retains seasonal adjustments in the magnitude of the diurnal variation. For example, the narrow bands that define the diurnal variance category capture a seasonal adjustment in the diurnal range of incoming solar radiation (not shown), reaching a maximum at the summer solstice (Julian day 202) and a minimum near the winter solstice (Julian day 355). The annual and diurnal categories both show an increase in magnitude during the warmest portion of the year when continental convection is at its maximum. The lowest diurnal range occurs in the late winter (near Julian day 70), when convection is at a minimum. These variance categories are similar to those used in RR2007b, but the intraseasonal band is expanded.

Third, after the components have been bandpass-filtered and cast back into a 3-hourly time series, the variance of each component

$$\mathrm{var}(A') = \frac{1}{N-1}\sum_{1}^{N}(A')^2 \qquad (4.7)$$

as well as the covariance between the various components

$$\mathrm{cov}(A', B') = \frac{1}{N-1}\sum_{1}^{N} A'B' \qquad (4.8)$$

is calculated for every grid point each year.

Equation 4.6b indicates that any deviation in one component of the water cycle must be matched by change in other components. This balance may be extended into variance by calculating the covariance of each term in the equation to a particular variable, then normalizing by the variance of that variable. As an example, for the tendency term, this is equivalent to multiplying each nth member of the bandpass-filtered time series in *Eqn. 4.6b* by $T_n'/\Sigma([T']^2)$ and then performing a summation over all *n*. With some rearrangement, and bringing negative signs inside the covariance to enable a convenient sum between terms, we have:

$$\frac{\mathrm{cov}(P', P')}{\mathrm{var}(P')} \times 100\% = \frac{\mathrm{cov}(E', P') + \mathrm{cov}(-T', P') + \mathrm{cov}(C', P')}{\mathrm{var}(P')} \times 100\% = 100\% \quad , \quad (4.9a)$$

$$\frac{\mathrm{cov}(E', E')}{\mathrm{var}(E')} \times 100\% = \frac{\mathrm{cov}(P', E') + \mathrm{cov}(T', E') + \mathrm{cov}(-C', E')}{\mathrm{var}(E')} \times 100\% = 100\% \quad , \quad (4.9b)$$

$$\frac{\mathrm{cov}(T', T')}{\mathrm{var}(T')} \times 100\% = \frac{\mathrm{cov}(-P', T') + \mathrm{cov}(E', T') + \mathrm{cov}(C', T')}{\mathrm{var}(T')} \times 100\% = 100\% \quad , \quad (4.9c)$$

and $$\frac{\mathrm{cov}(C', C')}{\mathrm{var}(C')} \times 100\% = \frac{\mathrm{cov}(P', C') + \mathrm{cov}(-E', C') + \mathrm{cov}(T', C')}{\mathrm{var}(C')} \times 100\% = 100\% \quad . \quad (4.9d)$$

These "normalized covariances" indicate the portion of one component's variance that is matched by another. As an example, the first term in the center portion of *Eqn. 4.9a* indicates the percentage of precipitation's variance that corresponds to variance of evaporation. Although covariance is commutative (*cov[A',B']=cov[B',A']*), the terms in the center portion of *Eqns. 4.9a-d* are not commutative because they are normalized by

a single component's variance, although complimentary terms will always have the same sign.

Each of these normalized covariance terms indicates a potential dominant balance or exchange in the atmospheric water cycle. For example, if there was no change in precipitable water tendency or vapor convergence, any increase in evaporation must be matched with precipitation. If there was no variation in evaporation or vapor convergence, any precipitation event must be removing moisture from the column, causing a negative tendency in precipitable water. If precipitation and the tendency term were held constant, evaporation into the column must be matched by an equal vapor flux divergence.

Finally, maps of these normalized covariances (*Eqns. 4.9a-d*) are produced by averaging the normalized covariant percentages at each grid point over the three annual segments in each variance category. As each component's variance may be explained by its normalized covariance with the other three components of the water cycle, the sum of these three maps are exactly 100% at every grid point. If the percentage normalized covariance between two components in a given variance category ranges more than 100% between years over a particular grid point, it is omitted for displaying too much uncertainty in its interannual variation (white portions of the figures). The strength of this method is its ability to confidently explain the comprehensive variation of a component's deviations in a particular variance category, so if uncertainty exists in any normalized covariant term the grid point is omitted in all other terms of the same balance. These maps (representing *Eqns. 4.9a-d*) form the primary bases for examinations in this study.

Heeding the warnings by Randall et al. (1991), it is both tempting and incorrect to use the normalized covariances to fully delineate the cause of particular patterns. These maps really indicate coincident behaviors; a determination of which component caused the changes in the other components requires additional analysis and physical insight, which is provided in Section 3 for select features. This procedure will underemphasize lagged responses in the atmosphere, as differences in phase will appear only as a reduction in the magnitude of the simultaneous normalized covariance.

4.2.5 Model versus Natural Tendencies

A water cycle imbalance due to model error tendency (introduced by successive re-initializations of the NCEP/National Center for Atmospheric Research Reanalysis) has been identified by a number of authors, including Trenberth and Guillemot (1995, 1998). In contrast to their work (which also used a residual technique to compute an *E-P* term at monthly and longer time scales) precipitable water tendency is computed here at much shorter 3-hourly intervals (*Eqn. 4.2*) where the budget is balanced. Although the natural precipitable water tendency is negligible on long time scales, Randall et al. (1991) recognized that the tendency term may be significant on shorter time scales. RR2007a also noted a significant diurnal tendency component over North America in three different reanalysis systems due in part to convective parameterization errors. To fully understand the implications of the normalized covariances in Sections 4.3 and 4.4, it is important to determine whether the tendency variations are due to its model or natural components.

The format of the reanalysis experiment allows for a clear separation of these two components on 6-hourly time scales due to an overlap of the instantaneous 6-hour precipitable water forecast and the analysis field of the next initialization (see **Fig. 4.3**). These dual, coincident states may be compared to the precipitable water field 6 hours later to provide insights into model and natural behavior. As noted above, the evolution of precipitable water from its analysis field to a 6-hour forecast contains both model error (*ET*) and natural (*NT*) tendencies

$$T = ET + NT = \frac{w_{06,06} - w_{06,00}}{0.25 days}, \qquad (4.10)$$

where $w_{06,00}$ indicates the 00-hour forecast (analysis) of precipitable water from a 06UTC initialization. The tendency between the 6-hour forecast and the previous 6-hour forecast is indicative of the natural processes according to the model's assimilation system

$$NT = \frac{w_{06,06} - w_{00,06}}{0.25 days} \quad . \qquad (4.11)$$

The model error tendency may therefore be estimated by subtracting the natural tendency from the total tendency over a 6-hour forecast period

$$ET = T - NT = \frac{w_{00,06} - w_{06,00}}{0.25 days} \, . \qquad (4.12)$$

To understand the role of these two tendency terms, analysis of the 6-hourly time series from 2002-2004 was conducted in a corresponding manner to the methodology in Section 2 (not shown). $\overline{NT}$ is less than 0.1 mmday^{-1} across the entire globe, more than 50 times smaller than $\overline{ET}$, which is nearly identical to the $\overline{T}$ shown in **Fig. 4.1c**. In addition to large biases over arid regions, wave patterns in and around

major mountain ranges suggest the influence of a topographical mechanism in model error tendency. The variance of *NT'* exceeds the variance of *ET'* in the diurnal and intraseasonal category, although the variance of *ET'* is much larger in the annual category. Regions with dense upper-air measurements show particularly strong *ET'* variance, as do island rawinsonde stations (forming bulls-eyes similar to those seen by Trenberth and Guillemot, 1998).

The *T'* terms shown in the following sections contain both *ET'* and *NT'*, but several patterns emerged from analysis of the 6-hour separated model error and natural tendency transients (not shown). On the diurnal time scale (Section 4.3.1) patterns relating to *T'* are overwhelmingly due to *NT'*. Intriguingly, however, *ET'* acts to reduce regional anomalies in the covariance of *T'* and *E'*. On the annual time scale (Section 4.3.2) *NT'* is negligible, so patterns in *T'* match *ET'*. On intraseasonal time scales (Section 4.3.3) *T'* variance is small and mostly explained by *NT'*, although *ET'* makes a significant contribution to *T'* over land.

4.3 Transient Behavior of the Water Cycle

Maps of the normalized covariances of various water cycle components are shown in this section for diurnal (**Fig. 4.4**), annual (**Fig. 4.5**), and intraseasonal (**Fig. 4.6**) time scales. These maps are displayed in sets of threes to enable the full depiction of a particular variable through its normalized covariance with the other three components. For example, the sum of the three panels in the first row of **Fig. 4.4** describes 100% of the daily variance of *P'* at all points on the globe. **Figure 4.4a** examines the normalized covariance of evaporation to precipitation; equivalent to the cov*(E',P')*/var*(P')* term in

Eqn 4.9a. The other two maps in the first row correspond to the next two terms in this equation. A grid point showing a normalized covariance of 100% in **Fig. 4.4a** indicates that the variance of *E'* accounts for the entire variance of *P'*. A grid point showing 0% indicates no relationship between the variations of the two variables. A grid point showing <0% indicates that *E'* and *P'* co-vary, but with opposite phase. A grid point displaying a normalized covariance >100% has *E'* and *P'* co-varying in approximate phase, but with *E'* displaying a larger magnitude than *P'*. It should also be noted again that, because of the differing normalizations, the normalized covariance of evaporation to precipitation (**Fig. 4.4a**) is different than the normalized covariance of precipitation to evaporation (**Fig. 4.4d**).

4.3.1 Diurnal Variance Description

Normalized covariances of the water cycle components' diurnal variability are shown in **Fig. 4.4**. It is immediately apparent that there is a strong land/sea contrast in nearly all of the diurnal components. The land surface's low heat capacity leads to strong diurnal variations, but the R2 may overly diminish diurnal variations over the oceans due to diurnally constant SSTs (as discussed in Section 2.1). The constant thermodynamic state over the oceans leads to low diurnal evaporation variance over the oceans, providing a negligible denominator that leads to a wide interannual range in normalized covariances in **Figs. 4.4d-f**. As a result, the dynamic vapor flux convergence component drives most variance in the water cycle over the oceans at this time scale (**Figs. 4.4c,i**). Over the ocean, precipitation also receives a small portion of its moisture through an erosion of the precipitable water reservoir (**Fig. 4.4b**).

The normalized covariances that describe the variance of precipitation (**Figs. 4.4a-c)** are insignificant over arid and stratocumulus regions where large-scale subsidence inhibits precipitation. It is not surprising to see strong co-varying *E'* and *P'* over land (see e.g. Anderson et al., 2007). As the incoming solar radiation reaches its peak at midday, surface temperatures rise rapidly and evaporation peaks shortly thereafter. The evaporated moisture increases lower-tropospheric moisture availability and promotes afternoon convection in the destabilizing atmospheric column. The normalized covariance of *E'* to *P'* demonstrates that evaporation displays much more variance than the less-consistent precipitation over the Northern Hemisphere continents (more than twice as much in many places), but the two components have a similar phase. This imbalance is remedied by a seemingly counter-intuitive diurnal relationship between P' and T', where diurnal precipitation variability seems to be in phase with gains in the water column. Of course precipitation events do not add more moisture into the atmosphere, but this feature is a result of a conglomeration of many daily realizations that display fundamentally different traits. Although infrequent convective events are large, the regular evaporative signal dominates the diurnal variability of precipitable water tendency over any given year despite its relatively small diurnal amplitude. Therefore *P'* and *T'* share the same diurnal phase even if they do not occur on the same days.

The normalized covariance description of T' variance in **Figs. 4.4g-i** reinforces this explanation and displays the clear contrast between the thermodynamic control of the continents' water cycle and the dynamic control of the oceans' water cycle. As mentioned in the previous section, the variance of *T'* on the diurnal scale is dominated by its *NT'* component. The largest portion of diurnal *T'* variance over land is described by

variance in *E'* (particularly at higher latitudes), while over the ocean it is described by *C'*. It is therefore important to examine these two components (**Figs. 4.4d-f, 4.4j-l**) to determine the fate of moisture that is in either of these two dominant processes. Over land, moisture that is evaporated goes mostly into an increase in the precipitable water, although at higher latitudes it can be recycled into precipitation. At lower latitudes and in arid regions, evaporation often corresponds to divergent moisture flux. Over the oceans, moisture that converges into a region mostly results in an increase in the precipitable water, although precipitation also may occur outside of the stratocumulus regions. The lack of correspondence between *E'* and *–C'* suggests that either a large portion of the divergence occurs outside of the nearly saturated boundary layer, or that there is a significant lag in the response of the ocean surface.

It is also interesting to note several other features in the diurnal variance descriptions. Over tropical Africa, Mexico, and along and just off of many coastlines, diurnal *P'* corresponds to enhanced *C'* (**Fig. 4.4c**) where local circulations (e.g. land/sea breezes) provide moisture advection into a region during a particular time of day. Over the lush tropical land masses of the Amazon and Indochina where humidity is consistently very high, all components of the water cycle have comparable variance with a nearly common phase (**Figs. 4.4a-c**). Precipitation in these regions draws from evaporation and moisture flux convergence while still drawing down the atmospheric water column. Over high latitude land masses, diurnal variations in vapor flux convergence are insignificant (**Figs. 4.4j-l**), likely owing to the low moisture content of the cold continental air masses. Similar to RR2007a's North American results, only weak regional variation is evident in the behavior of the diurnal water cycle between

warm and cold portions of the ocean or high and low elevation regions, although meridional and soil moisture variations are apparent.

4.3.2 Annual Variance Description

Normalized covariance maps describing the annual variance of water cycle components are presented in **Fig. 4.5**. The most striking aspect of annual variance is the meridional shift in character which is apparent in nearly all component interactions. Seasons have a larger radiative impact at higher latitudes, and the lower heat capacity of land surfaces also enables larger shifts in temperature than occur over the ocean.

Annual variance in the tropics is dominated by the converging portion of the Hadley Circulation, which draws moist lower-tropospheric air into the Inter-Tropical Convergence Zone (ITCZ). Both *P'* and *E'* have a dynamic Hadley signature, with tropical precipitation dominated by convergence (**Fig. 4.5c**) and subtropical evaporation over the oceans corresponding to the diverging regions underneath the descending portions of the circulation (**Fig. 4.5f**).

Many of the annual behaviors occur on land as well as over the oceans. *C'* and *P'* form the dominant balance throughout the tropics, but also extend their influence over the regions associated with the South and Southeast Asian monsoons. In these areas, large seasonal influxes of moisture correspond to heavy precipitation. A slight seasonal exchange of *T'* to *P'* over the low-latitude continents is apparent in **Figs. 4.5b,g**, although this is due mostly to the *ET'* component that dominates the annual tendency variance. *E'* also closely corresponds to the *ET'* variations on this time scale over arid regions, indicating that model evaporation interacts strongly with the model tendencies in these

locations, although annual variance for both of these terms is small in comparison to that of precipitation and vapor flux convergence. Annual water cycle variations are largely a balance between the *E'*, *C'*, and *P'* components, reflecting the diminished importance of the tendency terms on this scale.

Seasonal air masses dominate the behavior of the water cycle at higher latitudes. The continental water cycle is dominated by thermodynamic controls due to the low surface heat capacity, with large increases in summertime evaporation accompanied by enhanced precipitation (**Fig. 4.5a**) and a sight divergence of water vapor in comparison to strong wintertime dynamical convergence over the continent (**Fig. 4.5k**). *E'* variance (**Figs. 4.5d-f**) is described by a fairly even distribution of moisture to P' and *–C'* in these areas. Marine air masses precipitate in phase with annual variance in both evaporation and vapor flux convergence (**Figs. 4.5a-c**), taking on both a dynamic and thermodynamic exchange.

Large shifts in the water cycle behavior accompany the transition from continental to marine properties as air masses propagate from west to east across the ocean basins. After a long crossing of a relatively dry landmass, continental air masses pick up a lot of evaporated moisture as they move over the Kuroshio or the Gulf Stream (**Fig. 4.5a**; note also that a similar pattern exists downwind of the Sahara and over the Somali Current). Until they approach a more saturated lower troposphere, the air masses' water cycle continues to act as if it were still over land, with thermodynamically dominated precipitation that is likely still convective in nature. As the air masses move into the central and eastern ocean basins they begin to act more like the nearly-saturated tropical atmosphere as dynamical vapor convergence plays a larger role. At these

higher latitudes, however, the dominant precipitation signal (likely stratiform in nature) is matched by both a large amount of convergent moisture exchange (**Fig. 4.5j**) and seasonal evaporative input (**Fig. 4.5d**). Upon reaching the western coastlines of continents the saturated air masses converge and dump a large amount of precipitation, particularly where orographic lifting squeezes the atmospheric column in the Coastal Ranges of North America (**Fig. 4.5a,c**).

Other annual variance features are also noteworthy. The narrow equatorial Eastern Pacific feature seen in many of the panels is a signature of the double ITCZ that appears over the cold tongue of SSTs in the Boreal Spring. When this double ITCZ forms, the area on the northern edge of the cold tongue that lies between the two narrow convective bands has enhanced divergence and evaporation, leading to a reduction in precipitation. When the convergence returns after the collapse of this feature, precipitation initiates rapidly. Evaporation does not vary strongly enough to be significant in the vast majority of the moist tropics on these long time scales (**Figs. 4.5d-f**), but when it does occur in the stratocumulus regions it acts as a source of atmospheric moisture through its exchange with vapor flux divergence (**Fig. 4.5k**).

4.3.3 Intraseasonal Variance Description

The normalized covariances describing the water cycle's intraseasonal variance are provided in **Fig. 4.6**. The intraseasonal band is unique in that it is the broadest of the three variance categories examined here and lacks any direct solar forcing. Ranging from 7 - ~80 days, this variance category captures propagating synoptic systems, slow Rossby waves, Madden-Julian variability, and tropospheric "rivers" (Newell et al., 1992),

among other processes. All of these mechanisms are dynamic in nature, and thus the intraseasonal variance category is dominated by the transients in vapor flux convergence.

The thermodynamic *E'* term contains the lowest intraseasonal variance, and cannot be significantly described by the other components of the water cycle over the tropics and most land areas (**Figs. 4.6d-f**). The lack of low-frequency variance in the tropics was also noted in the annual category, but over land this suggests low thermodynamic sensitivity to passing dynamic disturbances. Difficulties in simulating the clouds that accompany these systems and the soil moisture response to rainfall likely contribute to the insignificant values.

C' describes ~100% of the variance in both *P'* and *T'* with very little influence from the other components (**Figs. 4.6a-c,g-i**). For this to occur, the intraseasonal convergence must describe precipitation and vapor flux convergence independently, as otherwise the variance of the convergent term would exceed either component's variance and normalized covariances >100% would result. This suggests that dynamic systems leading to convergence in the intraseasonal band act to either raise the amount of moisture in the atmospheric column or are coincident with precipitation, but rarely do both occur simultaneously. In the intraseasonal band, therefore, there are dual, independent exchange regimes between 1) *C'* and *T'* when the convergent region is unsaturated; and 2) *C'* and *P'* when the convergent region would otherwise exceed saturation. With much smaller variance, intraseasonal *E'* co-varies with a *–C'* term that experiences much larger variance (**Fig. 4.6f**) due to its interactions with the other two water cycle components. By examining **Figs. 4.6k,l,** it becomes clear that evaporation

occurs primarily under the first convergent exchange regime, with evaporation helping to speed the saturation of the atmospheric column.

As the dominant term in the intraseasonal variance category, it is instructive to separate the preferred influence of vapor flux convergence on the other water cycle components. Not surprisingly, the tropical regions that are routinely near saturation show the largest exchange of moisture from convergence to precipitation (**Fig. 4.6j**). These regions are also the center of MJO activity. Monsoon precipitation is often manifested in subseasonal systems, and much of the variance in vapor flux convergence in these regions is explained by coincident precipitation. Over arid regions that rarely ever reach saturation, the intraseasonal *C'* term is explained almost exclusively by *T'* (**Fig. 4.6l**).

The water cycle acts quite consistently between the time scales of the annual and diurnal solar forcing. In fact, the patterns displayed by the intraseasonal band mimic the patterns that are produced when normalized covariances are computed from the components' full (unfiltered) annual time series (not shown). This suggests that the largest percentage of variance is located outside of the narrow bands that define the direct solar forcings, as was observed in RR2007b for *P'* and is also true for *C'* and *T'* (*E'* is dominated by diurnal variance but has a total variance an order of magnitude smaller than *C'* in most areas). Most of the water cycle's variance is therefore best described by the dynamic vapor flux convergence, which exchanges mainly with precipitation (particularly in the tropics and monsoon regions), although also with increases in the precipitable water tendency (especially in areas of large-scale subsidence) and with evaporation (notably over the stratocumulus regions).

4.4 Comparison with PERSIANN Precipitation

To verify that the results of this study are not overly biased by inadequate convective parameterizations or are too sensitive to the residual definition of the convergent term, the above analysis was also conducted with the R2 precipitation replaced by the Precipitation Estimation from Remotely-Sensed Information using Artificial Neural Networks (PERSIANN; see Hsu et al., 1997, and Sorooshian et al., 2000) product. The PERSIANN product is among a group of high-resolution precipitation products that were compared to the R2 in RR2007b, and uses a suite of remotely-sensed products and in-situ observations to drive a precipitation estimation algorithm at 3-hourly resolution and 0.25ºx0.25º resolution between 60ºN/S latitude. In this study, the PERSIANN precipitation values that fully overlap with any given model grid point were averaged into a single value, approximating the R2's horizontal resolution. In addition, grid points were omitted if more than 20% of the PERSIANN values were missing in any single year from 2002-2004, most often due to geosynchronous satellite coverage in the southeast Pacific and over Australia. Ebert et al. (2007) note that high-resolution precipitation products fare better when examining convection and over the oceans, as the interpretation of microwave channels is restricted over land surfaces. RR2007b revealed several differences between the R2 and PERSIANN global precipitation fields, most notably the effects of an overactive convective parameterization. To ensure a consistent water cycle balance, the residual vapor flux convergence was calculated over every 3-hour forecast period using the model

evaporation and precipitable water tendency along with the PERSIANN precipitation rate.

The normalized covariant descriptions of diurnal, annual, and intraseasonal precipitation from the PERSIANN experiment are presented in **Fig. 4.7**. Each row in **Fig. 4.7** may be compared to the top (precipitation) rows in **Figs. 4.4-6** that have the corresponding time scale in the R2 model. The descriptions of PERSIANN annual and intraseasonal precipitation are remarkably similar to the R2 precipitation. The intraseasonal (**Figs. 4.7g-i**) variance is described even more strongly by the dominant dynamic convergence term. Annual precipitation variance (**Figs. 4.7d-f**) displays a strong meridional contrast between the dynamically-controlled tropics and an air mass driven extra-tropics that displays the same west-to-east transition across the ocean basins. Monsoon behavior is very similar, and a signature of a seasonal double ITCZ over the northern edge of the Eastern Pacific cold tongue is also apparent. Overall, the PERSIANN experiment's precipitation is explained by water cycle behaviors that are very similar to those that describe the R2's parameterized precipitation, although several exceptions are noteworthy.

A larger proportion of the globe is insignificant in each of the PERSIANN experiment's variance categories. The PERSIANN product did not capture significant amounts of precipitation over much larger stratocumulus regions in the Southeast Atlantic and Pacific Oceans, and of course does not estimate precipitation polewards of 60º latitude. The land-surface microwave channel effects on the PERSIANN product also reduce the significance of diurnal and annual precipitation over the mid- and high-latitude continents.

The largest differences between the R2 and PERSIANN experiment water cycles are in the diurnal time scale (**Figs. 4.7a-c**). Over the oceans, *C'* still dominates the description of diurnal *P'*, although over the tropics there is a larger contribution from *E'*. The *C'* and *T'* terms are much more important over the land in the PERSIANN experiment, however. *P'* and *E'* are out of phase over much of the tropical land due to a lag between peak early-afternoon evaporation and convective systems that reach their maximum intensity later in the afternoon and early evening.

The nocturnal convective maximum over the United States Midwest identified by Wallace (1975) has long been an intriguing diurnal phenomenon. The diurnal water cycle behaviors produced by the PERSIANN experiment in this region capture much of the observed variability discussed more extensively in RR2007a. Carbone et al. (2002) tracked propagating convective disturbances from their late-afternoon origins over the lee side of the Rocky Mountains to their dissipation in the early morning over the Great Lakes region, replenished by moisture supplied by a nocturnal low-level jet streaming north from the Gulf of Mexico (Higgins, 1997). The evolution of these processes may be inferred from the normalized covariances shown in **Figs. 4.7a-c**. Precipitation over the lee side of the Rocky Mountains varies nearly in phase with evaporation (**Fig. 4.7a**), indicating an early afternoon initiation of convection. These phases then grow further apart as the storms propagate eastward, until *P'* is ~100% out of phase with *E'* over the Upper Midwest, indicating that convection peaks shortly after midnight. This explanation is also supported by the normalized covariance of *T'* to *P'* (**Fig. 4.7b**). Over the Rockies, these storms occur when there is normally a positive tendency in precipitable water due to afternoon evaporative input, but as precipitation moves

eastward it begins to feed off the supply of moisture already in the atmospheric column at the end of the day. These storms also co-vary with a large influx of convective moisture (**Fig. 4.7c**) that extends from the Texas coast into southern Canada and seems to remain in phase with the precipitation bands throughout the entire process.

Additional comparisons were also made with the Experimental Climate Prediction Center's Seasonal Forecast Model reanalysis (SFM, see Kanamitsu et al., 2002a, and RR2007a,b; not shown). While many of the R2's features discussed above were common to the SFM, the SFM displayed far lower diurnal significance in the description of precipitation's variance over land in the extra-tropics. Variations in the SFM's annual *C'* described virtually all of the *ET'* variance, suggesting a dynamic tendency interaction as opposed to a largely thermodynamic interaction in the R2.

4.5 Conclusions

Examination of the transient balance of the atmospheric water cycle in the NCEP/DOE Reanalysis-2 reveals unique water cycle behaviors at different time scales. The variance of each water cycle process is explained by its normalized covariance with the other components, which then allows a complete description of the dominant balances and exchanges of the water cycle across the globe.

The diurnal water cycle is characterized by a strong land/sea contrast, with thermodynamic evaporation dominating the continents and dynamic convergence controlling exchanges over the ocean. Some diurnal convective regimes are also fed by moisture convergence that corresponds to diurnal circulation patterns (particularly along

tropical coastlines). Although it is largely insignificant at annual and longer time scales, variance in the precipitable water tendency is important over both land and sea.

Annual water cycle behaviors are largely dependent on latitude, with the Hadley Circulation dominating the tropics and the extra-tropics governed by a slow drying and moistening of air masses advected in the westerlies. Monsoon circulations over Southern and Southeastern Asia are strongly influenced by long-distance moisture supply that leads to vapor convergence over land. Evaporation in most of the tropics does not vary significantly on this time scale.

Without a direct solar forcing, the intraseasonal variance category is dominated by propagating convergence regions associated with dynamic systems. The exchange of moisture from these systems is dependent on the relative humidity of the convergent environment, with moisture convergence variability corresponding to an increase in the relative humidity in unsaturated regions and precipitation when the environment is saturated. The intraseasonal behaviors also mimic the normalized covariances of the unfiltered time series, suggesting that the largest portion of variance in the water cycle falls outside the direct solar frequencies.

Water cycle behaviors produced describing the variance of precipitation were robust when PERSIANN precipitation replaced the modeled fields (particularly on the intraseasonal and annual time scales), although large portions of the continents become insignificant, due perhaps in part to errors introduced by satellite data over land. The water cycle behaviors that control the intriguing nocturnal precipitation maximum over the US Midwest are captured when PERSIANN data are introduced, displaying the

signature of afternoon thunderstorms over the Rocky Mountains that are supplied with moisture by a low-level jet as they propagate eastward until the early morning.

As a compliment to RR2007b, the results presented here explored the covariant behaviors of unique water cycle features in much greater detail. Still further examinations are possible by focusing on a single time scale and tracking the evolution of individual bandpass-filtered structures. Preliminary examinations of the surface water cycle and the surface and atmospheric energy cycle using these methods have also proven interesting. The sensitivity of the atmospheric water cycle's transient behaviors to a model's physical parameterizations could shed some light on the relative strengths and weaknesses of the model's parameterization set.

4.6 Acknowledgements

The text of this chapter, in full, is accepted for the "Understanding Diurnal Variability of Precipitation through Observations and Models" special issue of the *Journal of Climate* by A.C. Ruane and J.O. Roads. The dissertation author was the primary investigator and author of this paper, and the publication's coauthor made significant contributions to the direction of the research examined in this chapter. We are grateful for the support received through NOAA NA17RJ1231 and NASA NNG05GR40G and NNG06GC85G grants. The views expressed herein are those of the authors and do not necessarily reflect the views of NOAA and NASA. We would also like to thank Masao Kanamitsu for his advice on the R2, Martin Olivera, Jack Ritchie, and Patrick Tripp for technical support, and three reviewers for their helpful comments.

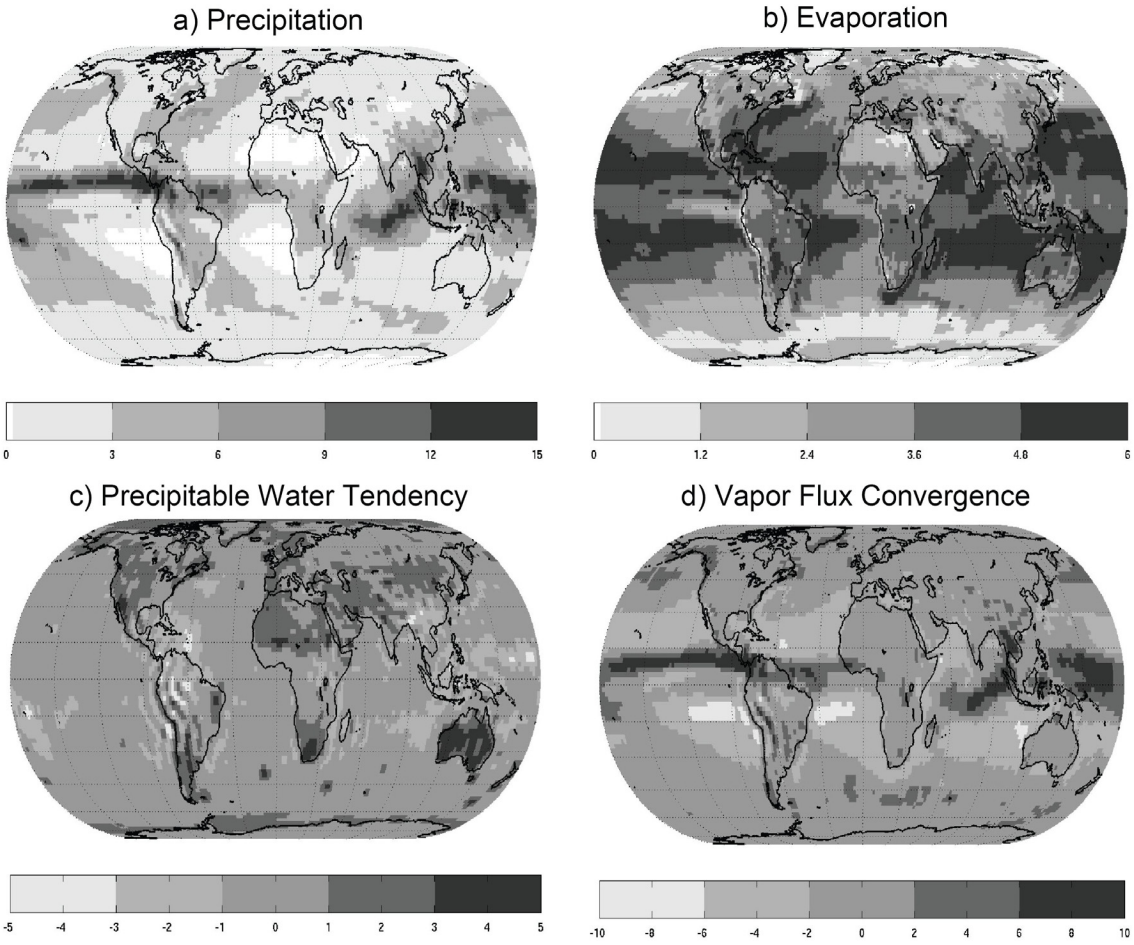

Figure 4.1: 2002-2004 water cycle component means (mm/day). *(a)* Precipitation, *(b)* evaporation, *(c)* precipitable water tendency, *(d)* vapor flux convergence.

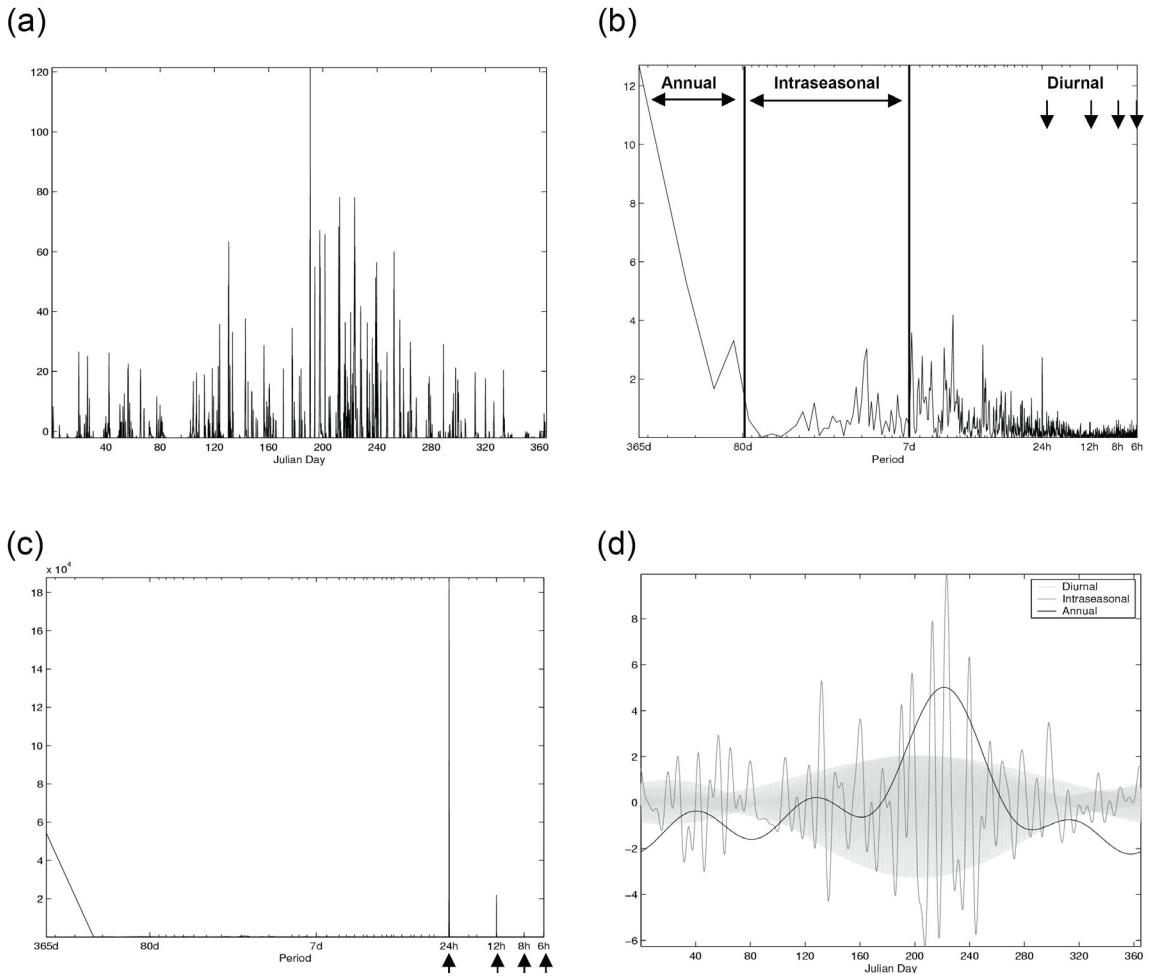

Figure 4.2: Methodology example for Lindenberg, Germany, in 2002; *(a)* 3-hourly precipitation rate (mm/day; deviation from the mean); *(b)* variance spectrum of precipitation rate ([mm/day]2) with variance category definitions; *(c)* variance spectrum of surface downward shortwave radiation flux ([W/m2]2) with 4 diurnally forced peaks; *(d)* bandpass-filtered time series of precipitation for each variance category (mm/day). The diurnal category oscillates so rapidly that it appears to blend together into an envelope here.

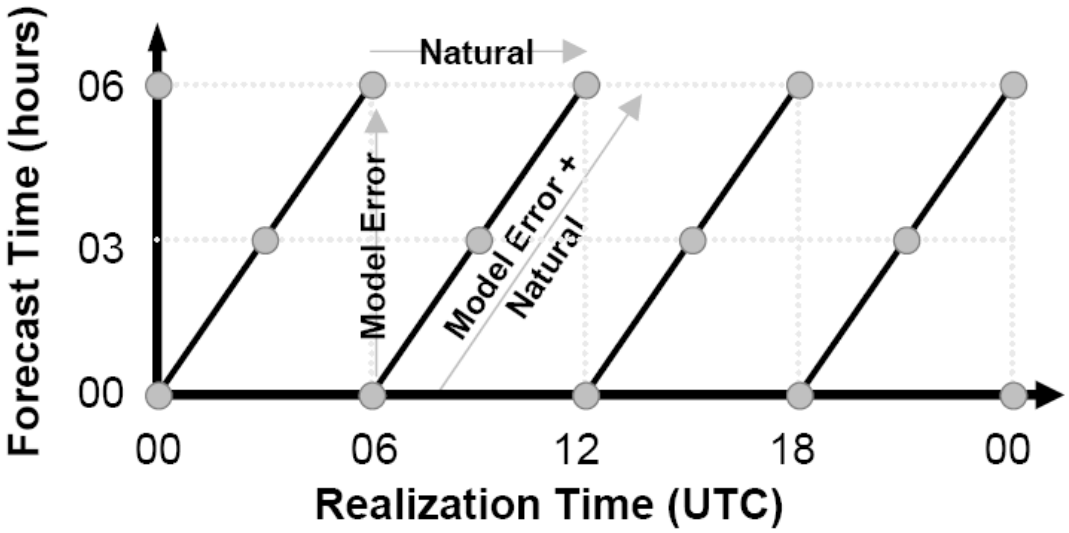

Figure 4.3: Experiment design overview. Each diagonal line represents a continuous simulation, and each circle represents an output time. The gray arrows indicate the differences that separate the model error and natural precipitable water tendencies.

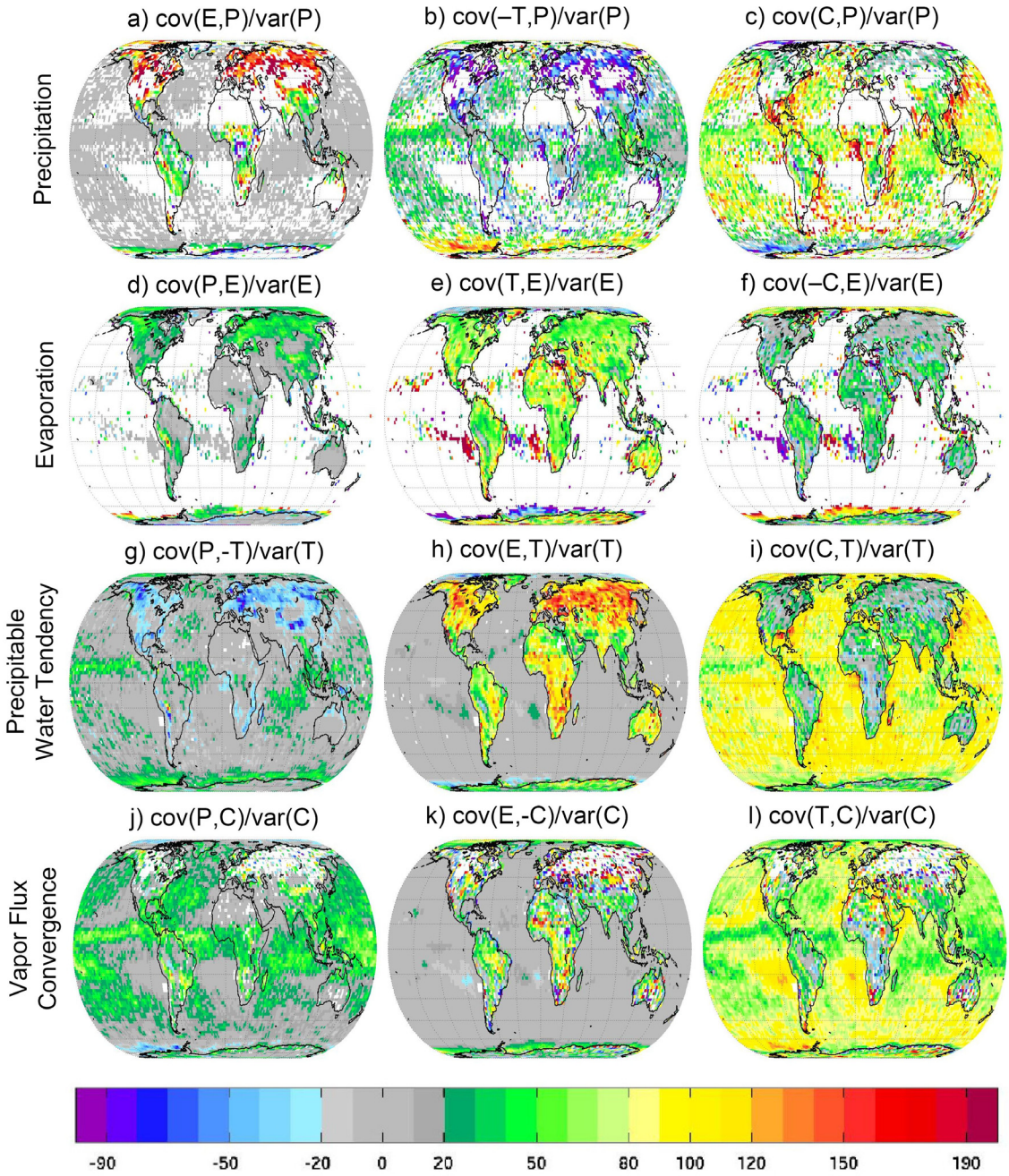

Figure 4.4: Diurnal normalized covariance maps describing diurnal variance (%) from 2002-2004 in the R2. The sum of each row describes 100% of the diurnal variance of the component listed at left by its normalized covariance with the other components. The first row (panels *a-c*) represents the three terms in the center of *Eqn. 4.9a*; likewise panels *d-f* represent the terms in *Eqn. 4.9b*, panels *g-i* represent theh terms in *Eqn. 4.9c*, and panels *j-l* represent the terms in *Eqn. 4.9d*. White grid points represent locations where the variance description was insignificant.

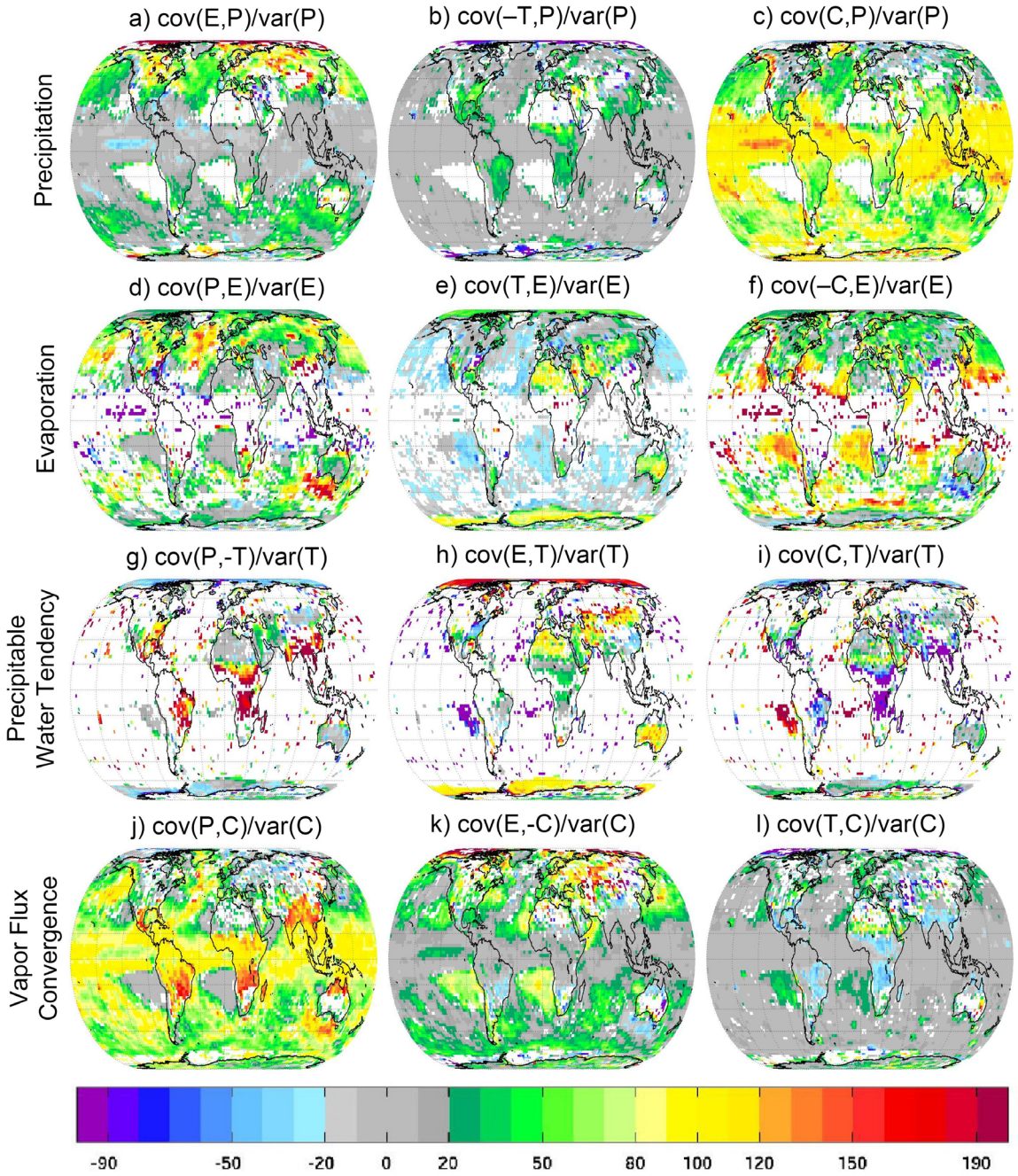

Figure 4.5: As in Fig. 4.4, but for annual variance.

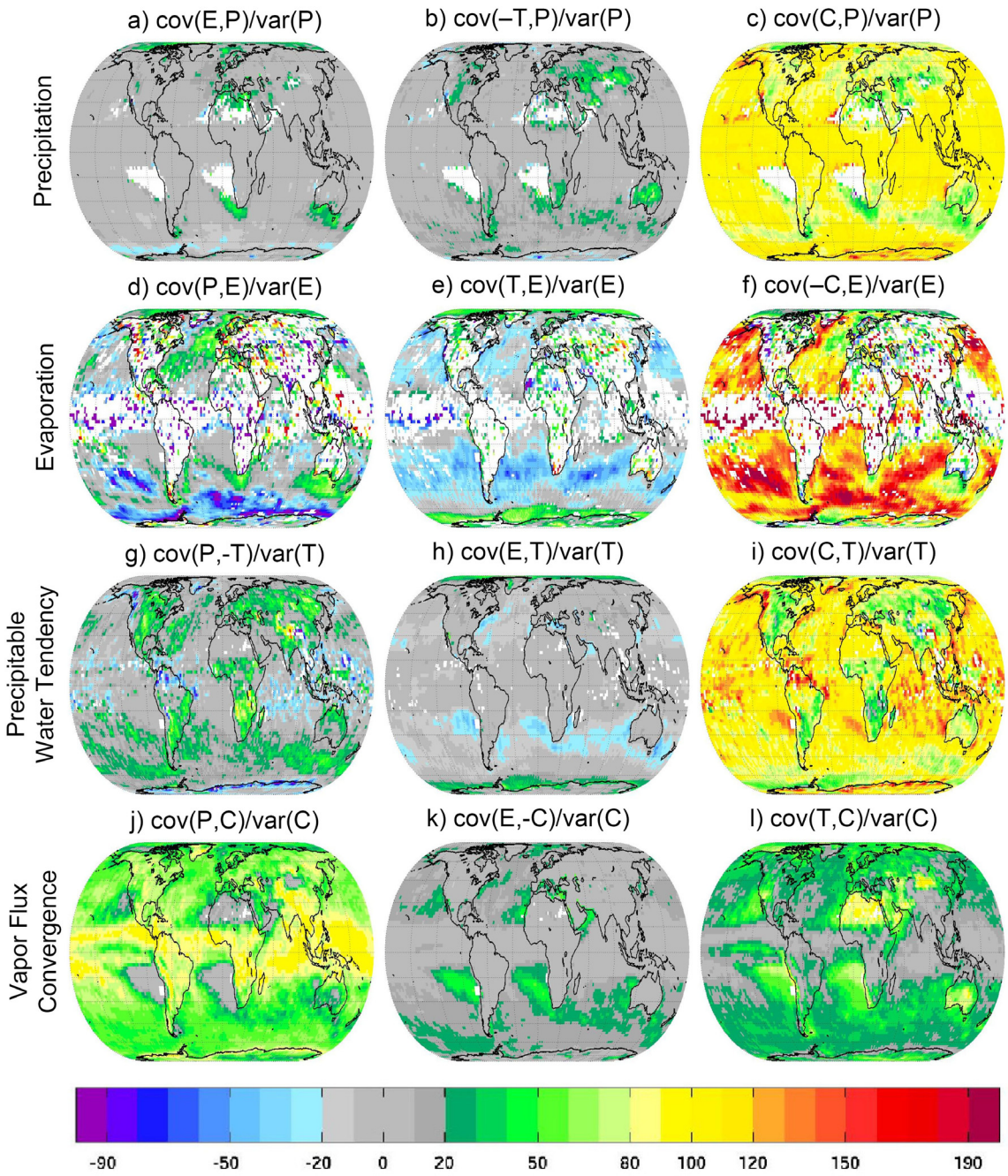

Figure 4.6: As in Fig. 4.4, but for intraseasonal variance.

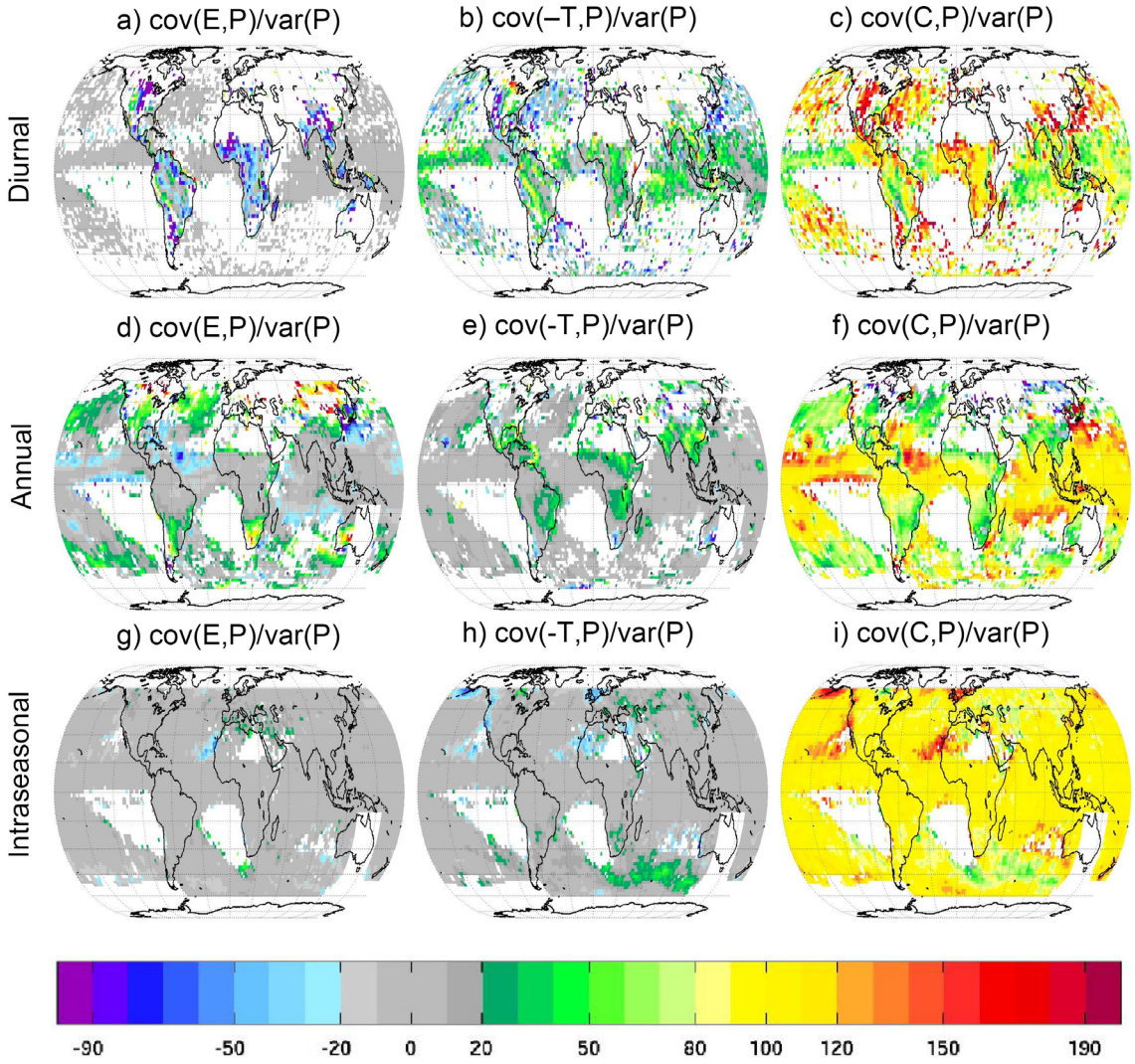

Figure 4.7: As in Fig. 4.4, but for only the precipitation variance description in the PERSIANN experiment. Here each row corresponds to *Eqn. 4.9a*, but at the time scale indicated on the left. Panels *a-c* represent diurnal variance, panels *d-f* annual variance, and panels *g-i* intraseasonal variance.

CHAPTER V

Summary and Future Work

5.1 Summary of Results

A variety of modeling and observational products were evaluated with the purpose of identifying unique aspects in the atmospheric water cycle ranging from the diurnal to annual frequencies. This was done in three parts, each utilizing a novel methodology and each corresponding to a chapter here.

First, the diurnal variation of water and energy, both at the surface and in the atmospheric column, was examined independent of other frequencies in Chapter 2. Drawing from the NCEP/DOE Reanalysis-2 and a new Seasonal Forecast Model (SFM) reanalysis that were produced for the Coordinated Enhanced Observing Period (CEOP), diurnal and semidiurnal harmonics from the summertime Global Spectral Model output from 2001-2003 was compared to the NCEP North American Regional Reanlaysis (NARR) over the Continental United States.

In comparison to the NARR results, which featured increased data assimilation at a higher resolution, the global reanalyses showed mixed success in reproducing the unique diurnal variations observed across the continent. Water and energy components that are sensitive to thermodynamic forcings exhibited very similar phase regardless of horizontal resolution or land-surface scheme, but a large discrepancy in the amplitude of diurnal latent and sensible heating was noted between the OSU2 and NOAH schemes, although these complimentary biases offset and led to a similar net energy budget. Despite energetic forcings that were quite similar to the regional reanalysis, the global

reanalyses produced very different water cycles, indicating a much larger role for dynamic and parameterized influences.

The global reanalyses' diurnal atmospheric water cycle is permeated with biases that stem from a suite of parameterizations that lead to an overactive convective trigger. Despite significant differences in land cover and orography and a well-observed nocturnal precipitation maximum in the upper Midwest, global reanalyses have low significance and a consistent afternoon peak in daily rainfall. The reanalysis system actually performs quite well in representing the dynamic vapor convergence and the precipitable water tendencies, capturing a nocturnal low-level jet which supplies moisture to the upper Midwest. Without the evening thunderstorms, however, this moisture input leads to large diurnal fluctuations in the atmospheric reservoir of vapor.

Second, the comprehensive distribution of precipitation's variance between the diurnal and annual frequencies was evaluated in Chapter 3. Comparisons between atmospheric reanalyses and the first spectral intercomparison of High Resolution Precipitation Products show that precipitation has a red spectrum, but displays unique characteristics in both time and space. Diurnal variance is strongest in the tropics, along coastlines, and on the edge of mountain ranges. Annual variance is concentrated just off the equator in the tropics and helps identify monsoon regions. The patterns of the low-frequency intraseasonal and slow synoptic variance categories indicate that large-scale circulation patterns set environmental conditions to encourage or inhibit precipitation on faster time scales, with the Hadley circulation and Madden-Julian oscillation especially notable. The fast-synoptic and high-frequency categories feature a strong land-sea contrast, with ocean systems organizing on the fast synoptic scale and land systems

demonstrating the large influence of surface gradients in temperature, orography, land cover, and humidity, and other factors.

The Relaxed Arakawa-Schubert convective parameterization (employed by the SFM reanalysis) shifts large portions of the variance from the higher-frequency categories toward the low-frequency portions of the precipitation spectrum. This enhancement of long-period activity may be beneficial for studies at seasonal and longer time scales, but comes at the expense of realistic sub-seasonal simulation. The Reanalysis-2 reproduces many of the unique patterns that were documented in the observation-based estimates, however. The variance of precipitation is therefore found to be quite sensitive to the suite of parameterizations utilized by a reanalysis system, which may have a profound impact on the water cycle across scales.

Third, after analyzing a specific time scale (in Chapter 2) and a specific component (in Chapter 3), Chapter 4 evaluated the interactions between all atmospheric water cycle components at various time scales. A unique method that comprehensively describes the variance of any water cycle component through its covariance with the other water cycle components reveals that the balances and exchanges of moisture throughout the water cycle are often native to a particular time scale and region. The diurnal cycle is characterized by the differing heat capacities of the land and ocean surface, while the annual solar signal drives unique latitudinal features in response to stronger seasonality at the higher latitudes. The hydroclimate outside of these forced time scales is dominated by moisture convergence and divergence in propagating systems.

The diurnal water cycle is dominated by a strong thermodynamic response to the

sun. Evaporation and a destabilizing atmosphere lead to enhanced afternoon convection on many days, but the regular evaporative signal also drives large fluctuations in the precipitable water reservoir. Dynamical processes play a diminished role over the high-latitude continents, but in the Tropics and over the oceans vapor convergence fills the void caused by relatively low daily thermal ranges. Annual variance in the tropics is dominated by the large-scale Hadley convergence. Outside of the tropics the water cycle is characterized by the modification of large-scale air masses as they are advected by the westerlies. Continental air masses demonstrate a strong thermodynamic connection between evaporation and precipitation, while marine air masses are governed by dynamic processes. Air masses adjust their properties over a transition region that extends several hundred kilometers downwind from the coastlines. Without a direct solar forcing, intraseasonal vapor convergence dominates variability, raising the relative humidity at the level of convergence or initiating precipitation after the saturation has been reached.

This dissertation has thus revealed many interesting processes that govern the regional variability of the atmospheric water cycle across many temporal scales. The water cycle is controlled by distinct dynamic and thermodynamic processes that are largely determined by the interaction of external forcing and the surface boundary. In the absence of strong solar variation or when the surface's high heat capacity buffers the thermodynamic signal, transient dynamical systems dominate. The reanalysis systems perform admirably in capturing the affects of large-scale circulations on environmental conditions, interacting with local signals across many time scales. Simulated biases most often originate in the convective parameterizations, although several parameterized

steps initiate the convection scheme. Designed primarily to capture low-frequency variation, these pay a heavy statistical price in their ability to model higher frequencies.

Each dissertation chapter also demonstrates methods that could be extended to evaluate regional features in greater detail due to their comprehensive nature. In particular, the complete water and energy budget harmonics calculated over North America extend our ability to track processes in the complex evolution of a forced response. The exhaustive description of variance from modeled and observation-based precipitation sets reveals the time scales and regions that play the most important role in understanding precipitation. Finally, the complete description of water cycle variance through each component's normalized covariances describes the major interactions that drive moisture exchange across many scales. Each of these methodologies could be utilized for other variables and balances, as well as in different regions or time scales.

5.2. Ongoing Work

Ongoing extensions of this dissertation are already underway. The first of these (Ruane and Roads, 2007d) examines the sensitivity of the atmospheric water cycle to convective and land-surface parameterizations. For this purpose, four combinations of two convective schemes and two land-surface schemes were initialized from the initial reanalysis conditions of January 1st, 2000 (reanalyses were selected to maintain consistent surface modeling systems). To prevent spin-up influences the first year is excluded, but six continuous years of global, three-hourly output are available from 2001-2006 for intercomparisons of the 4 parameterization combinations. To test the ability of these models to make stand-alone forecasts unconstrained by assimilated

observations, these experiments are also comparable to the reanalysis evaluations in Ruane and Roads, 2007a,b,c.

Preliminary results indicate that the atmospheric water cycle is much more sensitive to the convective parameterization than it is to the land-surface scheme (not shown). In addition to shifting large portions of the tropical high-frequency precipitation variance to lower frequencies, the Relaxed Arakawa-Schubert parameterization bias similarly affects the variance distribution of precipitable water tendency and vapor flux convergence. Evaporation is the only atmospheric water cycle component that does not feature a clearly red spectrum, as the solar forcings produce dominant annual and diurnal peaks.

Many of the water cycle features that were captured quite nicely by the reanalyses are also found in the stand-alone experiments (not shown). These robust features include the signatures of the Hadley circulation, monsoon systems, stratocumulus regions, arid regimes, coastal and mountain circulations, and significant land/sea contrasts. Despite the reddened redistribution of variance in the water cycle, dominant component interactions are largely conserved regardless of convective and land-surface scheme combinations.

In comparison to the observationally-constrained reanalyses, the free-running experiments alter the water cycle in several notable ways. In the reanalyses, the South American diurnal cycle is dominated by thermodynamic evaporation which mostly drives a positive precipitable water tendency (as it does over the other continents). Without assimilated observations, the boundary layer over the Amazon becomes saturated and evaporated moisture corresponds directly to vapor divergence or precipitation events.

In addition, diurnal vapor convergence plays a larger role over the continents and diurnal precipitation variance is much less significant. The free annual variation of precipitable water is negligible, confirming the separation of model and natural tendencies in Chapter 4. Intraseasonal evaporation covaries with passing precipitation variability depending on the choice of land-surface schemes, but the interaction of rainfall with the other water cycle components at this time scale is insensitive to the enhanced activity produced by the Relaxed Arakawa-Schubert scheme.

5.3. Future Plans

These dissertation results suggest many potential applications. These bandpass-filtered datasets could be further examined to isolate the exact dynamic influences that govern a particular region's water cycle at different scales, as well as identify lagged responses. After the water cycle has been characterized at a particular location across these time scales, the anomalous balances and exchanges that accompany abnormal events could be isolated and incorporated into future forecasts.

Extensions of these methodologies are also possible. Similar studies examining interannual time scales may help reveal the processes that lead to hydroclimatologic teleconnections, and three-dimensional balances could also be evaluated to reveal variability in atmospheric structure (see e.g. Anderson et al., 2007). The methodologies developed in Chapters 3 and 4 could also be used to elucidate the variance of the other balances in Chapter 2 (surface water, surface energy, and atmospheric energy). Of course, these techniques may be utilized to examine other modeling systems and will ideally be applicable to developing observation sets.

Appendix 1

ECPC Contributions to CEOP

Considerable time and energy went into the generation and maintenance of model datasets for this dissertation which are fully available through the Coordinated Energy and Water Cycle Experiment (CEOP, originally called the Coordinated Enhanced Observing Period) database located at the Max-Planck-Institute für Meteorologie (MPI). The Scripps Institution of Oceanography's Experimental Climate Prediction Center (ECPC) works in collaboration with the National Centers for Environmental Prediction (NCEP) to analyze and develop their global and regional atmospheric models. In particular, ECPC is currently using both the NCEP/DOE Reanalysis-2 model (R2; Kanamitsu et al. 2002b) and the NCEP seasonal forecast model (SFM; Kanamitsu et al. 2002a) to provide model output for CEOP. Details of these modeling systems were presented in **Table 2.1**.

The output from these two models include analysis files (ft00), and forecast files every 3hours (ft03 and ft06) from short-range 6-hour forecasts initialized every 6 hours (00, 06, 12, 18 UTC). In addition, every 24 hours (at 12 UTC), the 6 hour forecast is extended to 36 hours at 3-hourly resolution, as is demonstrated in **Figure A.1.** Note that this output schedule enables many comparisons between overlapping forecast times that correspond to the same realization time, and also that time series of individual forecast times enable spin-up examinations and analysis increments.

Table A.1 details the important water and energy cycle variables that were provided to the CEOP archive at MPI. These include both original and post-processed

quantities, the latter derived from the spectral components of state variables at their model coordinates. These variables are included in the global GRIB files described below, and are the sole variables included in the Model Output Location Time Series (MOLTS) files, which contain only the grid point corresponding to the CEOP observation sites around the world (see **Table A.2**).

Raw ECPC output files (ft00, ft03, ft06, …, ft33, ft36) provided to MPI:

PGB (2.5 degree 144x73x17 grid linear grid with p-levels) ~2 MB (GRIB)

- Multiple atmospheric variables on 17 p-levels (1000,925,850,700,600,500,400,300,250,200,150,100,70,50,30,20,10 hPa)

FLX (T62, on 192x94 gaussian grid) ~2 MB (GRIB)

- Surface fluxes, precipitation, land parameters

DIV (L28T62, on 192x94x28 gausian grid with σ-levels. ft03+ only) ~5 MB (GRIB)

- Heating diagnostics converted to mass-weighted variables.
- Vertical integrals of heating profiles.

SGB (L28T62, on 192x94x28 gaussian grid with σ-levels) ~18 MB (GRIB)

- Gridded atmospheric variables and diagnostics on 28 σ-levels

ECP (L28T62, on 192x94x28 gaussian grid with σ-levels) ~15 MB (GRIB)

- Gridded atmospheric variables and dynamical processes (moisture, moisture flux, convergence, energy flux, etc.)
- 3-D mass-weighted variables and vertical integrals on 28 σ-levels.

MOLTS (41 stations x 28 layers) 0.4 MB (NetCDF)

- Contains only the variables in **Table A.1**, processed from PGB, FLX, DIV, DIA, SGB, SFB, ECP files after the forecast.
- There are 41 columns corresponding to the 41 CEOP observation sites (**Table A.2**) and 111 CEOP variables (**Table A.1**). Note that some variables differ in dimensionality and grid spacing.

Auxiliary files, stored locally at ECPC (but not submitted to CEOP via MPI) include

SIG (L28T62) 3.5 MB, binary

- Atmospheric forecast variables (spectral)

SFC (T62) 3.6 MB, binary

- Land surface forecast variables (grid-point)

Among modeling participants to date, ECPC has contributed the largest volume (more than 45%) of model output to the CEOP archive at MPI (see **Table A.3**, updated from Toussaint et al., 2007, with permission from Hans Luthardt). ECPC output spans the entire CEOP phase I period, and is ahead of the pack in its conversion of MOLTS files to Network Common Data Format (NetCDF) format. This output is freely available via www.ceop.net.

Table A.1: ECPC CEOP variables and processes for the top of the atmosphere, the atmosphere, the surface and subsurface, along with their units. Accumulated variables represent a period covering the previous 3 hours, while instantaneous variables are snapshots at the forecast time (accumulated variables at ft00 are not recommended for use). The raw output file in which each variable is located is provided, along with the PDS numbers that correspond to the variable in the ECPC grib tables. Finally, the short name of each variable in the MOLTS NetCDF output is presented (note that a data point showing -99 is an error/missing value in the MOLTS file).

Variable ID	Full Variable Description	Units	Accumulated or Instantaneous	Raw Files	GRIB PDS5 Number	GRIB PDS6 Number	MOLTS Name
	Miscellaneous						
1	Elevation	m	Instantaneous	SGB	7	1	hgt
2	Surface albedo	%	Instantaneous	FLX	84	1	albdo
3	Land/sea mask (land=1, sea=0)	Binary	Instantaneous	FLX	81	1	land
4	Ice concentration (ice=1,no ice=0)	Binary	Instantaneous	FLX	91	1	icec
5	Total cloud cover	%	Instantaneous	FLX	71	200	tcdc
6	Roughness length	m	Instantaneous	FLX	83	1	sfcr
7	Vegetation cover	%	Instantaneous	SFB	87	1	veg
	Top of Atmosphere Processes						
8	Shortwave downward flux (positive)	W/m^2	Accumulated	FLX	204	8	dswrftoa
9	Shortwave upward flux (positive)	W/m^2	Accumulated	FLX	211	8	uswrftoa
10	Longwave upward flux (positive)	W/m^2	Accumulated	FLX	212	8	ulwrftoa
	Vertically Integrated Atmos Variables						
11	Total moisture (precipitable water) Q	cm	Accumulated	FLX	54	200	pwat
11b	Total moisture (precipitable water) Q	kg/m^2	Instantaneous	ECP	54	200	pwatb
12	Kinetic energy	kg/s^2	Instantaneous	ECP	154	200	kei
13	Geopotential energy (gZ)	kg/s^2	Instantaneous	SGB	142	10	gzi
14	Enthalpy (CpT)	kg/s^2	Instantaneous	SGB	187	10	cpti
14b	Enthalpy (CpT)	kg/s^2	Instantaneous	ECP	187	200	cptib
15	Phis (phi-RTv)d(ps/g)/dt	kg/s^2	Instantaneous	ECP	197	200	phisi
16	Total energy (CpT+KE+phis)	kg/s^2	Instantaneous	ECP	143	200	enti
17	Total mass = ps/g	kg/m^2	Instantaneous	ECP	180	200	mass
18	Surface pressure	Pa	Instantaneous	SGB	1	1	pres
	Vertically Integrated Processes						
19	Deep convective latent heating rate	W/m^2	Accumulated	DIV	100	200	cnvlhri
20	Shallow convective latent heating rate	W/m^2	Accumulated	DIV	101	200	shalhri
21	Stable latent heating rate	W/m^2	Accumulated	DIV	102	200	lrghri
22	Deep convective moistening rate	$kg/m^2/s$	Accumulated	DIV	103	200	cnvmri
23	Shallow convective moistening rate	$kg/m^2/s$	Accumulated	DIV	104	200	shamri
24	Stable moistening rate	$-kg/m^2/s$	Accumulated	DIV	105	200	lrgmri
25	Turbulent moistening rate	$kg/(m^2s)$	Accumulated	DIV	240	200	vdfmri
26	Turbulent heating rate	W/m^2	Accumulated	DIV	159	200	vdfhri
27	Shortwave heating rate	W/m^2	Accumulated	DIV	209	200	swhri
28	Longwave heating rate	W/m^2	Accumulated	DIV	210	200	lwhri
29	Precipitation rate	$kg/m^2/s$	Accumulated	FLX	59	1	prate
30	Convective precipitation rate	$kg/m^2/s$	Accumulated	FLX	214	1	Cprat
31	Precipitation (snow) rate	$kg/m^2/s$	Accumulated	FLX	64	1	Srweq
32	Water vapor zonal flux	kg/m/s	Instantaneous	ECP	106	200	wvzfxi
33	Water vapor meridional flux	kg/m/s	Instantaneous	ECP	107	200	wvmfxi
34	Water vapor flux divergence	$kg/m^2/s$	Instantaneous	SGB	108	10	wvfxdi
34b	Water vapor flux divergence	$kg/m^2/s$	Instantaneous	ECP	108	200	wvfxdib

35	Kinetic energy flux divergence	W/m^2	Instantaneous	ECP	140	200	kefxdi
36	Geopotential height flux divergence	1/s	Instantaneous	SGB	110	10	gzfxdi
36b	Mass weighted geopotential height flux divergence	W/m^2	Instantaneous	ECP	32	200	mgzfxdi
37	Enthalpy flux divergence	gm/s^3	Instantaneous	SGB	189	10	cptfxdi
37b	Mass weighted enthalpy flux divergence	W/m^2	Instantaneous	ECP	31	200	mcptfxdi
38	Total energy flux div. (CpT+gz+KE)	W/m^2	Instantaneous	ECP	213	200	entfxdi
39	Mass flux divergence	$kg/m^2/s$	Instantaneous	ECP	141	200	msfxdi
	Surface Variables						
40	Surface skin temperature	K	Instantaneous	FLX	11	1	tmpskin
41	2-meter temperature	K	Instantaneous	FLX	11	105	tmp2m
42	2-meter specific humidity	kg/kg	Instantaneous	FLX	51	105	spfh2m
43	U-component at 10 m	m/s	Instantaneous	FLX	33	105	ugrd10m
44	V-component at 10 m	m/s	Instantaneous	FLX	34	105	vgrd10m
45	Snow water equivalent	Kg/m^2	Instantaneous	FLX	65	1	weasd
46	Vegetation water	Kg/m^2	Instantaneous	FLX	223	1	cnwat
47	Planetary boundary layer height	m	Instantaneous	FLX	221	1	hpbl
	Surface Processes						
48	Shortwave downward flux (positive number)	W/m^2	Accumulated	FLX	204	1	dswrf
49	Shortwave upward flux (positive number)	W/m^2	Accumulated	FLX	211	1	uswrf
50	Longwave downward flux (positive number)	W/m^2	Accumulated	FLX	205	1	dlwrf
51	Longwave upward flux (positive number)	W/m^2	Accumulated	FLX	212	1	ulwrf
52	Sensible heating = Total turbulent heating (positive upward)	W/m^2	Accumulated	FLX	122	1	shtfl
53	Latent heating = Total turbulent latent heating (positive upward)	W/m^2	Accumulated	FLX	121	1	lhtfl
54	Snowmelt heat flux	W/m^2	Accumulated	FLX	229	1	snohf
55	Surface runoff plus layer runoff minus base flow	$kg/m^2/s$	Accumulated	FLX	90	1	runof
56	Baseflow runoff	$kg/m^2/s$	Accumulated	FLX	234	1	bgrun
	Bottom of Subsurface Processes						
58	Ground heat flux	W/m^2	Accumulated	FLX	155	1	gflux
	Atmosphere Variables						
59	Temperature	K	Instantaneous	PGB	11	100	tmp
59b	Temperature	K	Instantaneous	SGB	11	107	tmpb
60	Moisture	kg/kg	Instantaneous	PGB	51	100	spfh
60b	Mass weighted moisture	kg/m^2	Instantaneous	ECP	50	107	mspfh
60c	Moisture	kg/kg	Instantaneous	SGB	51	107	spfhc
61	Zonal wind	m/s	Instantaneous	PGB	33	100	ugrd
61b	Zonal wind	m/s	Instantaneous	SGB	33	107	ugrdb
62	Meridional wind	m/s	Instantaneous	PGB	34	100	vgrd
62b	Meridional wind	m/s	Instantaneous	SGB	34	107	vgrdb
63	Geopotential height	m^2/s^2	Instantaneous	PGB	7	100	gp
64	Pressure velocity	Pa/s	Instantaneous	PGB	39	100	vvel
64b	Pressure velocity	Pa/s	Instantaneous	ECP	39	107	vvelb
64c	Pressure velocity	Pa/s	Instantaneous	SGB	39	107	vvelc
65	Mass weighted kinetic energy	J/m^2	Instantaneous	ECP	68	107	ke
66	Mass weighted Enthalpy	J/m^2	Instantaneous	ECP	69	107	cpt
67	Geopotential Energy	J/m^2	Instantaneous	SGB	70	107	gz
68	Total Mass weighted Energy (CpT+KE+phis)	J/m^2	Instantaneous	ECP	219	107	ent

	Atmosphere Processes 3D						
69	Deep convective latent heating rate	W/m^2	Accumulated	DIV	242	107	cnvhr
70	Shallow convective heating rate	W/m^2	Accumulated	DIV	244	107	shahr
71	Stable latent heating rate	W/m^2	Accumulated	DIV	241	107	lrghr
72	Deep convective moistening rate	$kg/m^2/s$	Accumulated	DIV	243	107	cnvmr
73	Shallow convective moistening rate	$kg/m^2/s$	Accumulated	DIV	245	107	shamr
74	Stable moistening rate	$-kg/m^2/s$	Accumulated	DIV	236	107	lrgmr
75	Turbulent moistening rate	$kg/m^2/s$	Accumulated	DIV	249	107	vdfmr
76	Turbulent heating rate	W/m^2	Accumulated	DIV	246	107	vdfhr
77	Shortwave heating rate	W/m^2	Accumulated	DIV	250	107	swhr
78	Longwave heating rate	W/m^2	Accumulated	DIV	251	107	lwhr
79	Water vapor zonal flux	kg/m/s	Instantaneous	ECP	173	107	wvzfx
80	Water vapor meridional flux	kg/m/s	Instantaneous	ECP	174	107	wvmfx
81	Water vapor vertical flux	kg/m/s	Instantaneous	ECP	199	107	wvvfx
82	Water vapor flux divergence	$kg/m^2/s$	Accumulated	SGB	200	107	wvfxdv
82b	Water vapor flux divergence	$kg/m^2/s$	Instantaneous	ECP	200	107	wvfxdvb
83	Kinetic energy flux divergence	W/m^2	Instantaneous	ECP	201	107	kefxdv
84	Geopotential height flux divergence (gZ)	W/m^2	Instantaneous	SGB	29	107	gzfxd
84b	Geopotential height flux divergence (gZ)	W/m^2	Instantaneous	ECP	29	107	gzfxdb
85	Enthalpy flux divergence (CpT)	W/m^2	Instantaneous	SGB	30	107	cptfxd
85b	Enthalpy flux divergence (CpT)	W/m^2	Instantaneous	ECP	30	107	cptfxdb
86	Total energy flux div. (CpT+gZ+KE)	W/m^2	Instantaneous	ECP	203	107	entfxd
87	Mass flux divergence	$kg/m^2/s$	Instantaneous	ECP	202	107	msfxdv
	Subsurface Variables 3D						
88	Soil moisture - Top Layer	%	Instantaneous	FLX	144	112	soilw10
89	Soil moisture - Bottom Layer	%	Instantaneous	FLX	144	112	soilw200
90	Temperature - Top Layer	K	Instantaneous	FLX	11	112	tmp10
91	Temperature - Bottom Layer	K	Instantaneous	FLX	11	112	tmp200
	Extra variables						
92	Snow sublimation heat flux	W/m^2	Accumulated	FLX	230	1	snoev
93	Phis (phi-RTv)d(ps/g)/dt	W/m^2	Instantaneous	ECP	222	107	phis
	NOAH Only variables						
94	Soil moisture - 2^{nd} Layer	%	Instantaneous	FLX	144	112	soilw40
95	Soil moisture - 3^{rd} Layer	%	Instantaneous	FLX	144	112	soilw100
96	Temperature - 2^{nd} Layer	K	Instantaneous	FLX	11	112	tmp40
97	Temperature - 3^{rd} Layer	K	Instantaneous	FLX	11	112	tmp100

Table A.2: MOLTS location characteristics. Soil type based on 12 soil types; vegetation type based on 12 vegetation types. The vegetation type, roughness, grid points, and elevation are the same for RII and SFM, but RII uses a fixed soil type 7, and a fixed vegetation cover of .7 for all land points. Vegetation cover is provided to SFM by a monthly climatology.

Site	Site Name	Longitude	Latitude	Elevation (m)	Roughness Length (m)	Soil Type	Soil Type Description	Vegetation Type	Vegetation Type Description
1	Lindenberg	14.12	52.17	50.6	0.554	2	Loamy sand	1	Mixed farming, tall grassland
2	Cabauw	4.93	51.97	12.4	0.5	2	Loamy sand	3	Short grassland meadow and shrubland
3	Sodankylä	26.65	67.37	212.5	0.983	3	Sandy loam	8	Evergreen forest, Needle-leaved forest
4	Norunda	17.48	60.08	21.7	0.823	2	Loamy sand	8	Evergreen forest, Needle-leaved forest
5	Oueme	2	9.5	359.8	1.924	2	Loamy sand	7	Tropical evergreen broad-leaved forest
6	Niamey	2.5	13.5	223	0.34	2	Loamy sand	3	Short grassland meadow and shrubland
7	ARM Southern Great Plains	-97.49	36.61	331.1	0.5	8	Silty clay loam	3	Short grassland meadow and shrubland
8	Bondville	-88.29	40.01	223.3	0.5	4	Silt loam	1	Mixed farming tall grassland
9	Fort Peck	-105.1	48.31	718.1	0.5	6	Loam	3	Short grassland meadow and shrubland
10	Oak Ridge	-84.29	35.96	364.2	0.592	4	Silt loam	10	Deciduous forest
11	Mt. Bigelow	-110.73	32.42	1094.4	0.829	6	Loam	2	Tall/medium grassland, shrubland
12	BERMS (Old Black Spruce)	-105.12	53.99	538.8	0.548	3	Sandy loam	8	Evergreen forest, needle-leaved forest
13	Eastern Siberian Tundra	128.75	71.62	120.1	0.1	8	Silty clay loam	4	Tundra
14	Eastern Siberian Tiaga	129.62	62.25	198.7	1	8	Silty clay loam	10	Deciduous forest
15	Mongolia	106.26	45.74	1387.4	0.02	8	Silty clay loam	3	Short grassland meadow and shrubland
16	Tibet	91.9	31.37	4767.1	0.02	8	Silty clay loam	12	Ice
17	Tibet - Gaize	84.08	32.5	4748	0.02	8	Silty clay loam	12	Ice

18	Yangtze River	116	32	86.9	0.991	9	Clay loam	1	Mixed farming tall grassland
19	Inner Mongolia	122.12	44.46	152.4	0.53	12	Clay	1	Mixed farming tall grassland
20	Northern South China Sea - Southern Japan	121.18	24.97	341.1	0	0	Sea point	0	Sea point
21	Himalayas	86.81	27.96	4597.5	0.483	8	Silty clay loam	3	Short grassland meadow and shrubland
22	Korean Haenam	126.57	34.55	11.4	0.5	8	Silty clay loam	1	Mixed farming tall grassland
23	Korean Peninsula	127.9	37.44	406.6	0.5	8	Silty clay loam	9	Medium grassland, woodland
24	Chao-Phraya River	99.87	17.16	32.7	0.649	9	Clay loam	7	Tropical evergreen broad-leaved forest
25	Chao-Phraya River - Phitsanulok	100.48	16.85	176.7	0.759	3	Sandy loam	1	Mixed farming tall grassland
26	Chao-Phraya River - Lampang	99.47	18.4	395.1	0.006	9	Clay loam	7	Tropical evergreen broad-leaved forest
27	Chao-Phraya River - Kog-ma	98.9	18.81	693.1	0	9	Clay loam	7	Tropical evergreen broad-leaved forest
28	North-East Thailand	102.38	14.47	289.1	0.755	3	Sandy loam	1	Mixed farming tall grassland
29	Western Pacific Ocean	134.27	7.04	0	0.001	0	Sea point	0	Sea point
30	Western Pacific Ocean - Aimeliik	134.48	8.46	-1.1	0	0	Sea point	0	Sea point
31	Equatorial Island	100.32	-0.2	553.9	2.399	9	Clay loam	7	Tropical evergreen broad-leaved forest
32	Rondonia	-61.93	-10.08	226.4	2.7	12	Clay	7	Tropical evergreen broad-leaved forest
33	Manaus	-60.21	-2.61	64.5	2.7	12	Clay	7	Tropical evergreen broad-leaved forest
34	Santarem	-54.97	-3.02	93.4	2.7	12	Clay	9	Medium grassland, woodland
35	Caxiuana	-51.51	-1.71	-3.6	2.7	12	Clay	7	Tropical evergreen broad-leaved forest
36	Pantanal	-57.01	-19.56	111.7	0.8	12	Clay	3	Short grassland meadow and shrubland
37	Brasilia	-47.92	-15.93	1006.2	0.8	12	Clay	9	Medium grassland, woodland

38	Tumbarumba	148.15	-35.66	566	1.298	3	Sandy loam	1	Mixed farming tall grassland
39	ARM North Slope of Alaska (Barrow)	-156.62	71.32	2.2	0.01	0	Sea point	12	Ice
40	ARM Tropical Western Pacific (Manus)	147.43	-2.06	-4.2	0	0	Sea point	0	Sea point
41	ARM Tropical Western Pacific (Darwin)	130.89	-12.43	24.9	0.8	3	Sandy loam	3	Short grassland meadow and shrubland

Table A.3: CEOP contributions from various participating modeling centers, demonstrating the type, size, and temporal coverage throughout CEOP's first phase (updated version of the table that appears in Toussaint et al., 2007, reprinted with permission from Hans Luthardt).

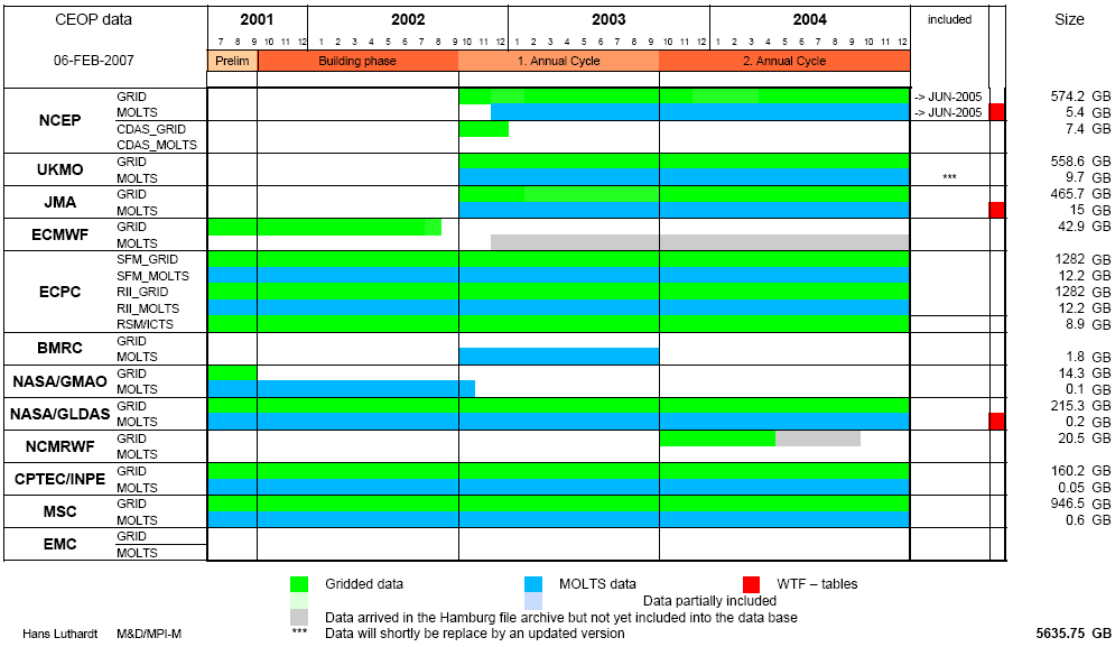

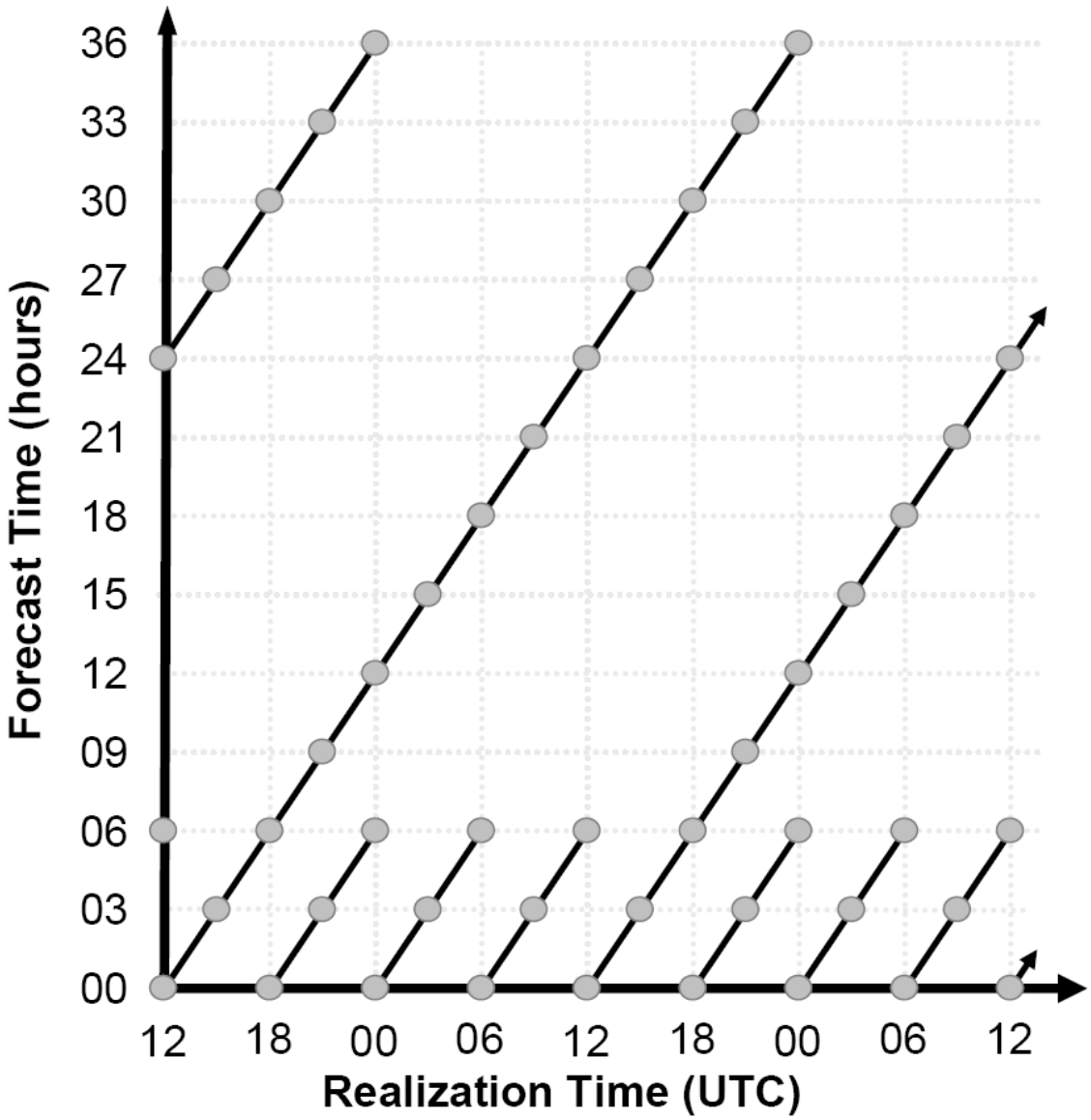

Figure A.1: Experimental design overview (as in Fig. 4.3), but displaying both the analysis and forecast experiments submitted to the CEOP model archive for both the R2 and the SFM.

References

Adler, R.F., G.J. Huffman, and P.R. Keehn, 1994: Global rain estimates from microwave adjusted geosynchronous IR data. *Remote Sens. Rev.* **11**, 125-152.

Anderson, B.T., and H. Kanamaru, 2005: The diurnal cycle of the summertime atmospheric hydrologic cycle over the southwestern United States. *J. Hydrometeor.* **6**, 219-228.

Anderson, B.T., A. Ruane, J.O. Roads, M. Kanamitsu, and G. Salvucci, 2007: A new metric for estimating local moisture cycling and its influence upon seasonal precipitation rates. *J. Hydrometeor.* in review.

Arkin, P.A., and P. Xie, 1994: The Global Precipitation Climatology Project: First algorithm intercomparison project. *Bull. Amer. Meteor. Soc.* **75(**3**)**, 401-419

Blackmon, M.L., Y.-H. Lee, and J.M. Wallace, 1984: Horizontal structure of 500mb height fluctuations with long, intermediate and short time scales. *J. Atmos. Sci.* **41(**6**)**, 961-979.

Bosilovich, M.G., and R. Lawford, 2002: Report on the Coordinated Enhanced Observing Period (CEOP) International Workshop. *Bull. Amer. Meteor. Soc.* **83**, 1495-1499.

Carbone, R.E., J.D. Tuttle, D.A. Ahijevych, and S.B. Trier, 2002: Inferences of predictability associated with warm season precipitation episodes. *J. Atmos. Sci.* **59(**13**)**, 2033-2056.

Campana, K.A., Y.-T. Hou, K.E. Mitchell, S.-K. Yang, and R. Cullather, 1994: Improved diagnostic cloud parameterization in NMC's global model. Preprints, *10th Conf. on Numerical Weather Prediction*, Portland, OR, Amer. Meteor. Soc., 324-325.

Chen, M., R.E. Dickinson, X. Zeng, and A.N. Hahmann, 1996: Comparison of precipitation observed over the Continental United States to that simulated by a climate model. *J. Climate* **9**, 2233-2249.

Chou, M.-D., 1992: A solar radiation model foruse in climate studies. *J. Atmos. Sci.* **49**, 762-772.

Chou, M.-D., and K.-T. Lee, 1996: Parameterizations for the absorption of solar radiation by water vapor and ozone. *J. Atmos. Sci.* **53**, 1203-1208

Chou, M.-D., and M.J. Suarez, 1994: An efficient thermal infrared radiation parameterization for use in general circulation models. NASA Tech. Rep. TM-1994-104606 Series on Global Modeling and Data Assimilation, 85 pp.

Dai, A., 2001: Global precipitation and thunderstorm frequencies. Part II: Diurnal variations. *J. Climate* **14**, 1112-1128.

Dai, A., 2006: Precipitation Characteristics in Eighteen Coupled Climate Models. *J. Climate* **19**, 4605-4630.

Dai, A., K.E. Trenberth, and T.R. Karl, 1999a: Effects of clouds, soil moisture, precipitation, and water vapor on diurnal temperature range. *J. Climate* **12**, 2451-2473.

Dai, A., F. Giorgi, and K.E. Trenberth, 1999b: Observed and model-simulated diurnal cycles of precipitation over the contiguous United States. *J. Geophys. Res.* **104**, 6377-6402.

Dai, A., J. Wang, R.H. Ware, and T. Van Hove, 2002: Diurnal variation in water vapor over North America and its implications for sampling errors in radiosonde humidity. *J. Geophys. Res.* **104,** D10, doi:10.1029/2001JD000642.

Dai, A., X. Lin, and K.-L. Hsu, 2007: The frequency, intensity, and diurnal cycle of precipitation in surface and satellite observations over low- and mid-latitudes. *Clim. Dyn.* in press.

Dai, A., and C. Deser, 1999: Diurnal and semidiurnal variations in global surface wind and divergence fields. *J. Geophys. Res.* **104**, 31109-31125.

Dai, A., and K.E. Trenberth, 2004: The diurnal cycle and its depiction in the Community Climate System model. *J. Climate* **17**, 930-951

Dai, A., and J. Wang, 1999: Diurnal and semidiurnal tides in global surface pressure fields. *J. Atmos. Sci.* **56(***22***)**, 3874-3891.

Dunkerton, T.J., and F.X. Crum, 1995: Eastward propagating ~2- to 15-day equatorial convection and its relation to the tropical intraseasonal oscillation. *J. Geophys. Res.* **100(**D12**)**, 25,781-25,790.

Ebert, E.E., J.E. Janowiak, and C. Kidd, 2007: Comparison of near-real-time precipitation estimates from satellite observations and numerical models. *Bull. Amer. Meteor. Soc.* **88(**1**)**, 47-64.

Ek, M.B., K.E. Mitchell, Y. Lin, E. Rogers, P. Grunmann, V. Koren, G. Gayno, and J.D. Tarpley, 2003: Implementation of Noah land surface model advances in the National Centers for Environmental Prediction operational mesoscale Eta model. *J. Geophys. Res.* **208(***D22***)**, 8851, doi:10.1029/2002JD003296

Fels, S.B., and M.D. Schwarzkopf, 1975: The simplified exchange approximation: A new method for radiative transfer calculations. *J. Atmos. Sci.* **32**, 1475-1488.

Emery, W.J., and R.E. Thomson, 2004: Data Analysis Methods in Physical Oceanography. Elsevier, Amsterdam, pp. 638.

Gray, W.M., and R.W. Jacobson, 1977: Diurnal variation of deep cumulus convection. *Mon. Wea. Rev.* **105**, 1171-1188.

Gutzler, D.S., H.-K. Kim, R.W. Higgins, H.-M.H. Juang, M. Kanamitsu, K. Mitchell, K. Mo, P. Pegion, E. Ritchie, J.-K. Schemm, S. Schubert, Y. Song, and R. Yang, 2005: The North American Monsoon Model Assessment Project. *Bull. Amer. Meteor. Soc.* **86*(10)***, 1423-1429.

Haertel, P.T., and G.N. Kiladis, 2004: Dynamics of 2-day equatorial waves. *J. Atmos. Sci.* **61**, 2707-2721

Hendon, H.H., and K. Woodberry, 1993: The diurnal cycle of tropical convection. *J. Geophys. Res.* **98(**D9**)**, 16623-16637.

Higgins, R.W., Y. Yao, E.S. Yarosh, J.E. Janowiak, and K.C. Mo, 1997a: Influence of the Great Plains low-level jet on summertime precipitation and moisture transport over the Central United States. *J. Climate* **10**, 481-507.

Higgins, R.W., Y. Yao, and X.L. Wang, 1997b: Influence of the North American monsoon system on U.S. summer precipitation regime. *J. Climate* **10**, 2600-2622.

Hong, S.-Y., and H.-L. Pan, 1996: Nonlocal boundary layer vertical diffusion in a medium-range forecast model. *Mon. Wea. Rev.* **124**, 2322-2339.

Hsu, K., X. Gao, S. Sorooshian, and H.V. Gupta, 1997: Precipitation estimation from remotely sensed information using artificial neural networks. *J. Appl. Meteor.* **36**, 1176-1190.

Janjić, Z.I., 1994: 'The Step-Mountain Eta Coordinate Model – further developments of the convection, viscous sublayer, and turbulence closure schemes. *Mon. Wea. Rev.* **122(**5**)**, 927-945

Janjić, Z.I., 1996: The Mellor-Yamada level-2.5 scheme in the NCEP Eta model. Preprint, 11th AMS Conference on Numerical Weather Prediction, Norfolk, VA, 333-334.

Janowiak, J.E., V.E. Kousky, and R.J. Joyce, 2005: Diurnal cycle of precipitation determined from the CMORPH high spatial and temporal resolution global precipitation analyses. *J. Geophys. Res.* **110**, D23105, doi:10.1029/2005JD006156.

Jones, C., and L.M. Carvalho, 2002: Active and break phases in the South American monsoon system. *J. Climate* **15**, 905-914.

Joyce, R.J., J.E. Janowiak, P.A. Arkin, and P. Xie, 2004: CMORPH: A method that produces global precipitation estimates from passive microwave and infrared data at high spatial and temporal resolution. *J. Hydromet.* **5**, 487-503.

Kanamitsu, M., W. Ebisuzaki, J. Woollen, S.-K. Yang, J. Hnilo, M. Fiorino, and J. Potter, 2002a: NCEP/DOE AMIP-II Reanalysis (R-2). *Bull. Amer. Meteor. Soc.* **83(***11***)**, 1631-1643

Kanamitsu, M, A. Kumar, H.-M.H. Juang, J.-K. Schemm, W. Wang, F. Yang, S.-Y. Hong, P. Peng, W. Chen, S. Moorthi, and M. Ji, 2002b: NCEP dynamical seasonal forecast system 2000. *Bull. Amer. Meteor. Soc.* **83(***7***)**, 1019-1037.

Knutson, T.R., and K.M. Weickmann, 1987: 30-60 day atmospheric oscillations: Composite life cycles of convection and circulation anomalies. *Mon. Wea. Rev.* **115**, 1407-1436.

Koike, T., 2004: The Coordinated Enhanced Observing Period – an initial step for integrated global water cycle observation. *WMO Bulletin* **53(**2**)**, 1-8.

Kraus, E.B., 1963: The diurnal precipitation change over the sea. *J. Atmos. Sci.* **20(***6***)**, 551-556.

Kummerow, C., J. Simpson, O. Thiele, W. Barnes, A.T.C. Chang, E. Stocker, R.F. Adler, A. Hou, R. Kakar, F. Wentz, P. Ashcroft, T. Kozu, Y. Hong, K. Okamoto, T. Iguchi, H. Kuroiwa, E. Im, Z. Haddad, G. Huffman, B. Ferrier, W.S. Olson, E. Zipser, E.A. Smith, T.T. Wilheit, G. North, T. Krishnamurti, and K. Nakamura, 2000: The status of the Tropical Rainfall Measuring Mission (TRMM) after two years in orbit. *J. Appl. Meteor.* **39**, 1965-1982.

Lacis, A.A., and J.E. Hansen, 1974: A parameterization for the absorption of solar radiation in the earth's atmosphere. *J. Atmos. Sci.* **31**, 118-133.

Lau, K.-M, L. Peng, C.-H. Sui, and T., Nakazawa, 1989: Dynamics of super cloud clusters, westerly wind bursts, 30-60 day oscillations and ENSO – an unified view. *J. Meteor. Soc. Jpn.* **67(**2**)**, 205-219.

Lawford, R., M. Bosilovich, S. Eden, S. Benedict, C. Brown, A. Gruber, P. Houser, K. Hsu, J. Huang, W. Lau, T. Meyers, K. Mitchell, C. Peters-Lidard, J. Roads, M., Rodell, S. Sorooshian, D. Tarpley, and S. Williams, 2006: U.S. contributions to the CEOP. *Bull. Amer. Meteor. Soc.* **87(**7**)**, 927-939.

Lee, M.-I., S. D. Schubert, M. J. Suarez, I. M. Held, N.-C. Lau, J. J. Ploshay, A. Kumar, H.-K. Kim, and J. E. Schemm, 2006: An analysis of the warm season diurnal cycle over the continental United States and northern Mexico in general circulation models. *J. Hydromet.,* revised.

Lee, M.-I., S.D. Schubert, M.J. Suarez, I.M. Held, A. Kumar, T.L. Bell, J.-K.E. Shemm, N.-C. Lau, J.J. Ploshay, H.-K. Kim, and S.-H. Yoo, 2006: Sensitivity to horizontal resolution in the AGCM simulations of the warm season diurnal cycle of precipitation over the United States and Northern Mexico. *J. Climate*, submitted.

Lin, J.-L., G.N. Kiladis, B.E. Mapes, K.M. Weickmann, K.R. Sperber, W. Lin, M.C. Wheeler, S.D. Schubert, A.D. Genio, L.J. Donner, S. Emori, J.-F. Gueremy, F. Hourdin, P.J. Rasch, E. Roeckner, and J.F. Scinocca, 2006: Tropical intraseasonal variability in 14 IPCC AR4 climate models. Part I: Convective signals. *J. Climate* **19**, 2665-2690.

Lin, X., D.A. Randall, and L.D. Fowler, 2000: Diurnal variability of the hydrologic cycle and radiative fluxes: Comparisons between observations and a GCM. *J. Climate* **13(***23***)**, 4159-4179.

Lindzen, R.S., 1967: Thermally driven diurnal tide in the atmosphere. *Quart. J. Roy. Meteor. Soc.* **93**, 18-42.

Lim, G.-H., and A.-S. Suh, 2000: Diurnal and semidiurnal variations in the time series of 3-hurly assimilated precipitation by NASA GEOS-1. *J. Climate* **13(***8***)**, 2923-2940.

Lu, C.-H., M. Kanamitsu, J.O. Roads, W. Ebisuzaki, K.E. Mitchell, and D. Lohmann, 2005: Evaluation of soil moisture in the NCEP-NCAR and NCEP-DOE Global Reanalyses. *J. Hydrometeor.* **6**, 391-408.

Madden, R.A., and P.R. Julian, 1971: Detecton of a 40-50 day oscillation in the zonal wind in the tropical Pacific. *J. Atmos. Sci.* **28**, 702-708.

Madden, R.A., and P.R. Julian, 1972: Description of global-scale circulation cells in the Tropics with a 40-50 day period. *J. Atmos. Sci.* **29**, 1109-1123.

Madden, R.A., and P.R. Julian, 1994: Observations of the 40-50-day tropical oscillation – A review. *Mon. Wea. Rev.* **122**, 814-837.

Matthews, A.J., and G.N. Kiladis, 1999: The tropical-extratropical interaction between high-frequency transients and the Madden-Julian Oscillation. *Mon. Wea. Rev.* **127**, 661-677.

Mellor, G.L., and T. Yamada, 1982: Development of a turbulence closure model for geophysical fluid problems. *Rev. Geophys. Space Phys.* **20**, 851-875.

Mesinger, F., 1993: Forecasting upper tropospheric turbulence within the framework of theMellor-Yamada 2.5 closure. *Res. Activ. Atmos. Oceanic Mod.,* CAS/JSC WGNE Rep. 18, 4.28-4.29, WMO, Geneva.

Mesinger, F., G. DiMego, E. Kalnay, K. Mitchell, P.C Shafran, W. Ebisuzaki, D. Jovic, J. Woollen, E. Rogers, E.H. Berbery, M.B. Ek, Y. Fan, R. Grumbine, W. Higgins, H. Li, Y. Lin, G. Manikin, D. Parrish, and W. Shi, 2006: North American Regional Reanalysis. *Bull. Amer. Met. Soc.* **87(**3**)**, 343-360.

Mitchell, K., M. Ek, Y. Lin, F. Mesinger, G. DiMego, P., Shafran, D. Jovic, W. Ebisuzaki, W.Shi, Y. Fan, J. Janowiak, and J. Shaake, 2004: NCEP completes 25-year North American reanalysis: Precipitation assimilation and land surface are two hallmarks. *GEWEX Newsletter* **14(***2***)**, 9-12.

Mo, K.C., M. Chelliah, M.L. Carrera, R.W. Higgins, and W. Ebisuzaki: Atmospheric moisture transport over the United States and Mexico as evaluated in the NCEP Regional Reanalysis. *J. Hydromet.* **6**, 710-728

Moorthi, S., and M.J. Suarez, 1992: Relaxed Arakawa-Schubert: A parameterization of moist convection for general circulation models. *Mon. Wea. Rev.* **120**, 978-1002.

Nakamura, K., 2004: Diurnal variation of precipitation measured by the TRMM TMI. *GEWEX Newsletter* **14***(2)*, 4.

Newell, R.E., N.E. Newell, Y. Zhu, and C. Scott, 1992: Tropospheric rivers? – A pilot study. *Geophys. Res. Lett.* **12(**24**)**, 2401-2404.

Newman, M., P.D. Sardeshmukh, and J.W. Bergman, 2000: An assessment of the NCEP, NASA, and ECMWF reanalyses over the Tropical West Pacific Warm Pool. *Bull. Amer. Meteor. Soc.* **81(1)**, 41-48.

Pan, H.-L., and L. Mahrt, 1987: Interaction between soil hydrology and boundary layer developments, *Bound.-Layer Meteor.* **38**, 185-202.

Pan, H.-L., and W.-S. Wu, 1995: Implementing a mass flux convection parameterization package for the NMC Medium-Range Forecast Model. NMC Office Note 409, 40 pp. [Available from NCEP/EMC 5200 Auth Road, Camp Springs, MD 20746].

Randall D.A, Hashvardhan, and D.A. Dazlich, 1991: Diurnal variability of the hydrologic cycle in a general circulation model. *J. Atmos. Sci.* **48**, 40-62.

Rasmusson, E.M, 1967: Atmospheric water vapor transport and the water balance of North America: Part I. Characteristics of the water vapor flux field. *Mon. Wea. Rev.* **95(**7**)**, 403-426.

Rasmusson, E.M., and P.A. Arkin, 1993: A global view of large-scale precipitation variability. *J. Climate* **6**, 1495-1522.

Reichler, T., and J.O. Roads, 2005: Long-range predictability in the Tropics. Part II: 30-60-day variability. *J. Climate* **18**, 634-650.

Roads, J., and A. Betts, 2000: NCEP-NCAR and ECMWF Reanalysis surface water and energy budgets for the Mississippi River Basin. *J. Hydrometeor.* **1**, 88-94.

Roads, J., M. Kanamitsu, and R. Stewart, 2002: CSE water and energy budgets in the NCEP-DOE Reanalysis II. *J. Hydrometeor.* **3**, 227-248.

Ruane, A.C., and J.O. Roads, 2007a: The diurnal cycle of water and energy over the continental United States from three reanalyses. *J. Meteor. Soc. Jpn*. **85A**, 117-143.

Ruane, A.C., and J.O. Roads, 2007b: 6-hour to 1-year variance of five global precipitation sets. *Earth Interactions*, in press.

Ruane, A.C., and J.O. Roads, 2007c: Dominant balances and exchanges of the atmospheric water cycle at diurnal, annual, and intraseasonal time scales. *J. Climate* in review.

Ruane, A.C., and J.O. Roads, 2007d: Water cycle sensitivity to convective and land-surface schemes in global free forecasts. in preparation.

Schubert, S.D., H.M. Helfand, C.-Y. Wu, and W. Min, 1998: Subseasonal variations in warm-season moisture transport and precipitation over the Central and Eastern United States. *J. Climate* **11**, 2530-2555.

Simpson, J., R.F. Adler, and G.R. North, 1988: A proposed Tropical Rainfall Measuring Mission (TRMM) satellite. *Bull. Amer. Meteor. Soc.* **69(**3**)**, 278-295.

Slingo, J.M., 1987: The development and verification of a cloud prediction model for the ECMWF model. *Quart. J. Roy. Meteor. Soc.* **113**, 899-927.

Slingo, J.M., K.R. Sperber, J.S. Boyle, J.P. Ceron, M. Dix, B. Dugas, W. Ebisuzaki, J. Fyfe, D. Gregory, J.F. Gueremy, J. Hack, A. Harzallah, P. Inness, A. Kitoh, W.K.M. Lau, B. McAvaney, R. Madden, A. Matthews, T.N. Palmer, C.K. Park, D. Randall, and N. Renno, 1996: Intraseasonal oscillations in 15 atmospheric general circulation models: Results from an AMIP diagnostic subproject. *Climate Dyn.* **12(**5**)**, 325-357.

Sorooshian, S., K.-L. Hsu, X. Gao, H.V. Gupta, B. Imam, and D. Braithwaite, 2000: Evaluation of PERSIANN system satellite-based estimates of tropical rainfall. *Bull. Amer. Met. Soc.* **81(**9**)**, 2035-2046.

Sorooshian, S., X. Gao, K. Hsu, R.A. Maddox, Y. Hong, H.V. Gupta, and B. Imam, 2002: Diurnal variability of tropical rainfall retrieved from combined GOES and TRMM satellite information. *J. Climate* **15**, 983-1001.

Sui, C.-H., and K.-M. Lau, 1992: Multiscale phenomena in the tropical atmosphere over the Western Pacific. *Mon. Wea. Rev.* **120**, 407-430.

Torrence, C., and G.P. Compo, 1998: A practical guide to wavelet analysis. Bull. Amer. Meteor. Soc. **79(**1**)**, 61-78.

Toussaint, F., M. Lautenschlager, and H. Luthardt, 2007: World Data Center for Climate data – support for the CEOP project in terms of model output. *J. Meteor. Soc. Jpn.* **85A**, 475-485.

Trenberth, K.E., and C.J. Guillemot, 1995: Evaluation of the global atmospheric moisture budget as seen from analyses. *J. Climate* **8**, 2255-2272.

Trenberth, K.E., and C.J. Guillemot, 1998: Evaluation of the atmospheric moisture and hydrologic cycle in the NCEP NCAR reanalyses. *Clim. Dyn.* **14**, 213-231.

Trenberth, K.E., A. Dai, R.M. Rasmussen, and D.B. Parsons, 2003: The changing character of precipitation. *Bull. Amer. Meteor. Soc.* **84(***9***)**, 1205-1217.

Vincent, D.G., A. Fink, J.M. Schrage, and P. Speth, 1998: High- and low-frequency intraseasonal variance of OLR on annual and ENSO timescales. *J. Climate* **11**, 968-986.

Wallace, J.M., 1975: Diurnal variations in precipitation and thunderstorm frequency over the conterminous United States. *Mon. Wea. Rev.* **103**, 406-419.

Wilson C.A., and J.F.B. Mitchell, 1986: Diurnal variation and cloud in a general circulation model. *Quart. J. Roy. Meteor. Soc.* **112**, 347-369.

Yang, S., and E.A. Smith, 2006: Mechanisms for diurnal variability of global tropical rainfall observed from TRMM. *J. Climate*, in press.

Zhang, C., 2005: Madden-Julian Oscillation. *Rev. Geophys.* **43**, RG2003, doi:10.1029/2004RG000158.

Zhang, G.J., 2006: Roles of atmospheric and boundary layer forcing in the diurnal cycle of convection in the U.S. southern great plains. *Geophys. Res. Lett.* **30(***24***)**, 2281.

Zhao, Q., T.L. Black, and M.E. Baldwin, 1997: Implementation of the cloud prediction scheme in the Eta model at NCEP. *Wea. Forecasting* **12**, 697-712.

Zhao, Y., and B.C. Weare, 1994: The effect of diurnal variation of cumulus convection on large-scale low-frequency oscillation in the Tropics. *J. Atmos. Sci.* **51(**18**)**, 2653-2663.